CHARACTERIZATION OF LATTICE MISMATCH INDUCED DISLOCATIONS ON EPITAXIAL CDTE FILMS

A Thesis Submitted to
Graduate School of Engineering and Sciences of
İzmir Institute of Technology
in Partial Fulfillment of the Requirements for the Degree of

MASTER OF SCIENCE

in Physics

by
Elif BİLGİLİSOY

July 2015
İZMİR

We approve the thesis of **Elif BİLGİLİSOY**

Examining Committee Members:

____

Assoc. Prof. Dr. Yusuf SELAMET
Department of Physics, İzmir Institute of Technology

____

Assoc. Prof. Dr. Emre GÜR
Department of Physics, Atatürk University

____

Prof. Dr. Orhan ÖZTÜRK
Department of Physics, İzmir Institute of Technology

24 July 2015

____

Assoc. Prof. Dr. Yusuf SELAMET
Supervisor, Department of Physics
İzmir Institute of Technology

____

Prof. Dr. Nejat BULUT
Head of the Department of Physics

____

Prof. Dr. Bilge KARAÇALI
Dean of the Graduate School of
Engineering and Sciences

ACKNOWLEDGEMENTS

Firstly, I would like to thank my parents for all of their patience and support through the whole process of my study.

I would like to thank my advisor Assoc. Prof. Dr. Yusuf Selamet for all his help, patience and detailed reviewing all of my study. Without his support and guidance, I would never have been able to complete this study.

I wish to thank the other committee members of my thesis Assoc. Prof. Dr. Emre Gür and Prof. Dr. Orhan Öztürk for their participation and comments.

I would like to acknowledge and thank all of my colleagues and friends who helped me through the whole process of my study. Especially, I would like to thank Selin Özden and Sinem Duman for their friendship and Raman spectroscopy mapping measurements and also Emine Bakali for SEM measurements. I would also like to thank Merve Karakaya and Begüm Yavaş for their great friendship and *ex-situ* SE measurements. I would like to thank to Mustafa Polat for XRD measurements and Ozan Arı for MBE growth. In addition, I would like to thank Nesli Tekgüzel Yağmurcukardeş and Hasan Aydın for teaching me AFM. I would like to thank Elif Özçeri, Alper Yanılmaz and Erdi Kuşdemir for their friendship and support.

I would like to thank to Oğuzhan Alperen who always supported and encouraged me through this whole process.

I wish to acknowledge using of facilities at the IZTECH Material Research Center for SEM. In addition, I would like to thank ASELSAN and SSM for financial and technical support.

ABSTRACT

CHARACTERIZATION OF LATTICE MISMATCH
INDUCED DISLOCATIONS ON
EPITAXIAL CDTE FILMS

Mercury Cadmium Telluride (HgCdTe) is a widely used material for infrared focal plane array applications. In order to produce high quality infrared detecting material, HgCdTe needs to be grown on large area alternative substrates such as GaAs, GaSb, Si or Ge. GaAs is the best choice as an alternative substrate due to its surface polarity and commercially availability of high quality epi-ready wafers. However, there exists a lattice mismatch between HgCdTe and GaAs. To minimize the detrimental effect of the large lattice mismatch between the two materials, Cadmium Telluride (CdTe) is preferred as a buffer layer for HgCdTe IR material. The lattice mismatch between HgCdTe/CdTe and the GaAs substrate results in a large number of misfit dislocations. Dislocation density of the buffer layer limits and reduces the detector device performance. For this reason, the crystal quality and dislocation analysis of CdTe are examined in detail to produce large area and high performance HgCdTe IR devices.

The aim of this thesis is the characterization of lattice mismatch induced dislocations on epitaxial CdTe buffer layers. CdTe epilayers which were grown on (211)B GaAs by molecular beam epitaxy (MBE) were subjected to two different etch treatments to quantify the crystal quality and dislocation density. The crystal quality was also obtained by using x-ray diffraction (XRD) measurements. The thicknesses of the samples were measured by *ex-situ* spectroscopic ellipsometry (SE). The surface morphologies of the CdTe buffer layers were analyzed by atomic force microscopy (AFM), scanning electron microscopy (SEM) and Nomarski microscopy before and after wet chemical etching. Vibrational phonon modes distributions of the as-grown and etched samples were examined by Raman spectroscopy mapping. The “triangle” and “trapezoid” shaped etch pits were compared due to the Everson and Nakagawa etching solutions, respectively. Measured etch pit density (EPD) values of “triangle” etch pits were found in $0.3 \times 10^8 – 3.8 \times 10^8$ cm^{-2} range and “trapezoid” shaped etch pits were found in $0.03 \times 10^8 – 0.6 \times 10^8$ cm^{-2} range for samples.

ÖZET

EPİTAKSİYEL CDTE FİLMLERİN ÖRGÜ UYUMSUZLUĞUNDAN KAYNAKLANAN DİSLOKASYONLARIN KARAKTERİZASYONU

Cıva Kadmiyum Tellür (HgCdTe), kızılötesi fokal düzlem dizini uygulamaları için en yaygın kullanılan malzemedir. Yüksek kalitede kızılötesi algılayıcı malzeme üretebilmek için HgCdTe geniş alanlı GaAs, GaSb, Si veya Ge gibi alt-tabanlar üzerine büyütülmelidir. Yüzey polaritesinden ve yüksek kalitede hazır alt-tabanların ticari olarak bulunmasından dolayı GaAs alt-taban olarak en iyi tercihtir. Ancak; HgCdTe ve GaAs arasında örgü uyumsuzluğu mevcuttur. Bu iki malzeme arasındaki büyük örgü uyumsuzluğunun hasar verici etkilerini en aza indirmek için Kadmiyum Tellür (CdTe) HgCdTe malzemesinde tampon katman olarak tercih edilmektedir. HgCdTe/CdTe ve GaAs arasındaki örgü uyumsuzluğu çok sayıda dislokasyona yol açar. Tampon katmandaki dislokasyon yoğunluğu detektör performansını kısıtlar ve azaltır. Bu nedenle, geniş alanlı ve yüksek performanslı HgCdTe kızılötesi cihazlar üretmek için CdTe malzemesinin kristal kalitesi ve dislokasyon analizi detaylı olarak incelenmelidir.

Bu tezin amacı, epitaksiyel CdTe tampon katmanların üzerinde örgü uyumsuzluğunun sebep olduğu dislokasyonların karakterizasyonudur. Moleküler demet epitaksi (MBE) ile (211)B GaAs üzerine büyütülen CdTe katmanların kristal kalitesi ve dislokasyon yoğunluğunun belirlenmesi için iki farklı aşındırma tekniği uygulanmıştır. Kristal kalitesi ayrıca X-ışını kırınımı (XRD) ölçümleri kullanılarak da elde edilmiştir. Örneklerin kalınlıkları spektroskopik elipsometre (SE) ile ölçülmüştür. CdTe tampon katmanların yüzey yapıları atomik kuvvet mikroskobu (AFM), taramalı elektron mikroskobu (SEM) ve Nomarski mikroskobu ile ıslak kimyasal aşındırma öncesi ve sonrasında analiz edilmiştir. Büyütülen ve aşındırılan örneklerin titreşimli fonon mod dağılımları Raman spektroskopi haritalama ile incelenmiştir. Everson ve Nakagawa aşındırma karışımları sonucunda sırasıyla oluşan "üçgen" ve "yamuk" şekilli aşındırma kusurları karşılaştırılmıştır. Ölçülen aşındırma çukur yoğunluğu (EPD) değerleri, "üçgen" aşındırma çukurlarında $0.3x10^8$ – $3.8x10^8$ cm^{-2} aralığında ve "yamuk" aşındırma çukurlarında $0.03x10^8$ – $0.6x10^8$ cm^{-2} aralığında bulunmuştur.

TABLE OF CONTENTS

LIST OF FIGURES viii

LIST OF TABLES xiv

LIST OF ABBREVIATIONS xv

CHAPTER 1. INTRODUCTION 1

CHAPTER 2. CADMIUM TELLURIDE CRYSTAL AND DISLOCATION PROPERTIES 3

2.1. Crystal Structure 3

2.1.1. Crystal Lattice 3

2.1.1.1. Simple Cubic Lattice 3

2.1.1.2. Body Centered Cubic Lattice 4

2.1.1.3. Face Centered Cubic Lattice 5

2.1.1.4. Zinc-Blende Lattice 6

2.2. Alternative Substrates of Cadmium Telluride 7

2.3. Molecular Beam Epitaxial Growth of Cadmium Telluride 9

2.4. Uses of Cadmium Telluride 10

2.5. Polar Surfaces of Cadmium Telluride 11

CHAPTER 3. DEFECTS IN CRYSTALS 13

3.1. Zero Dimensional Defects 13

3.2. One Dimensional Defects 15

3.2.1. Edge Dislocation 16

3.2.2. Screw Dislocation 17

3.2.3. Mixed Dislocation 18

3.2.4. Burgers Circuit 19

3.2.5. Calculation of Dislocation Stress Strain and Energy 20

3.2.6. Motion of Dislocation 26

3.3. Two Dimensional Defects 29

3.4. Three Dimensional Defects 33

3.5. Lattice Mismatch 33

3.5.1. Misfit Dislocation 34
3.5.2. Dislocation Interaction 36

CHAPTER 4. OBSERVATION OF DISLOCATIONS 39
4.1. Defect Decoration Methods 39
4.1.1. Everson Etch 40
4.1.2. Nakagawa Etch 41
4.1.3. Benson Etch 43
4.1.4. Schaake Etch 43
4.2. Transmission Election Microscopy 44
4.3. Electrical Characterization of Etch Pit Density 46

CHAPTER 5. EXPERIMENTAL TECHNIQUES AND PROCEDURES 48
5.1. Atomic Force Microscopy 48
5.2. Scanning Electron Microscopy 51
5.3. Nomarski Microscopy 53
5.4. Reflected High Energy Electron Diffraction 54
5.5. Raman Mapping 57

CHAPTER 6. EXPERIMENTAL RESULTS AND DISCUSSION 59
6.1. MBE Grown CdTe/GaAs (211)B Epilayers 59
6.2. RHEED Characterization Results 62
6.3. Structural Analysis of As-Grown CdTe (211)B Buffer Layers 67
6.3.1. Nomarski Characterization Results 67
6.3.2. AFM Characterization Results 68
6.3.3. SEM Characterization Results 75
6.4. Defect Decoration Etching Processes of CdTe (211)B Epilayers 77
6.5. Structural Analysis Results of Wet Chemically Etched CdTe 80
6.5.1. Nomarski Characterization Results 80
6.5.2. AFM Characterization Results 84
6.5.3. SEM Characterization Results 92
6.5.5. Raman Mapping Characterization Results 100

CHAPTER 7. CONCLUSION 107

REFERENCES 109

LIST OF FIGURES

Figure **Page**

Figure 1. A schematic representation of SC lattice. 4
Figure 2. A schematic representation of BCC. 5
Figure 3. A schematic representation of FCC. 5
Figure 4. A schematic representation of FCC for (a) Cd atoms, (b) Te atoms and (c) zinc-blende lattice structure of CdTe. 6
Figure 5. Range of the transmission of the IR spectra ground atmospheric windows ... 10
Figure 6. B-terminated (211) surface of CdTe 12
Figure 7. P-T curve and isohole concentration lines for CdTe for temperature range from 500 to 1100 K. 14
Figure 8. Schematic of different types of point defects in a crystal. (1) vacancy, (2) self-interstitial, (3) interstitial impurity, (4) and (5) substitutional impurities and (6) impurity defect (adapted from [34]). 15
Figure 9. Diagram of an edge dislocation 17
Figure 10. Diagram of a screw dislocation 18
Figure 11. Schematic of edge, screw and mixed dislocation types 19
Figure 12. Burgers circuit and Burgers vector representation (adapted from [43]). 20
Figure 13. Components of stress on the faces of an elemental cube. 21
Figure 14. Pure shear of an area element in the x-y plane. 22
Figure 15. (a) Screw dislocation formation in a crystal structure and (b) representation by using cylindrical shell 23
Figure 16. (a) Edge dislocation formation in a crystal structure and (b) representation by using cylindrical shell 24
Figure 17. CdTe slip system configuration. (a) {111} slip plane with <0-11><10-1><-110> slip directions, (b) {-1-11} slip plane with <011><-101><1-10> slip directions, (c) {-111} slip plane with <0-11><-10-1><110> slip directions and (d) {1-11} slip plane with <011><10-1><-1-10> slip directions. 27
Figure 18. An example of a conservative dislocation motion is motion of an edge dislocation (arrows show the applied shear stress) 28
Figure 19. Schematic of (a) positive and (b) negative types of climb. 29
Figure 20.Schematic of a low and high angle grain boundary and the angle of misalignment 31

Figure 21. Schematic of a twin boundary and a mirror image 32
Figure 22. Stacking faults in the FCC crystal structure. (a) Extrinsic stacking fault with an extra B plane and (b) intrinsic stacking fault with a missing A plane. 32
Figure 23. Schematic of (a) matched, (b) strained and (c) relaxed film on the substrate. 34
Figure 24. The schematic of misfit dislocation formation mechanisms in epitaxial films [61]. 35
Figure 25. The schematic representation of (a) repulsive, (b) attractive forces. 36
Figure 26. Graphically description of (a) neutralization and (b) combination of dislocations (adapted from [41]). 38
Figure 27. Nomarski microscopy images of (a) and (b) Everson etch pits on (111)B surface, (c) and (d) Everson etch pits on (211)B surface. TEM image of (e) Everson etch pits formed on dislocations [69]. 41
Figure 28. The CdTe (111) surfaces after 3HF: $2H_2O_2$: $1H_2O$ etch. Triangular etch pits are formed on Te-rich surface. Cadmium-rich surface is nearly polished 41
Figure 29. Optical microscopy images of (a) etch pits and how their positions into the sample and (b) surface after etching [73]. 42
Figure 30. Optical microscopy image of etch pits on CdTe (111)B surface [76].......... 42
Figure 31. (a) Nomarski microscopy, (b) low-resolution AFM and (c) high-resolution AFM images of a sample surface after Benson etching [77]. 43
Figure 32. (a) and (b) Nomarski microscopy images of after 15 s Schaake etch HgCdTe samples [79]. 44
Figure 33. Schematic description of TEM components. 45
Figure 34. R_0A versus EPD values for a device built on an (a) Array 1 and (b) Array 2 (Array 1 junction area: $6.8x10^{-6}$ cm^2 and Array 2: 1.1 $x10^{-5}$ cm^2) 47
Figure 35. Schematic description of tip bending (adapted from [85])........................... 48
Figure 36. Schematic representation of AFM components. 49
Figure 37. Lennard-Jones potential [86]. 50
Figure 38. Force as a function of probe-sample separation [89]. 50
Figure 39. Demonstration of output of interaction of electrons with sample. 51
Figure 40. Schematic diagram of a scanning electron microscope. 52
Figure 41. Schematic representative of DIC microscope working principle. 53
Figure 42. Representation of elastic scattering process [98]. 55
Figure 43. Schematically demonstration of experimental arrangements of RHEED. 56

Figure 44. Schematic representation of a confocal Raman spectroscopy...................... 58
Figure 45. [01-1] RHEED patterns of CT22 (a) after oxide desorption at 582 °C and (b) after growth at 300 °C. 62
Figure 46. [01-1] RHEED patterns of CT24 (a) after oxide desorption at 580 °C and (b) after growth at 320 °C. 63
Figure 47. [01-1] RHEED patterns of CT25 (a) after oxide desorption at 583 °C and (b) after growth at 295 °C. 64
Figure 48. [01-1] RHEED patterns of CT26 (a) after oxide desorption at 582 °C and (b) after growth at 295 °C. 64
Figure 49. [01-1] RHEED patterns of CT27 (a) after oxide desorption at 584 °C and (b) after growth at 302 °C. 65
Figure 50. Nomarski microscopy as-grown images of (a) CT6, (b) CT9 and (c) CT10 at 100x magnification... 67
Figure 51. Nomarski microscopy as-grown images of (a) CT22, (b) CT24, (c) CT25, (d) CT26 and (e) CT27 at 100x magnification. 68
Figure 52. (a) AFM 2D and (b) 3D topographical images of CT9 as-grown sample and (c) cross-section line analysis of XS1(line 144)... 69
Figure 53. (a) AFM 2D and (b) 3D topographical images of CT22 as-grown sample and cross-section line analysis of XS1(line 180). 70
Figure 54. (a) AFM 2D and (b) 3D topographical images of CT26 as-grown sample and cross-section line analysis of XS1(line 191). 71
Figure 55. (a) AFM 2D topographical image and (b) and cross-section line analysis of XS1(line 165) of CT10 as-grown sample. 73
Figure 56. (a) AFM 2D topographical image and (b) and cross-section line analysis of XS1(line 184) after CT10 polished with 0.5% Br_2-MeOH for 2 seconds....... 73
Figure 57. (a) AFM 2D topographical image and (b) and cross-section line analysis of XS1(line 138) after CT10 polished with 0.5% Br_2-MeOH for 10 seconds..... 74
Figure 58. (a) AFM 2D topographical image and (b) and cross-section line analysis of XS1(line 101) after CT10 polished with 0.5% Br_2-MeOH for 15 seconds..... 74
Figure 59. Comparison between as-grown defect density and as-grown defect depth... 75
Figure 60. SEM images of as-grown (a) CT6, (b) CT9 and (c) CT10 samples at 25000 magnification... 76
Figure 61. SEM images of as-grown (a) CT22, (b) CT24, (c) CT25, (d) CT26 and (c) CT27 samples at 25000 magnification... 77

Figure 62. Nomarski microscopy images of (a) as-grown surface, (b) E1 etched surface and (c) N2 etched surface for CT6 at 100x magnification. 81
Figure 63. Nomarski microscopy images of (a) as-grown surface, (b) E1 etched surface and (c) N2 etched surface for CT9 at 100x magnification. 81
Figure 64. Nomarski microscopy images of (a) as-grown surface, (b) E1 etched surface and (c) N2 etched surface for CT10 at 100x magnification. 81
Figure 65. Nomarski microscopy images of (a) as-grown surface, (b) E1 etched surface and (c) N2 etched surface for CT22 at 100x magnification. 82
Figure 66. Nomarski microscopy images of (a) as-grown surface, (b) E1 etched surface and (c) N2 etched surface for CT24 at 100x magnification. 82
Figure 67. Nomarski microscopy images of (a) as-grown surface, (b) E1 etched surface and (c) N2 etched surface for CT25 at 100x magnification. 83
Figure 68. Nomarski microscopy images of (a) as-grown surface, (b) E1 etched surface and (c) N2 etched surface for CT26 at 100x magnification. 83
Figure 69. Nomarski microscopy images of (a) as-grown surface, (b) E1 etched surface and (c) N2 etched surface for CT27 at 100x magnification. 83
Figure 70. CT6 AFM 2D topographical images of (a) and (b) length analysis and cross-section line analysis of pits after CT6-E4 etch; (c) and (d) length analysis and cross-section line analysis of pits after CT6-N2 etch. 84
Figure 71. CT9 AFM 2D topographical images (a) and (b) length analysis and cross-section line analysis of pits after CT9-E1; (c) and (d) length analysis and cross-section line analysis of pits after CT9-N2 etch. 85
Figure 72. CT10 AFM 2D topographical images of (a) and (b) length analysis and cross-section line analysis of pits after CT10-E1 etch; (c) and (d) length analysis and cross-section line analysis of pits after CT10-N2 etch. 86
Figure 73. CT26 AFM 2D topographical images of (a) and (b) length analysis and cross-section line analysis of pits after CT26-E1 etch; (c) and (d) length analysis and cross-section line analysis of pits after CT26-N2 etch. 87
Figure 74. (a) AFM 2D topographical images and (b) cross-sectional line analysis of XS1(line 195) of as-grown CT6; (c) AFM 2D topographical image and (d) cross-sectional line analysis of XS1(line 139) after 3 seconds Nakagawa ($20H_2O$:$20H_2O_2$:30HF) etched CT6. 88
Figure 75. (a) AFM 2D topographical images and (b) cross-sectional line analysis of XS1(line 165) of as-grown CT10; (c) AFM 2D topographical image and (d)

cross-sectional line analysis of XS1(line 165) after 3 seconds Nakagawa ($20H_2O$:$20H_2O_2$:30HF) etched CT10. 89

Figure 76. (a) AFM 2D topographical images and (b) cross-sectional line analysis of XS1(line 96) of as-grown CT24; (c) AFM 2D topographical image and (d) cross-sectional line analysis of XS1(line 135) after 3 seconds Nakagawa ($20H_2O$:$20H_2O_2$:30HF) etched CT24. 90

Figure 77. (a) AFM 2D topographical images and (b) cross-sectional line analysis of XS1(line 48) of as-grown CT25; (c) AFM 2D topographical image and (d) cross-sectional line analysis of XS1(line 160) after 3 seconds Nakagawa ($20H_2O$:$20H_2O_2$:30HF) etched CT25. 91

Figure 78. Comparison of 3 second Nakagawa EPD and as-grown defect density........ 92

Figure 79. SEM images of (a) as-grown surface of CT6, (b) after CT6-E4 etched sample, (c) after the CT6-N2. 93

Figure 80. SEM images of (a) as-grown surface of CT9, (b) after CT9-E1 etched sample and (c) after CT9-N2. 93

Figure 81. SEM images of (a) as-grown surface of CT10, (b) after CT10-E1 etched sample and (c) after CT10-N2. 94

Figure 82. SEM images of (a) as-grown surface of CT22, (b) after CT22-E1 etched sample and (c) after CT22-N2. 95

Figure 83. SEM images of (a) as-grown surface of CT24, (b) after CT24-E1 etched sample and (c) after CT24-N2. 95

Figure 84. SEM images of (a) as-grown surface of CT25, (b) after CT25-E1 etched sample and (c) after CT25-N2. 96

Figure 85. SEM images of (a) as-grown surface of CT26, (b) after CT26-E1 etched sample and (c) after CT26-N2. 96

Figure 86. SEM images of (a) as-grown surface of CT27, (b) after CT27-E1 etched sample and (c) after CT27-N2. 97

Figure 87. A comparison of (a) Everson and (b) Nakagawa etch pit shapes and their directions. 98

Figure 88. XRD-FWHM values versus flux ratio. 98

Figure 89. Everson EPD versus flux ratio. 99

Figure 90. Everson EPD versus calculated percentage error value from RHEED. 99

Figure 91. Everson EPD versus XRD-FWHM. 100

Figure 92. (a) Optical microscope image of 20x20 μm^2 scanned area on CT6-E4 etched sample, Raman intensity change of (b) A_1-symmetry mode of Te, (c) CdTe-like TO phonon mode, (d) CdTe-like LO phonon mode and (e) GaAs-like TO phonon mode. 102
Figure 93. (a) Optical microscope image of 20x20 μm^2 scanned area on CT6-N2 etched sample, Raman intensity change of (b) A_1-symmetry mode of Te, (c) CdTe-like TO phonon mode, (d) CdTe-like LO phonon mode, (e) GaAs-like TO phonon mode and (f) GaAs-like LO phonon mode..................................... 103
Figure 94. (a) Optical microscope image of 40x40 μm^2 scanned area on CT9-E1 etching performed sample, Raman intensity change of (b) A_1-symmetry mode of Te, (c) CdTe-like TO phonon mode, (d) CdTe-like LO phonon mode and (e) GaAs-like phonon mode.. 104
Figure 95. (a) Optical microscope image of 20x20μm^2 scanned area on CT9-N2 EPD etching performed sample, Raman intensity change of (b) A_1-symmetry mode of Te, (c) CdTe-like TO phonon mode, (d) CdTe-like LO phonon mode and (e) GaAs-like phonon mode. 105

LIST OF TABLES

Table **Page**

Table 1. Si, Ge and GaAs substrate properties for CdTe buffer layer. 8

Table 2. CdTe (211)B buffer layers growth parameters. 60

Table 3. XRD, SE and FTIR characterization results for CdTe films. 61

Table 4. Calculated lattice constants and percentage error values of buffer layers. 66

Table 5. AFM characterization results for as-grown CdTe buffer layers. 72

Table 6. Defect decoration methods, volume ratios, etching times and EPD values for CT6 and CT9. 79

Table 7. EPD results for different samples by applying E1 and N2 methods. 80

Table 8. A representative peak positions of phonon modes of as-grown CT6 and CT9. 101

Table 9. Raman intensity distribution of phonon modes of etched CT6 and CT9. 106

LIST OF ABBREVIATIONS

AFM	Atomic Force Microscopy
BCC	Body Centered Cubic
CdTe	Cadmium Telluride
CdZnTe	Cadmium Zinc Telluride
EPD	Etch Pit Density
FCC	Face Centered Cubic
FTIR	Fourier Transformation Infrared
FWHM	Full Width at Half Maximum
GaAs	Gallium Arsenide
IR	Infrared
LWIR	Long Wavelength Infrared
MBE	Molecular Beam Epitaxy
HgCdTe	Mercury Cadmium Telluride
MWIR	Mid Wavelength Infrared
ROIC	Read Out Integrated Circuit
RHEED	Reflection High Energy Electron Diffraction
SE	Spectroscopic Ellipsometry
SEM	Scanning Electron Microscopy
SC	Simple Cubic
SWIR	Small Wavelength Infrared

CHAPTER 1

INTRODUCTION

HgCdTe is one of the most important IR detector materials. No other material system yet offers a comparable performance for strategic applications. However, difficulties associated with suitable substrates prevent large format focal plane arrays. The lattice matched substrate, CdZnTe (with 4% Zn), has some issues. Besides being extremely expensive, it has large thermal mismatch with Si read out integrated circuit (ROIC) and it is very brittle material [1]. On the other hand, alternative substrates have been widely studied especially for MBE growth of HgCdTe [2]. Among these, Si and GaAs are the most promising ones and have made tremendous progress in recent years [3, 4]. They are low-cost, large area and have much less surface defects compared to CdZnTe. Surface dislocation density values of Si, GaAs and CdZnTe substrates are ~100 cm^{-2}, ~10^3 cm^{-2} and ~10^4 cm^{-2}, respectively [5]. However, there exists a large lattice parameter difference between HgCdTe and alternative substrates. In order to minimize the deleterious effects of the large lattice mismatch between the alternative substrates such as Si, Ge and GaAs and the epilayer, HgCdTe needs to be grown on a buffer layer including CdTe or CdZnTe [6, 7]. This lattice mismatch leads to a large number of misfit dislocations in epilayer. Most of these dislocations propagate into the growing film from the substrate interface. Surface defects of the buffer layer reduce the detector and focal plane array performance [8] of the HgCdTe epilayers grown on them. Hence, the crystal quality and dislocation density of CdTe grown on an alternative substrate needs to be analyzed for high performance HgCdTe infrared devices.

Wet chemical defect decoration etching is the most common process to reveal various kinds of defects especially those related to dislocations. Different etch techniques leave different pit shapes on the surface. The decoration etching creates etch pits at the end points of dislocations terminating at the surface due to the difference in the bond strength. In addition, crystal symmetry along the direction perpendicular to the surface can be monitored by the shape of the etch pits [9].

In this work, two different etch methods of Nakagawa and Everson on CdTe (211)B epilayers with expectedly high structural defect content grown on GaAs were

utilized to reveal and obtain areal density of defects related to dislocations and/or other type of defects. The Everson (which yields triangle-like shaped pits) and Nakagawa (which yields trapezoid-like shaped pits) etch pit densities were compared and analyzed from CdTe samples grown under different growth conditions. CdTe samples were characterized by using reflected high energy electron diffraction (RHEED) during the epitaxial growth. Atomic force microscopy (AFM), Nomarski microscopy, scanning electron microscopy (SEM) and Raman Spectroscopy were used to characterize the etching effects.

- In Chapter 2, gives brief background information about CdTe crystal properties. In addition, alternative substrates for CdTe, molecular beam epitaxial growth will be explained.
- In Chapter 3, gives background information about dislocation properties of CdTe such as zero, one and three dimensional defect types.
- In Chapter 4, defect decoration and characterization methods will be explained.
- In Chapter 5, *in-situ,* structural and optical characterization techniques such as AFM, Nomarski, SEM, RHEED and Raman Spectroscopy Mapping are given.
- In Chapter 6, experimental results and discussions of defect structure of molecular beam epitaxial grown CdTe buffer layers are given. Wet chemical etching procedure is explained in detail and two different etch methods are applied on CdTe (211)B epilayers. Etch pit density (EPD) results of these epilayers were compared with *in-situ* characterization results which are obtained by RHEED. Etched CdTe buffer layers are characterized by AFM, SEM, Nomarski and Raman spectroscopy mapping. Characterization results were discussed with regard to two different etch techniques.
- In Chapter 7, summary of results of this study, conclusions and ideas about future works are given.

CHAPTER 2

CADMIUM TELLURIDE CRYSTAL AND DISLOCATION PROPERTIES

2.1. Crystal Structure

2.1.1. Crystal Lattice

In an assembly of the atom or molecules arrange themselves in a regular three dimensional pattern where strong attractive forces are exerted. Imaginary points in space no need to form a crystal. To form a crystal structure, one needs a lattice and basis. Basis is the repeated unit, configuration of atoms attached to each lattice site to a form a crystal. CdTe epilayers have the zinc-blende crystal structure. In addition to the zinc-blende crystal structure, in this chapter simple cubic (SC), body-centered cubic (BCC) and face-centered cubic (FCC) structures will be briefly discussed.

2.1.1.1. Simple Cubic Lattice

SC is the simplest lattice structure in the cubic lattice system. SC lattice consists of a single type of atoms in which the coordinates of atoms (0,0,0) and distances between each of them are equal (Figure 1). In fact, distance between the atoms refer to the dimension of the smallest structure in the crystal lattice, is defined as lattice parameter. This smallest structure is also called as a unit cell which generates the full crystal by the repetition of itself under a proper combination of lattice parameters. The only example for SC lattice is Polonium (Po) crystal [10].

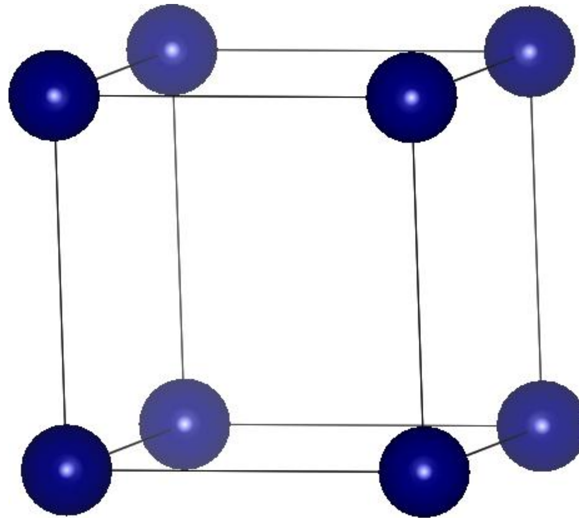

Figure 1. A schematic representation of SC lattice.

As mentioned above, the dimension of the unit cell is specified with lattice parameters. However, the orientation of the crystal plane needs a different argument. Crystal plane intersects the unit cell at some points in terms of lattice constants like a h'$\mathbf{a_1}$, k'$\mathbf{a_2}$, l'$\mathbf{a_3}$ (where $\mathbf{a_1}$, $\mathbf{a_2}$ and $\mathbf{a_3}$ are lattice constants and h', k' and l' are intersect points). Reciprocal values of the intersect points are 1/h', 1/k', 1/l'. The Miller indices h,k,l are obtained by multiplying these reciprocal values with their greatest common divisor. There are different notations of the Miller indices; [hkl] indicates the convention lattice vectors, (hkl) indicates the lattice planes, <hkl> indicates the family of lattice vectors and {hkl} indicates the family of lattice planes. Negative values of the miller indices can be shown as ā or –a.

2.1.1.2. Body Centered Cubic Lattice

BCC lattice structure contains of two atoms in each unit cell. The coordinates of atoms are (0,0,0) and (1/2,1/2,1/2) which is shown in Figure 2. Iron (Fe) crystal is the most common example for bcc lattice structure [11].

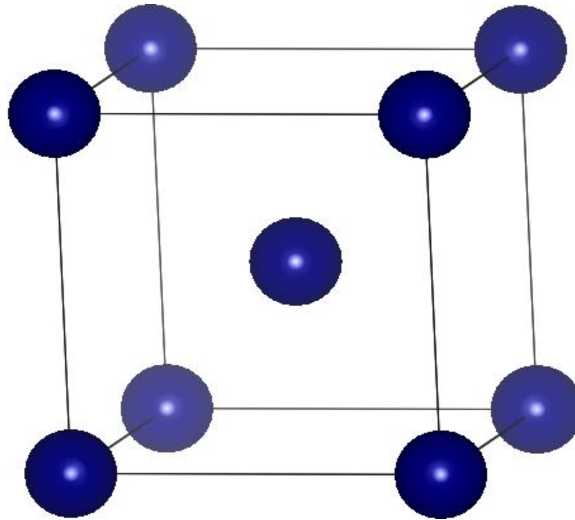

Figure 2. A schematic representation of BCC.

2.1.1.3. Face Centered Cubic Lattice

FCC contains four atoms in each unit cell. The coordinates of atoms are (0,0,0), (0,1/2,1/2), (1/2,0,1/2) and (1/2,1/2,0) as pictured in Figure 3. The NaCl is the most common example for FCC lattice structure [12].

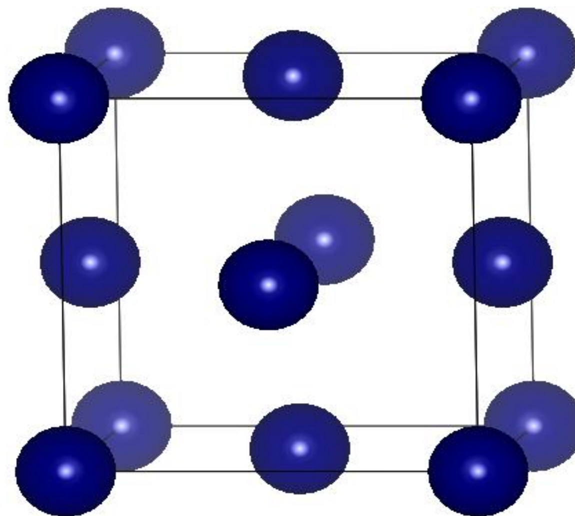

Figure 3. A schematic representation of FCC.

2.1.1.4. Zinc-Blende Lattice

CdTe has a zinc-blende lattice structure [13]. Cadmium (Cd) has a FCC lattice and four atoms in a unit cell. Also, Tellurium (Te) has a FCC lattice and again four atoms in a unit cell. It can be inferred that zinc-blende lattice consists of two FCC sub lattices. The coordinates of the Cd atoms are (0,0,0), (0,1/2,1/2), (1/2,0,1/2), (1/2,1/2,0) and Te atoms are (1/4,1/4,1/4), (1/4,3/4,3/4), (3/4,1/4,3/4), (3/4,3/4,1/4) (Figure 4. a and b, respectively). The combination of these two FCC lattice structure creates the final form of CdTe zinc-blende lattice which can be seen in Figure 4. c. For some theoretical explanations of zinc-blende lattice, it can be thought as a FCC lattice as practical and easy approach.

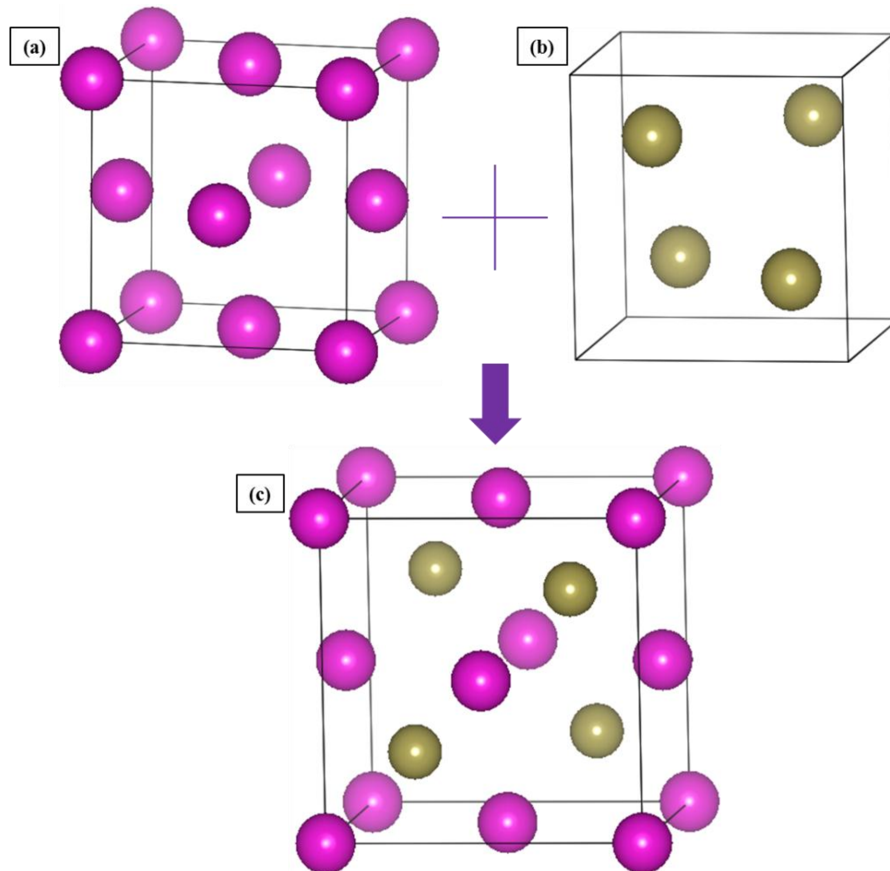

Figure 4. A schematic representation of FCC for (a) Cd atoms, (b) Te atoms and (c) zinc-blende lattice structure of CdTe.

2.2. Alternative Substrates of Cadmium Telluride

Epitaxial CdTe buffer layer growth has very important process for HgCdTe LWIR detector applications. The lattice and thermal expansion coefficient matched between CdTe buffer layer and alternative substrates are crucial research areas [2, 14]. In addition, alternative substrates can provide low-cost, large area and almost surface defect free structure. Table 1 shows the comparison between alternative substrates and CdTe which has a lattice constant of 6.48 Å [15] and a thermal expansion coefficient of $5.31 x 10^{-6}$ K^{-1} [15]. Si read out integrated circuits (ROIC) are very suitable with Si substrates. Furthermore, Si substrates have low-cost, large area and low etch pit densities with respect to Ge and GaAs substrates as can be seen in Table 1. However; Ge and GaAs could be better choices due to their lattice and thermal coefficient matching with CdTe. To grow uniform B-face CdTe (211) buffer layer, substrate crystal structure becomes significant factor. Therefore, GaAs substrate has a potential benefit because of its zinc-blende crystal structure and polar (211) surface. For all above mentioned reasons, GaAs is the ideal substrate for growing CdTe (211)B buffer layer.

Table 1. Si, Ge and GaAs substrate properties for CdTe buffer layer [5, 15, 16].

Substrates / Properties	Si	Ge	GaAs
Cost ($\$/cm^2$)	~1	~8	~5
Max. Size (cm^2)	~700	~180	~180
Structure	Diamond	Diamond	Zinc-blende
Lattice Parameter (Å)	5.43	5.66	5.65
Lattice Mismatch	19.36%	14.56%	14.66%
Etch Pit Density (cm^{-2})	10-100	$5x10^3$	10^3
Thermal Coefficient ($10^{-6} K^{-1}$)	2.6	5.8	5.8
Thermal Coefficient Mismatch	92.3%	-11.9%	-11.9%

2.3. Molecular Beam Epitaxial Growth of Cadmium Telluride

CdTe buffer layers on epi-ready GaAs (211)B substrates were grown by molecular beam epitaxy (MBE) for this work. The growth process of MBE includes several steps. Epi-ready GaAs substrates have protective oxide layers on their surfaces. Once, in the ultra-high vacuum growth chamber, oxide layers on the surface of epi-ready GaAs is thermally desorbed. After this step, temperature is cooled to grow CdTe nucleation layer. The nucleation layer growth step is important to suppress the formation of twin defects [17] and also to protect the crystal orientation of the surface. Finally, the substrate temperature is increased to the buffer layer growth temperature. During the oxide removal and growth steps of nucleation and buffer layers, *in-situ* RHEED patterns are monitored to observe the change of crystal quality and roughness of the surface. The source material As_4 is used for deoxidation and CdTe and Te_2 are used for growth steps. The mean free path of an atom is on the order of several meters to several kilometers under the ultra-high vacuum pressure (10^{-7} Torr – 10^{-10} Torr). In kinetic theory, the mean free path is the average distance between colliding particles. Therefore, the source materials can be thought as a beam of non-interacting particles. The flux (or molecular beam) of the source materials at the substrate position is measured by an ion-gauge as a pressure change, hence it is called as beam-equivalent pressure (BEP) for this reason. VI/II flux ratio on the material can be controlled by changing the temperature of the source materials.

CdTe (211)B buffer layers are used and (211) orientation is preferred for several reasons. For LWIR detection systems, HgCdTe is the most important material. In the past, CdTe material growth was carried on lower index planes such as (111), (100) and (110) for epitaxially growth. To grow the HgCdTe material from CdTe buffer layers, CdTe (111)B oriented epilayers have been shown to require four or five time less Hg flux [18]. Although, (111)B orientation leads to twinning defects which reduce the detector and focal plane array (FPA) performance [19]. (211)B oriented planes were found to be giving material of higher quality, lower surface defects and require less Hg flux than lower index planes.

After the growth, the CdTe buffer layers are removed from MBE system and subjected to several characterization including the crystal quality and surface morphology determination by using different techniques. The optical properties and

thicknesses of the samples were characterized by *ex-situ* SE and FTIR. To quantify the crystal quality of buffer layers, EPD and XRD methods were performed. The surface morphologies of the CdTe epilayers were analyzed by using AFM, SEM and Nomarski microscopy for as-grown and chemically etched samples.

2.4. Uses of Cadmium Telluride

CdTe is a semiconductor material which is formed by alloying cadmium and tellurium. This material is used to make thin film solar cells, infrared optical materials for optical windows and lenses, electro-optic modulators and infrared detection windows [20]. Particular interest of this work is the infrared detection application of CdTe which can be alloyed with mercury to form one of the most important materials of infrared detectors [21-24]. Due to the transmission range of the infrared (IR) spectra through atmosphere, IR wavelengths are divided into three main windows: short wavelength infrared (SWIR) which has transmission range 1-3 µm, middle wavelength infrared (MWIR) which has transmission range 3-5 µm and long wavelength infrared (LWIR) which has transmission range 8-12 µm as shown in Figure 5.

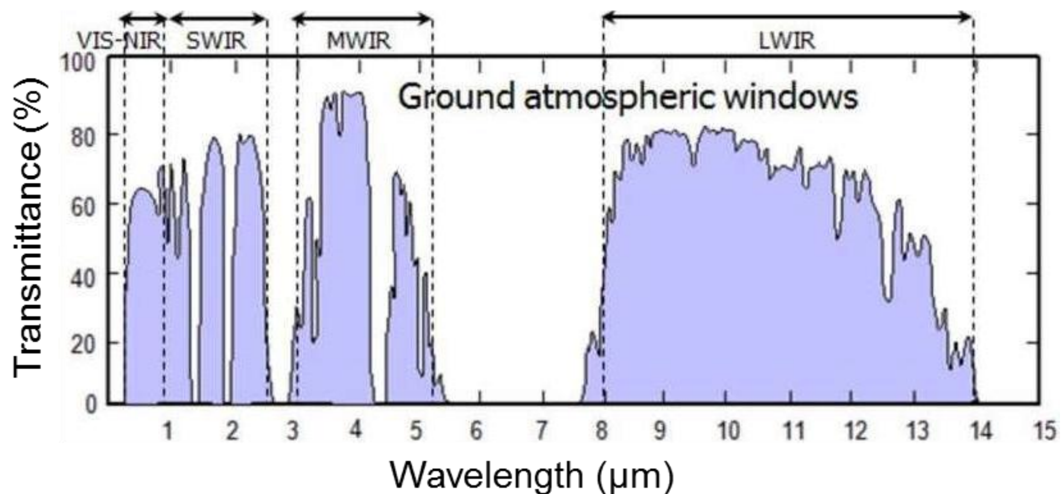

Figure 5. Range of the transmission of the IR spectra ground atmospheric windows [25].

In general, HgCdTe is grown on the alternative substrate materials such as Si, GaAs or Ge with CdTe epitaxial buffer layer. CdTe is very suitable material for above application areas with its 1-30 µm transmission ranges [20]. LWIR detector applications

have the ideal range for night vision imaging systems. According to Wien's law, hotter objects emit more than their energy at shorter wavelengths, objects emit the black body source at room temperature (300 K) with a peak at a wavelength (λ_{max}=A/T, A= 2898 μm K) of about 9.7 μm [26]. Due to this, LWIR wavelengths are suitable for imaging room temperature objects and penetrating through some different environments such as dust or vapor. Hence, LWIR technology is crucial for astronomy, military and security applications.

2.5. Polar Surfaces of Cadmium Telluride

Compound semiconductors such as GaAs, CdTe, InSb, etc. have surface polarity which depends on atom termination on the surface. Crystallographic polarity of CdTe can be defined as A-terminated (Cd) and B-terminated (Te) surfaces [27]. For example, (211) plane surface must be A-terminated or B-terminated due to its bonding structure (Figure 6). If the number of Cd and Te atoms on the surfaces are equal to each other, this surfaces are called non-polar such as (110) and (100) for CdTe [28]. Crystallographic polarity is so important to determine the wet chemical etching technique, because the surface morphology of the CdTe compound semiconductor depends on whether the A-terminated or B-terminated surface has been used.

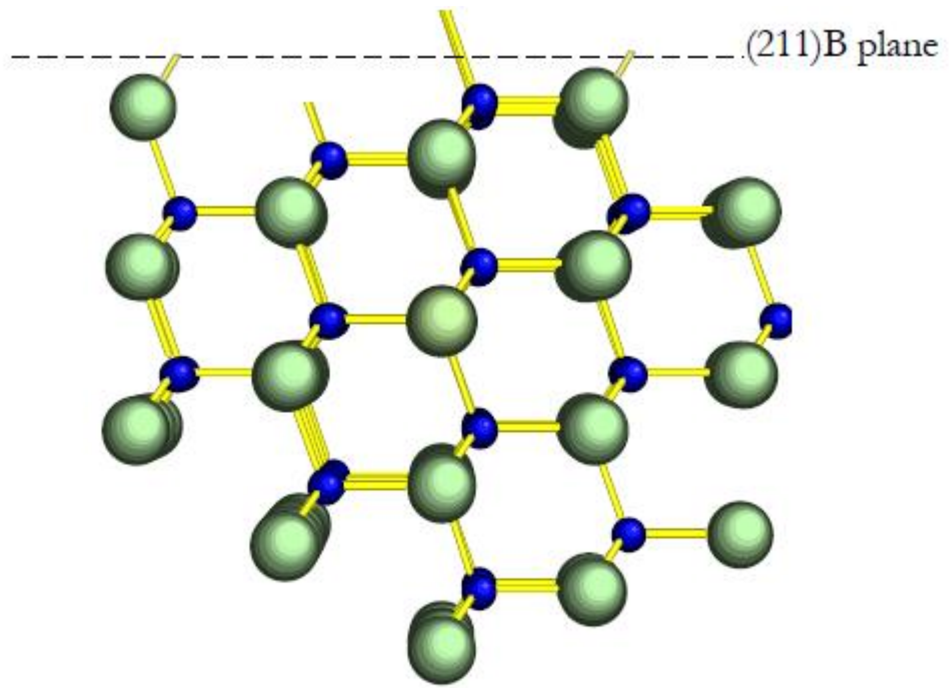

Figure 6. B-terminated (211) surface of CdTe [29].

CHAPTER 3

DEFECTS IN CRYSTALS

3.1. Zero Dimensional Defects

The crystal structures are affected from zero-dimensional defects which are also called point defects in accordance with their surface polarity.

There are several different types of point defects that can be found in a crystal. The most common types of point imperfections are interstitials, vacancies, substitutions and impurities. They will be briefly described in this section.

An atom with in crystal lattice which is not found at a proper lattice place, but rather it exists in the empty space between lattice points is called an interstitial defect. If atom is the same species atom with the regular lattice atoms, it is called self-interstitials. Smaller atoms such as carbon, nitrogen, oxygen, hydrogen, etc. are usually found at interstitial positions. A vacancy type point defect occurs when there is an empty atom in the lattice site. Especially, at high temperature (i.e. high annealing temperature), many of atoms will have broken atomic bonds similar to an interstitial atoms and move away from their lattice positions and leave behind vacant lattice sites. The probability of finding a vacant lattice site at the thermal equilibrium is proportional to a Boltzmann factor [30];

$$\boldsymbol{P = Ae^{\left(-E_v/k_BT\right)}} \tag{3. 1}$$

where E_v is the energy needed to form a vacant defect, k_B is the Boltzmann constant, A is constant and T is the absolute temperature. If N_s is the number of lattice sites, the number of vacancies N_v can be found [31],

$$\boldsymbol{\frac{N_v}{N_s - N_v} = e^{\left(-E_v/k_BT\right)}}. \tag{3. 2}$$

In reality, the number of vacancies is much smaller than the number of regular lattice sites ($N_v \ll N_s$). Therefore, the above equation can approximated as [31],

$$\boldsymbol{\frac{N_v}{N_s} = e^{\left(-E_v/k_BT\right)}}. \tag{3. 3}$$

Hence, for a lower temperature; the percentage of vacancies is reduced. If the crystal is cooled suddenly, e.g. after the high temperature growth conditions, the number of vacancies will be higher than the equilibrium value [31].

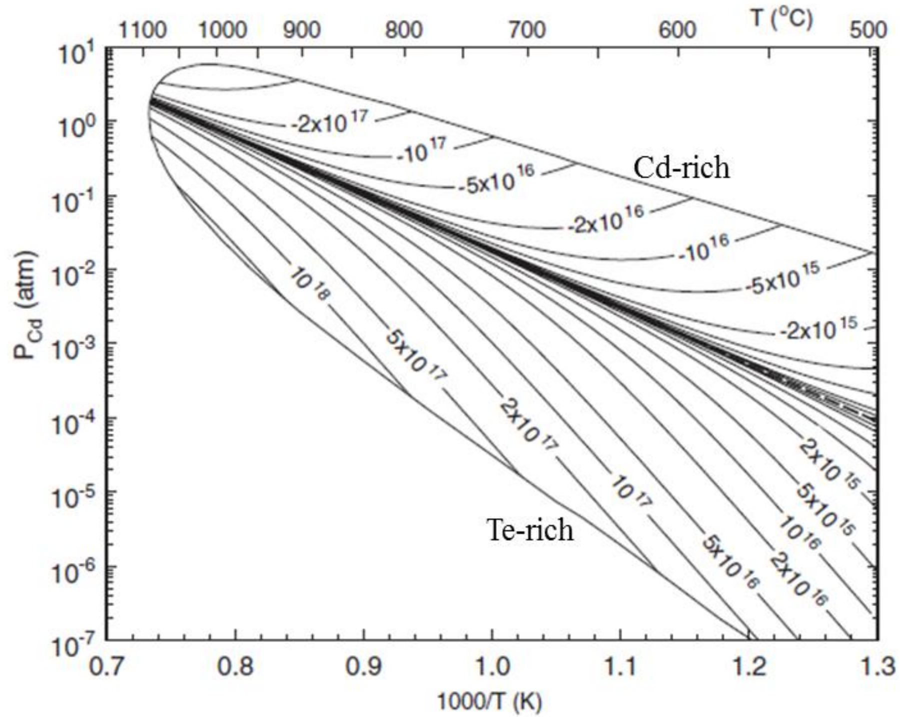

Figure 7. P-T curve and isohole concentration lines for CdTe for temperature range from 500 to 1100 K [32].

The epitaxial growth on the B face of CdTe occurs under Te-rich conditions. The higher Cd vapor pressure than that of Te_2 leads to form the loss of Cd during the crystal growth [33]. Hence, larger numbers of Cd-vacancies at high anneal temperature there will be a high concentration of vacancies. However; the number of vacancies will be lower when annealing can be done under Cd-rich conditions [32]. In Figure 7, the upper bound of the curve shows the Cd-vapor pressure and the lower bound shows the lower limit of Cd over pressure.

The other two forms of point defects substitutions and impurities occur when a foreign atom resides in the lattice sites. Although, small foreign atoms are often found in interstitial sites (interstitial impurities), larger ones are usually substitutional (substitutional defects). If a foreign atom is occupying a lattice point, it is called impurity defect. All point defect types are shown in Figure 8, the arrows in this figure indicate the local stresses by the point defects.

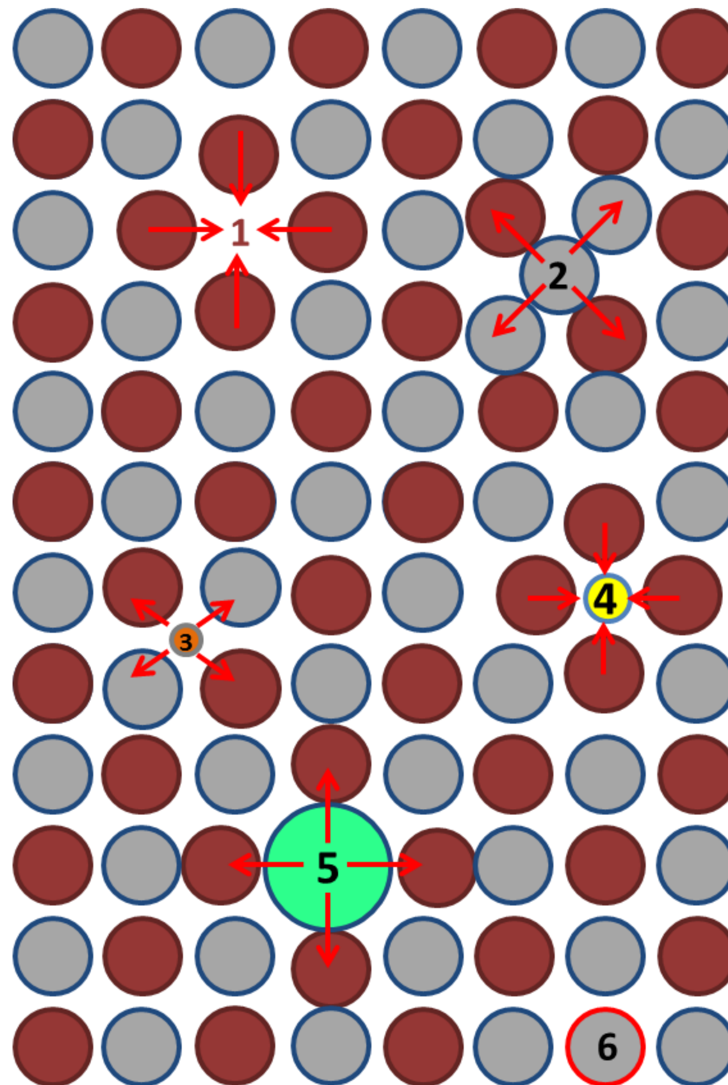

Figure 8. Schematic of different types of point defects in a crystal. (1) vacancy, (2) self-interstitial, (3) interstitial impurity, (4) and (5) substitutional impurities and (6) impurity defect (adapted from [34]).

3.2. One Dimensional Defects

One-dimensional defects are lines along which the crystal lattice is deformed. These defects are called dislocations. The theory of defects from the elastic fields in a solid was firstly developed by Vito Volterra in 1907 [35]. The term of dislocation referring to a defect on the atomic scale was explained by Taylor, Orowan and Polanyi in 1934 [36-38].

When the crystal is deformed under an applied stress, large numbers of atoms is broken and reconnected at another location. This process is called plastic deformation.

The elastic deformation accrues again under an applied stress, but unlike the plastic deformation, large numbers of atoms are not broken but strained and distorted. There are three different dislocation types; edge dislocation, screw dislocation and mixed dislocation.

3.2.1. Edge Dislocation

Edge dislocation is a one dimensional defect that origins around the line. The missing part of the crystal is formed the extra of plane. Figure 9 (a) and (b) illustrates the edge dislocation formation. According to this figure, edge dislocation is formed by making a planar cut in a crystal lattice. Henceforward, cutting part of the crystal inserts or removes in the direction as shown in Figure 9 (a). Matching the material in a strained region around the cutting line demands that excess part be gathered at the line. Figure 9 (b) shows the linear defect structure which is called an edge dislocation.

Edge dislocation is a kind of the plastic deformation which changes the shape of a body without changing its volume. Hence, the crystal structure remains the same. The symbol "⊥" is used to demonstrate a positive dislocation (extra fractional plane) and "⊤" is used to demonstrate a negative dislocation (missing fractional plane) [39].

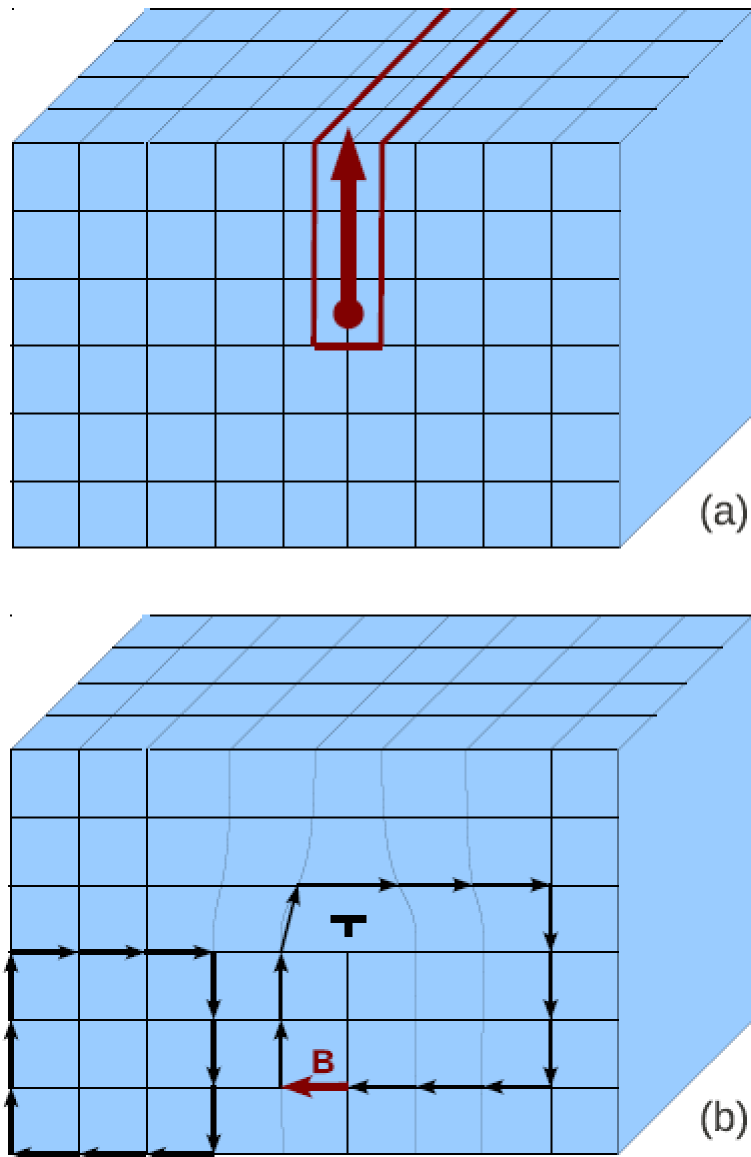

Figure 9. Diagram of an edge dislocation [18].

3.2.2. Screw Dislocation

There is a second main type of one-dimensional dislocation which is called as a screw dislocation. Cutting in a perfect crystal along a plane under applying a shear stress can be seen in a Figure 10 (a). After this cutting, the screw dislocation is formed parallel to the direction in which the crystal is being displaced because of a shear stress (Figure 10 (b)). The symbol ↻ sometimes used to represent screw dislocation [40].

The differences between edge and screw dislocations are their geometries and directions of motions under an applied force. For a screw dislocation, the Burgers vector

is parallel to the dislocation direction and both of them are also parallel with each other in any plane. Hence, a screw dislocation direction can be observed in any plane in contrast to an edge dislocation [41].

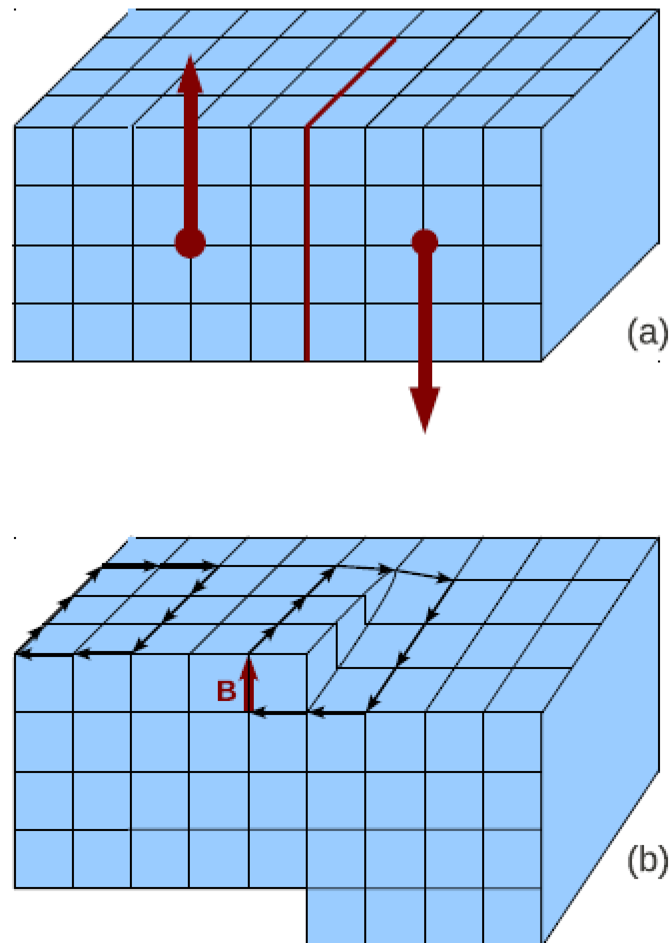

Figure 10. Diagram of a screw dislocation [18].

3.2.3. Mixed Dislocation

The last one-dimensional dislocation type is a mixed type dislocation. A mixed type dislocation can be described that the dislocation line direction and Burgers vector are neither perpendicular (edge-type dislocation) nor parallel (screw-type dislocation) with each other, but combination of both types. All one-dimensional dislocation types are schematically represented in Figure 11. The lattice distortion can be understood from where the crystal is strained. In order to understand a one-dimensional dislocation

totally that has edge, screw and mixed, Burgers vector expression must be made in detail.

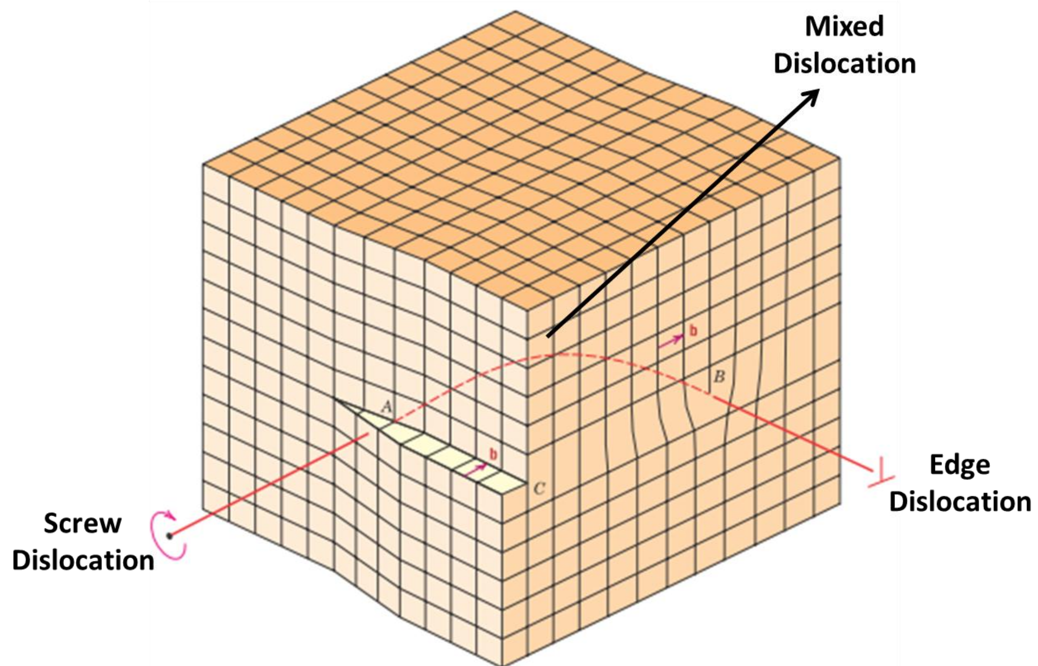

Figure 11. Schematic of edge, screw and mixed dislocation types [42].

3.2.4. Burgers Circuit

To describe the magnitude and the direction of the lattice distortion which is caused by a dislocation is explained in terms of a Burgers vector, demonstrated by a **b** [42].

To compose a Burgers circuit, there is a perfect crystal lattice with a clockwise closed circuit which is constructed by using arrows in Figure 12 (a), when the same circuit wanted to compose by linking crystal lattice sites, the circuit encloses a dislocation. Hence, it will not close. An extra vector is required to form and close the circuit which is called a Burgers vector (Figure 12 (b)). The net displacement of the complete circuit with respect to a perfect crystal lattice is also represented by a Burgers vector.

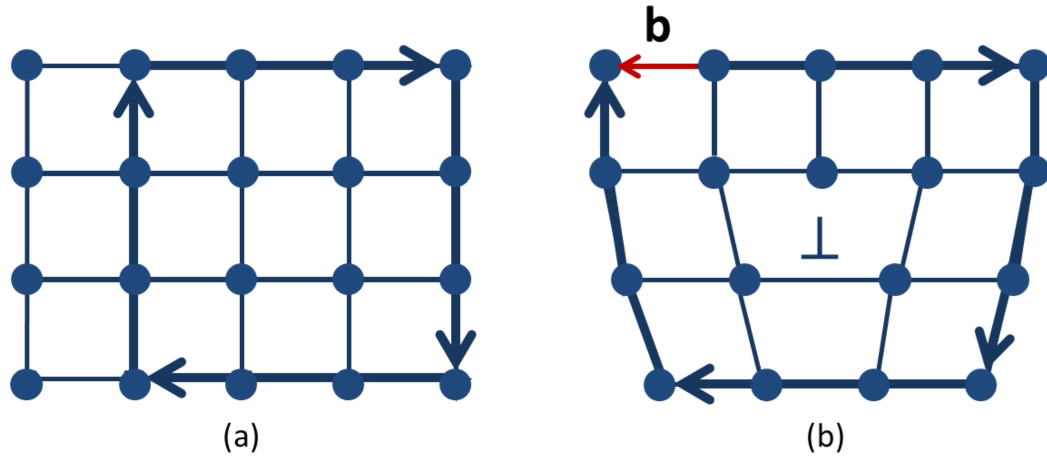

Figure 12. Burgers circuit and Burgers vector representation (adapted from [43]).

3.2.5. Calculation of Dislocation Stress Strain and Energy

A dislocation is the result of large number of atoms is broken or missing in a crystal structure. In some cases, stress and strain in a continuum field are proportional with each other which are called elastic deformation [44]. However, in general, elastic deformation persists only to strains, so stress and strain proportionality is broken irreversibly. This condition causes a plastic deformation [45]. This part will be examined the stress, strain and self-energy calculations of screw, edge and mixed dislocations. The accepted way to calculate the stress and strain is Volterra construction or Volterra tube [46] demonstration as shown in Figure 15 and Figure 16. Volterra construction or tube contains a cylindrical shell. A piece of this cylindrical shell is cut down the side. The area of cutting part is glided and reconnects again. Therefore, stress and strain formation of dislocations can be shown by using this cylindrical shell.

To define the orthogonal Cartesian coordinates, let x_i (i=1,2,3) remark the stresses in a body with using $\sigma_{ij}.\sigma_{ij}$. The i th component of the force per unit area on a plane as demonstrate in Figure 13. There is a rotational equilibrium of the element so that no net toque on the element;

$$\boldsymbol{\sigma_{ij} = \sigma_{ji}} \tag{3. 4}$$

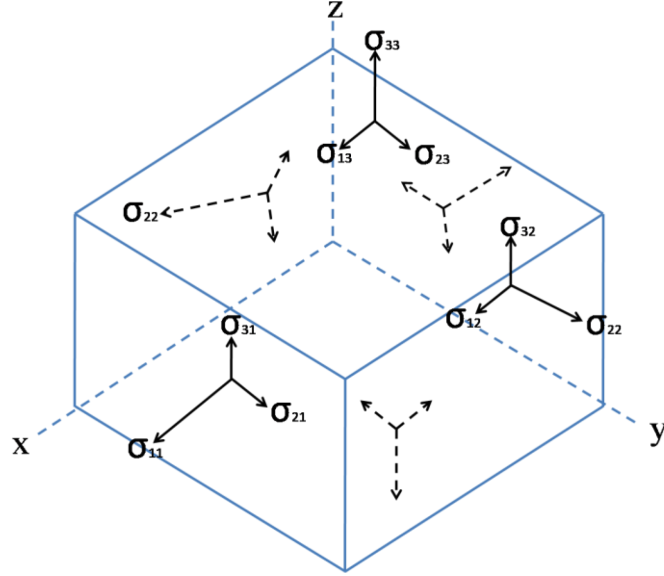

Figure 13. Components of stress on the faces of an elemental cube.

The displacement of a point in a strained body from its position in the unstrained state [47] can be shown by the vector $\mathbf{U_i}$. Now, the strains are defined as [48];

$$\epsilon_{ij} = \frac{1}{2}\left(\frac{\partial U_i}{\partial X_j} + \frac{\partial U_j}{\partial X_i}\right). \tag{3. 5}$$

For i ≠ j, that is, for shear strains;

$$\gamma_{ij} = 2\epsilon_{ij}. \tag{3. 6}$$

Due to the Figure 14, the shear strain is related to the angle of shear;

$$\gamma_{12} = \emptyset_1 + \emptyset_2. \tag{3. 7}$$

For small distortions $\partial U_i / \partial X_j$, the stresses depend linearly on deformation. Stiff rotations of an element cannot give rise;

$$\omega_{ij} = \frac{\partial U_i}{\partial X_j} - \frac{\partial U_j}{\partial X_i} = 0 \;\rightarrow\; \frac{\partial U_i}{\partial X_j} = \frac{\partial U_j}{\partial X_i}. \tag{3. 8}$$

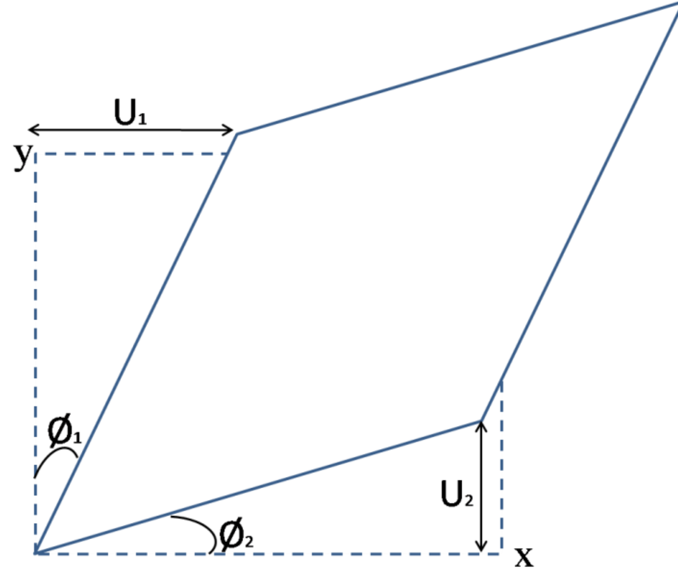

Figure 14. Pure shear of an area element in the x-y plane.

When the internal torque is absent, the stresses depend only on the stains;

$$\boldsymbol{\sigma_{ij} = c_{ijkl}\epsilon_{kl}}. \tag{3. 9}$$

C_{ijkl} is the elastic constant and property of the elastic constant is;

$$\boldsymbol{c_{ijkl} = c_{jikl} = c_{ijlk} = c_{jilk}}. \tag{3. 10}$$

Due to the above equations;

$$\boldsymbol{\epsilon_{kl} = \frac{\partial U_k}{\partial X_l} \rightarrow \sigma_{ij} = c_{ijkl}\frac{\partial U_k}{\partial X_l}}. \tag{3. 11}$$

If the coordinate axes are written in compatible with cubic axes, the rotational symmetry becomes very important. In that, cubic crystal structures are invariant under the symmetry to 90° rotations about cubic axes. Hence, the formulations can be rewritten such as $C_{iiii}=C_{11}$, $C_{iijj}=C_{12}$ for i≠j and $C_{ijij}=C_{44}$ for i≠j. All other constants are equal to zero (i.e. $C_{iiij}=0$). Due to the matrix notation [48], the relation between stress and strain can be reduced to simple form;

$$\sigma_{11} = c_{11}\epsilon_{11} + c_{12}\epsilon_{22} + c_{12}\epsilon_{33}, \qquad \sigma_{23} = 2c_{44}\epsilon_{23}$$

$$\boldsymbol{\sigma_{22} = c_{12}\epsilon_{11} + c_{11}\epsilon_{22} + c_{12}\epsilon_{33}, \qquad \sigma_{31} = 2c_{44}\epsilon_{31}} \tag{3. 12}$$

$$\sigma_{33} = c_{12}\epsilon_{11} + c_{12}\epsilon_{22} + c_{11}\epsilon_{33}, \qquad \sigma_{12} = 2c_{44}\epsilon_{12}$$

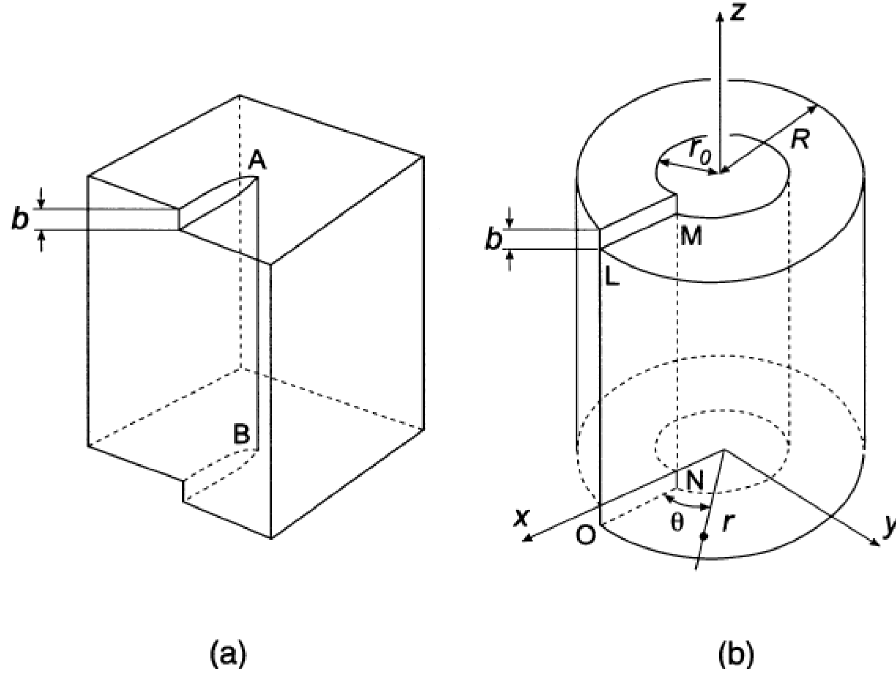

Figure 15. (a) Screw dislocation formation in a crystal structure and (b) representation by using cylindrical shell [47].

An annular slit was cut in the Volterra tube representation of a perfect crystal parallel to the z-axis. Free surfaces of the Volterra tube displaced rigidly with respect to each other by distance a Burger vector, **b**, as shown in Figure 15. It can be seen from this figure, there are no displacement in the x and y directions (U_x=U_y=0). The displacement increases uniformly from zero to **b** which occurs only z-direction [47, 48].

$$U_z = \frac{b\theta}{2\pi} = \frac{b}{2\pi}\tan^{-1}\left(\frac{y}{x}\right). \tag{3. 13}$$

Using equation 3.5 which is written in accordance with standard elastic theory, the strain can be determined to be

$$\epsilon_{xx} = \epsilon_{yy} = \epsilon_{zz} = \epsilon_{xy} = \epsilon_{yx} = 0$$

$$\epsilon_{xz} = \epsilon_{zx} = \frac{-b}{4\pi}\frac{y}{(x^2+y^2)} = \frac{-b}{4\pi}\frac{\sin\theta}{r} \tag{3. 14}$$

$$\epsilon_{yz} = \epsilon_{zy} = \frac{-b}{4\pi}\frac{x}{(x^2+y^2)} = \frac{-b}{4\pi}\frac{\cos\theta}{r}$$

From the above strain results, the stresses can also be determined as

$$\sigma_{xx} = \sigma_{yy} = \sigma_{zz} = \sigma_{xy} = \sigma_{yx} = 0$$

$$\sigma_{xz} = \sigma_{zx} = \frac{-\mu b}{4\pi}\frac{y}{(x^2+y^2)} = \frac{-\mu b}{4\pi}\frac{\sin\theta}{r} \tag{3. 15}$$

$$\sigma_{yz} = \sigma_{zy} = \frac{-\mu b}{4\pi}\frac{x}{(x^2+y^2)} = \frac{-\mu b}{4\pi}\frac{\cos\theta}{r}.$$

where μ is the shear modulus.

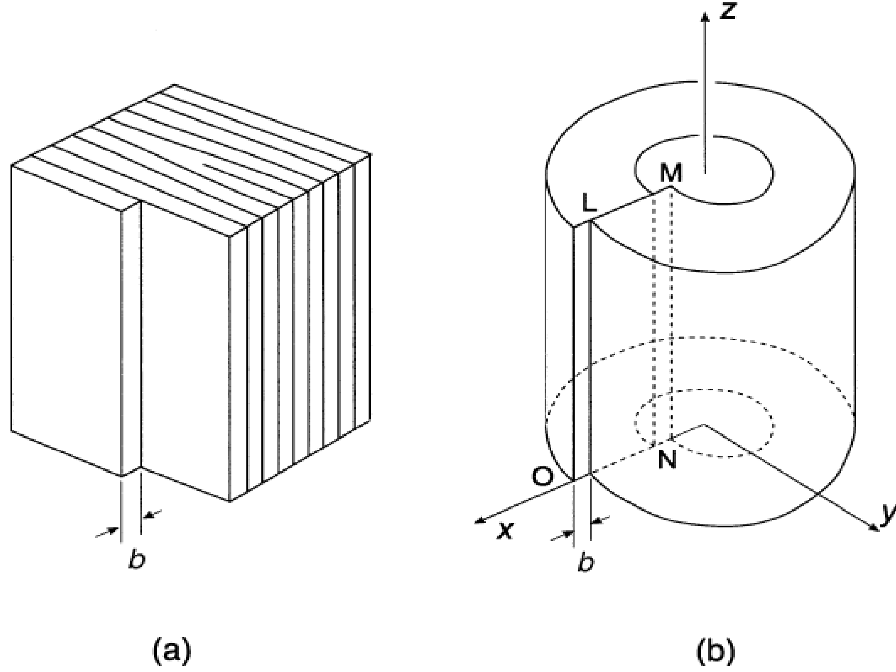

Figure 16. (a) Edge dislocation formation in a crystal structure and (b) representation by using cylindrical shell [47].

The stress and strain calculation of edge dislocation is more complicated and difficult than the screw dislocation equations. Therefore, the proofs of the stress and strain equations are skipped. The resulting strain equations are [47],

$$\epsilon_{zz} = \epsilon_{xz} = \epsilon_{yz} = 0 \tag{3. 16}$$

$$\epsilon_{xx} = \frac{by}{2\pi}\frac{\mu y^2 + (2\lambda+\mu)x^2}{(\lambda+2\mu)(x^2+y^2)^2}$$

$$\epsilon_{yy} = \frac{by}{2\pi}\frac{(2\lambda+\mu)x^2 - \mu y^2}{(\lambda+2\mu)(x^2+y^2)^2}$$

$$\epsilon_{xy} = \frac{b}{2\pi(1-\nu)}\frac{x(x^2-y^2)}{(x^2+y^2)^2}.$$

The stresses which are calculated from above strain equations are determined as;

$$\sigma_{xz} = \sigma_{yz} = 0$$

$$\sigma_{xx} = \frac{\mu b}{2\pi(1-\nu)} \frac{y(3x^2 + y^2)}{(x^2 + y^2)^2}$$

$$\sigma_{yy} = -\frac{\mu b}{2\pi(1-\nu)} \frac{y(x^2 - y^2)}{(x^2 + y^2)^2} \quad (3.\ 17)$$

$$\sigma_{zz} = \nu(\sigma_{xx} + \sigma_{yy}) = \frac{\mu \nu b y}{\pi(1-\nu)(x^2 + y^2)}$$

$$\sigma_{xy} = -\frac{\mu b}{2\pi(1-\nu)} \frac{x(x^2 - y^2)}{(x^2 + y^2)^2}.$$

where λ is Lamè constant and ν is Poisson's ratio.

The energy of a dislocation is formed from the elastic part which is contained the elastic field energy and the core energy. The particular form of strain energy for an elastic structure which is stored in a unit volume of strained material can be written as [49];

$$U = \frac{1}{2}\left(\sigma_{xx}\epsilon_{xx} + \sigma_{yy}\epsilon_{yy} + \sigma_{zz}\epsilon_{zz} + \sigma_{xy}\epsilon_{xy} + \sigma_{yz}\epsilon_{yz} + \sigma_{zx}\epsilon_{zx}\right). \quad (3.\ 18)$$

The circumference of a cylindrical shell which is shown in Figure 15 for screw dislocation is 2πr. The circumference has been interrupted by an amount of the Burger vector, b. Therefore, shear strain can be written amount of the Burger vector over the circumference of a cylindrical shell (e = b/2πr). In an elastic continuum theory, this shear strain can be modified such as;

$$\sigma = \mu e = \frac{\mu b}{2\pi r}. \quad (3.\ 19)$$

The elastic energy stored in small element of volume per unit length of the cylindrical shell is

$$dE_s = \mu e^2 dV = \mu \left(\frac{b}{2\pi r}\right)^2 r dr = \frac{\mu b^2}{4\pi} \frac{dr}{r}. \quad (3.\ 20)$$

The integration limit changes from r_0 to R which is the outer radius of dislocation

$$\int_{r_0}^{R} dE_s = E_s \rightarrow E_s = \int_{r_0}^{R} \frac{\mu b^2}{4\pi} \frac{dr}{r} = \frac{\mu b^2}{4\pi} \int_{r_0}^{R} \frac{dr}{r} \quad (3.\ 21)$$

$$\boldsymbol{E_s = \frac{\mu b^2}{4\pi} \ln\left(\frac{R}{r_0}\right)} \quad (3.\,22)$$

To obtain energy of an edge dislocation is more complicated than screw one. The result of the total elastic energy of an edge dislocation is;

$$\boldsymbol{E_e = \frac{\mu b^2}{4\pi(1-\nu)} \int_{r_0}^{R} \frac{dx}{x} = \frac{\mu b^2}{4\pi(1-\nu)} \ln\left(\frac{R}{r_0}\right).} \quad (3.\,23)$$

The only difference between energy of a screw dislocation and edge dislocation is the factor (1-ν). Where ν is the Poisson ratio and this ratio is nearly equal to 0.3 for most crystals [50]. Poisson ratio ν = 0.41 and the energy difference factor (1-ν) = 1.7 for CdTe [51]. The two dislocations can be assumed that have nearly the same energy.

As mentioned before, if the angle between the Burgers vector and dislocation line is equal to zero, it is a screw dislocation and if the angle is equal to 90°, it is an edge dislocation. Otherwise, the combination of a screw and an edge dislocation is a mixed dislocation. Due to the superposition principle, the energy of a mixed dislocation can be written as [18],

$$\boldsymbol{E_m = \frac{\mu b^2}{4\pi(1-\nu)} (1 - \nu cos^2\theta) \ln\frac{R}{r_0}.} \quad (3.\,24)$$

3.2.6. Motion of Dislocation

At an atomistic or on a microscopic scale, dislocations and the movement of large number of atoms are the results of irreversible plastic deformation. There two different types of motion of dislocations. First one is conservative motion or glide which is the consequence of the movement of atomic planes in the crystalline surface. Therefore, the movement of atomic planes causes to glissade from one atomic plane to another. Conservative dislocation motion occurs when the crystal is deformed under an applied stress. Hence, it can be understood that plastic deformation results from slip on parallel atomic crystal planes. The meaning of the "conservative" word is that movement of dislocation required the amount of energy and this energy is also equal to reconstitute the atomic bonds. Thereby, energy conservation may be mentioned for glide motion. This kind of motion has a small temperature dependence, because strongly stress dependence which vary with temperature.

As mentioned above, glide motion is the result of slip on parallel crystal planes. Slip becomes clear with plastic deformation approachment. Slip can be understood on

parallel atomic crystal planes which are substantially called slip planes. Slip planes consist of the highest density planes of crystal, in case of the face centered cubic and zincblende crystal structure the slip planes are {111} plane. Direction of slip has the same direction with slip plane regarding to shortest translation lattice vectors. FCC and zinblende crystal structure have <110> slip direction. For conservative or glide motion, both line vector (**t**) and Burgers vector (**b**) must lengthen on a slip plane. CdTe material has the zincblende crystal structure and slip plane and slip directions are {111} and <110> [52]. Slip system contains both a slip plane and a slip direction. FCC and zincblende (CdTe) crystal structure have four {111} planes with three <110> directions in each, so have twelve {111}<110> slip systems as can be seen in Figure 17.

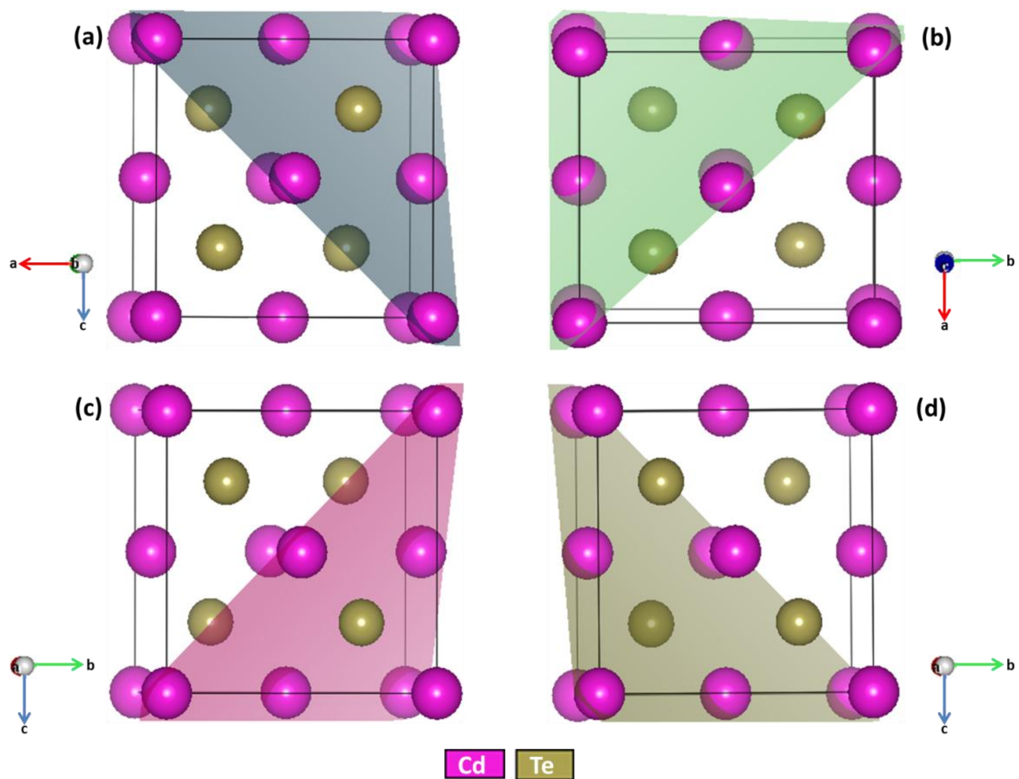

Figure 17. CdTe slip system configuration. (a) {111} slip plane with <0-11><10-1><-110> slip directions, (b) {-1-11} slip plane with <011><-101><1-10> slip directions, (c) {-111} slip plane with <0-11><-10-1><110> slip directions and (d) {1-11} slip plane with <011><10-1><-1-10> slip directions.

When the dislocation motion is observed for screw, edge and mixed dislocation types, the main difference between edge and screw dislocations is direction of motions

under an applied force. As is known, for edge dislocations, the Burgers vector is perpendicular to dislocation direction or line vector. It means that the motion of edge dislocation occurs on a unique slip plane (Figure 18). By the reason of the edge component of the mixed dislocation, in the same way that previous situation, mixed dislocation have a unique slip plane. However; the Burgers vector is parallel to the line vector for screw dislocations. Thus, screw dislocations do not have a well-defined slip plane. As a consequence, screw dislocations can glide in any close space vector, while mixed and edge dislocations can glide along a single vector.

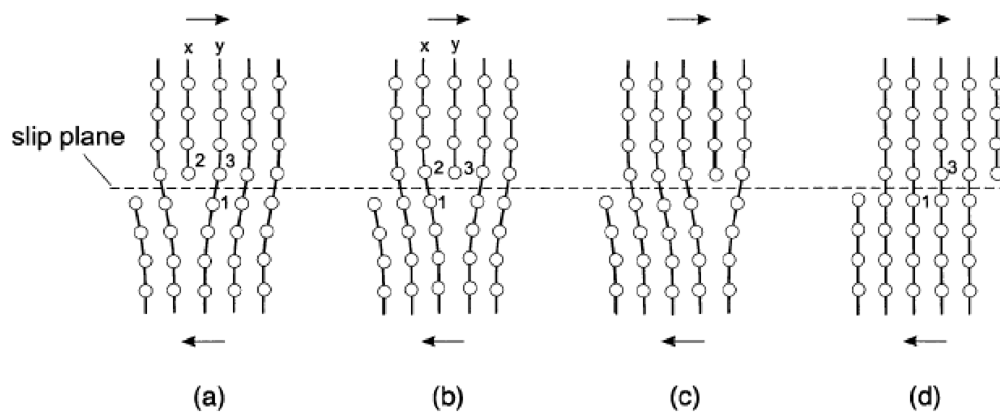

Figure 18. An example of a conservative dislocation motion is motion of an edge dislocation (arrows show the applied shear stress) [47].

Unlike the conservative motion, non-conservative motion or climb consists of a diffusion of point defects to a dislocation. In other words, an edge dislocation moves out of slip plane to climb. This kind of motion with two different types can be seen in Figure 19. A vacancy type point defect diffuses to an edge dislocation to form a positive climb (Figure 19.a). The crystal plane narrows perpendicular to the extra half plane of atoms. The opposite case is that an interstitial type of point defect diffuses towards the dislocation to form negative climb (Figure 19.b). The crystal plane enlarges in the direction perpendicular to the half plane of atoms, because negative climb contains an extra atom to the half plane. Non-conservative motions or climb depend strongly temperature and weakly stress. In that, point defect types, concentration and mobility are also highly temperature dependent.

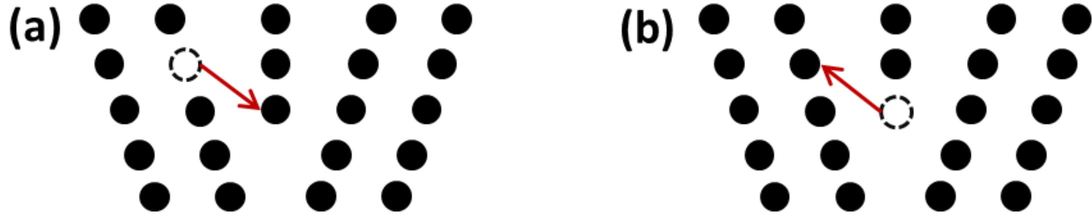

Figure 19. Schematic of (a) positive and (b) negative types of climb.

If CdTe material is examined for dislocation motion, Cd vacancies are mentioned in point defect part. Symmetric diffusion path of a Cd vacancy is given as 1.83 eV and the rate-limiting barrier for Cd interstitials is given as 0.33 eV in CdTe [53]. Diffusion path or diffusion barrier terms refer to the diffusion activation energy. Formation of new vacancies is strongly temperature dependent especially growth and annealing steps of epitaxial growth. If an applied stress is greater than critical shear stress (CRSS), dislocation motion will occur. The calculation of CRSS for CdTe [54];

$$\boldsymbol{CRSS = 12.25e^{-0.0029T}\ \ (MPa)} \tag{3. 25}$$

The CdTe buffer layer growth temperature is 300°C and annealing temperature is 390°C in our laboratory. Due to these temperatures, the minimum shear stress of CdTe to form a dislocation motion can be found as CRSS ≈ 1.93─2.48 MPa.

3.3. Two Dimensional Defects

Two-dimensional defects include planar defects which are fundamentally boundaries. There are five different kinds of two-dimensional defects: external surfaces, grain boundaries, twin boundaries, stacking faults and phase boundaries. These all defects have two common features. In a regular crystal lattice, they are surface defects which have specific atomic structure with respect to crystal orientation. Furthermore, the energy per unit area is equal to surface tension, so they have a positive energy.

External surface is one of the planar surface types. In this sort of defect, surface atoms are not bonded with each other and have higher surface energy than the bulk atoms. Therefore, material tends to minimize the total surface area to reduce this surface free energy. For instance, this case is observed in the liquids that the liquid droplets become spherical to have a minimum surface area. For solids which are mechanically

rigid materials reducing the surface area cannot be a possible situation. However; solid surfaces can reconstruct to bond surface atoms with each other. Due to their higher energies, surfaces of solid materials are so reactive. Hence, impurities do not mostly hold to surfaces and to reconstruct the surface, energy is required. At this point, grains incline to grow in size of smaller grains to reduce the energy.

Another planar defect is grain boundaries which are separating two small grains or regions of different crystallographic orientations. If solid materials have grain boundaries, they are called as polycrystalline which means that crystal generate of many crystal orientations no single. Grain boundaries have insensible cracks. There are different degrees between grain boundaries. If mismatch of the orientation is small, this boundary called as a small or low angle grain boundary (Figure 20). When low angle grain boundary is parallel with the edge dislocation, this specific type of grain boundary is called a tilt boundary. Tilt boundary is the result of a low angle grain boundary, because in general, the angle of misorientation is less than 10°. As discussed above for external surface explanation, surface energy is so high and the degree of misorientation is related to this energy. For high angle grain boundaries, this energy is being higher. This condition results in that grain boundaries are higher mobility, diffusivity and chemical reactivity than the grains. Both of low and high angle grain boundaries can be seen in Figure 20.

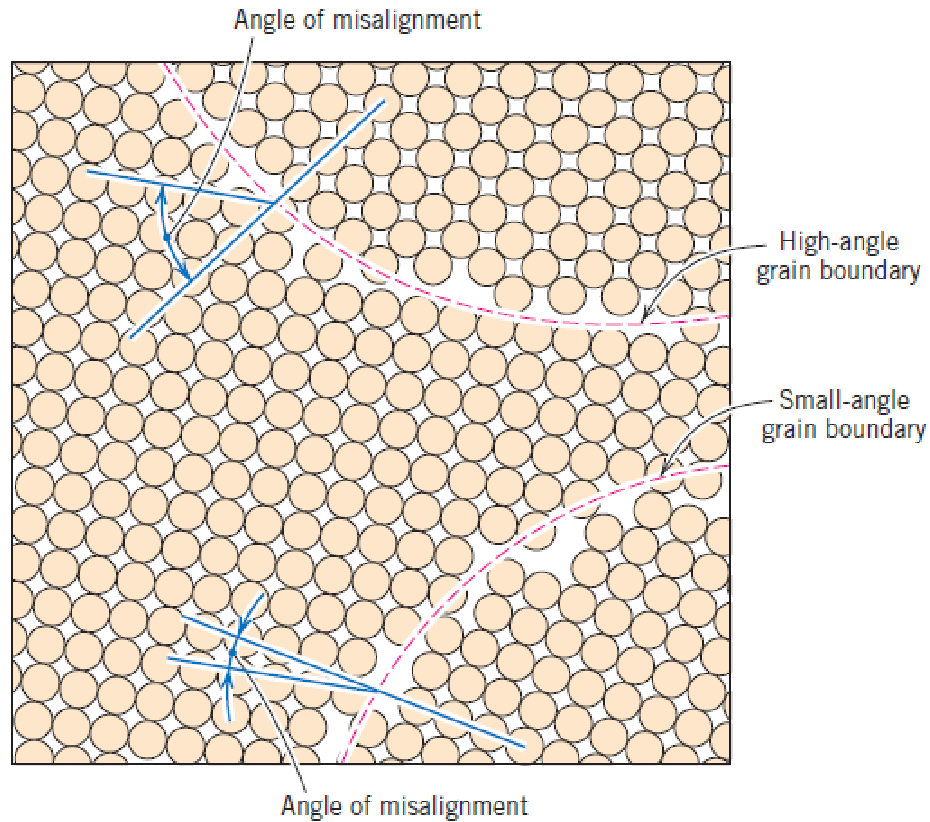

Figure 20.Schematic of a low and high angle grain boundary and the angle of misalignment [42].

Under an applied shear, a single crystal structure has a new orientation. This process is called a deformation twinning or twin boundaries. An original single crystal orientation and a new orientation are being a mirror image between each other (Figure 21). Plastic deformation also originates from twin boundaries and it is very important for epitaxial grown materials. At high annealing temperatures, twin boundaries can recover to original crystal orientation.

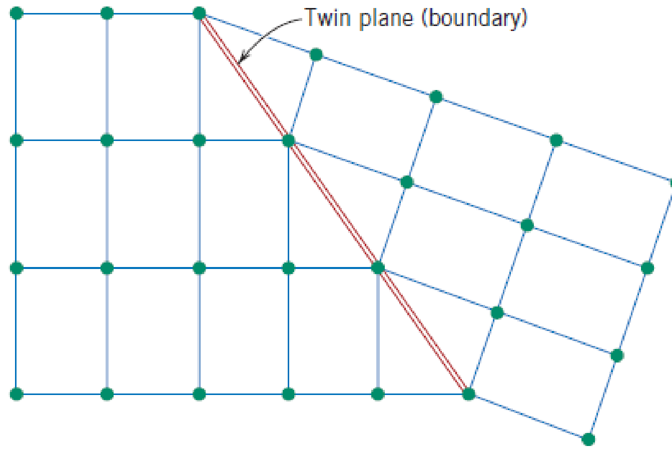

Figure 21. Schematic of a twin boundary and a mirror image [42].

Stacking faults can be observed usually in close-packed structures. In the order of …ABCABC… creates the FCC crystal structure. When this crystal pattern is destroyed, a stacking fault occurs. There are two kinds of stacking fault. First one is extrinsic stacking fault. This sort of stacking fault occurs when in the order of regular …ABCABC… crystal planes are broken with extra plane of atoms. Regular …ABCABC… crystal plane order changes to …ABC│B│ABC… crystal order (Figure 22.a). An intrinsic stacking fault is formed by removing a plane of atoms. Now, crystal sequence becomes …ABC║BCABC… order. This ║ symbol remarks the missing crystal plane (Figure 22.b).

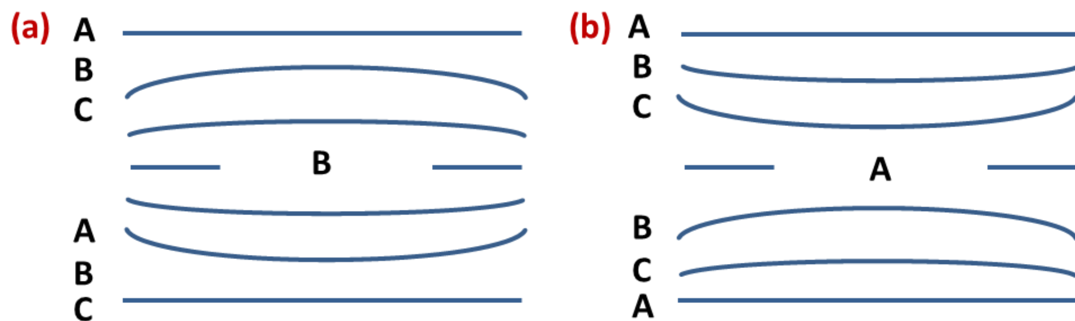

Figure 22. Stacking faults in the FCC crystal structure. (a) Extrinsic stacking fault with an extra B plane and (b) intrinsic stacking fault with a missing A plane.

A meaning of phase is explicit of physically, a homogeneous and definable of mechanically portion of the sample with a given structure and chemical composition.

Phase boundary is also known as internal defects. If the material has in ordered compounds, phase boundary occurs.

3.4. Three Dimensional Defects

Three dimensional defects in crystals are also called as volume defects. There are in general four kinds of three dimensional defects: precipitates, dispersants, inclusions and voids [55]. This classification is made according to the size of particles and their effect on the material.

Precipitates are small volume defects which are usually microns in size. When non-stoichiometric CdTe material is rapidly cooled from high temperatures, for example from annealing temperatures in Te-rich conditions for B face of CdTe, Te precipitates are formed on the surface of material. The sizes of Te precipitates in CdTe are range from 60 Å to 100 μm [56]. There are three main defects for B face of CdTe: Cd vacancies, Te interstitials and Te precipitates. These defects affect the physical and electrical behavior of the crystal [57].

Dispersants are larger than precipitates. Large precipitates, grains and polygranular formations may be called as dispersants. Dispersants also affect the physical and electrical properties of the material.

Large precipitates or impurity particles gather together to form small areas of a different phase. These small areas are called inclusions. Inclusions are generally 1-2 μm in size, sometimes that can be as large as 10-20 μm in CdTe [27]. Inclusions adversely effect on the strength and device characteristics of material.

Voids are areas the absence of a large number of atoms from the crystal structure. Voids are undesired formations that they weaken the mechanical properties of materials.

3.5. Lattice Mismatch

Lattice constant differences between a substrate and an epitaxial layer cause a lattice mismatch. This lattice mismatch will lead to strained or relaxed thin film on substrate. The lattice mismatch can be given as [58];

$$f_i = \frac{a_l - a_s}{a_s} \tag{3. 26}$$

where a_l is the lattice constant of an epitaxial film and a_s is the lattice constant of the substrate material. For CdTe grow buffer layer on a GaAs substrate with lattice constants are 6.48 Å [59] and 5.65 Å [60] respectively, so $f_i \approx 14.69\%$.

To minimize the defect density and increase the electron mobility of thin films, nearly matched substrate and epitaxial layers are needed. If lattice mismatch becomes larger, growing material begins to strain at the interface. When strain formation is not possible, relaxation occurs at the interface. Figure 23 shows the matched, strained and relaxed layers with respect to a substrate. Strain is divided into compressive strain which has a positive lattice mismatch and tensile strain which has a negative lattice mismatch.

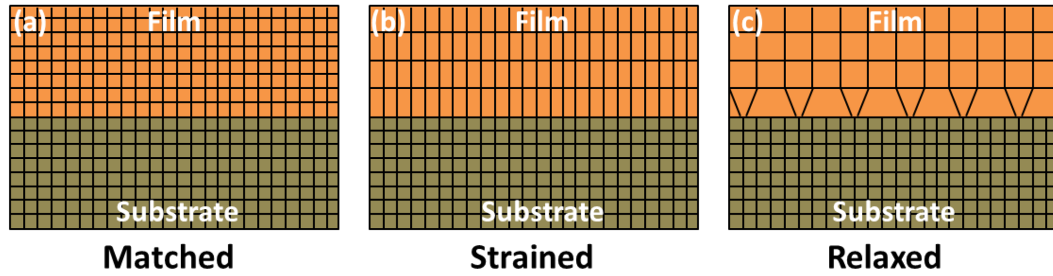

Figure 23. Schematic of (a) matched, (b) strained and (c) relaxed film on the substrate.

As mentioned above calculation of strain, stress and energy section, strain of the material induce also stresses. Therefore, elastic strain energy ingenerates in the epitaxial layers. The film thickness increases at the growth process, stored strain energy also increases. When the epitaxial layer thickness reaches the critical thickness, this stored energy is large enough to form dislocations at the interface. This dislocation is called misfit dislocations.

3.5.1. Misfit Dislocation

Misfit dislocations result in lattice mismatch between substrate and epitaxial layer when the critical thickness is exceeded. The value of critical thickness is related with the value of the lattice mismatch [61]. The critical thickness can be in size of a few

microns, if lattice mismatch is small. However; for lattice mismatch is bigger than ~ 10%, the critical thickness can be less than a monolayer. For specific example, if the lattice mismatch is as large as ~ 2%, the critical thicknesses are less than 20 Å [62]. Hence, buffer layer of CdTe/GaAs creates absolutely misfit dislocations.

Misfit dislocation occurs at the interface, but dislocations can complete at the free surfaces of an epitaxial films. These composed dislocations at the free surfaces are threading dislocations. Misfit dislocation curves up and glide from the interface to the threading dislocation (Figure 24). This condition lasts from the surface to the interface and also interface to the surface which is called dislocation loop or half loop. Therefore, half loop can nucleate at the surface and grow down to the threading component and fall down to the misfit component.

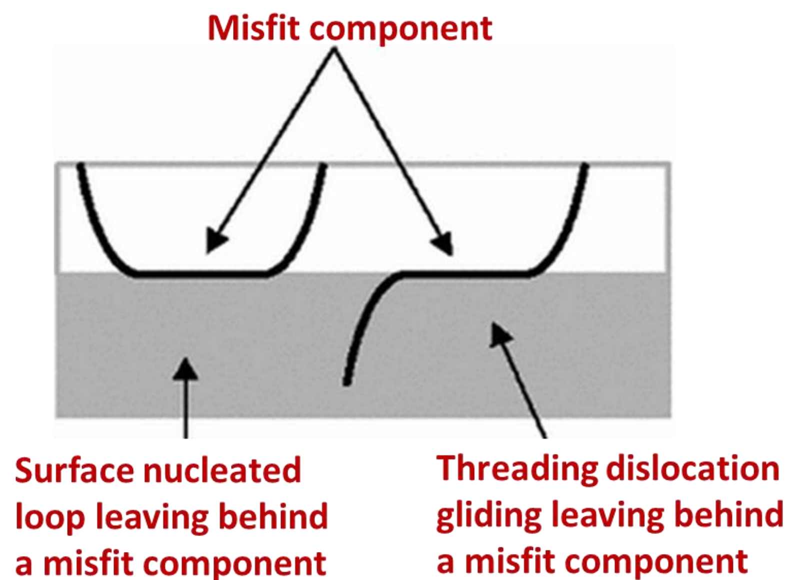

Figure 24. The schematic of misfit dislocation formation mechanisms in epitaxial films [61].

The lattice mismatch between CdTe and GaAs is $f_i \approx 14\%$. This value is positive, so there is a compressive stress. CdTe buffer layer grows the equilibrium lattice constant which is also it is own lattice parameter, 6.48 Å. However; GaAs lattice constant (5.65 Å) is smaller than CdTe lattice constant. GaAs lattice parameter increases to CdTe lattice parameter. At this point, CdTe buffer layer is constrained by the GaAs substrate, so compressive stress is occurred at the interface of the film.

3.5.2. Dislocation Interaction

Under an applied force, dislocation can become mobile and interact with each other. At this point, nonlocal force due to an external strain field should be examined to understand interaction between dislocations. By using Peach-Koehler formula, the work (W) done by the external stress field is [63];

$$\boldsymbol{W} = (\boldsymbol{Force}) \times (\boldsymbol{Distance}) = (\boldsymbol{\sigma l x}) \times \boldsymbol{b} \tag{3. 27}$$

where σ is applied shear stress, l the length of dislocation, x distance that the dislocation moved and b is the magnitude of Burgers vector.

Force acting on a unit length is;

$$\boldsymbol{f} = \boldsymbol{\sigma b}. \tag{3. 28}$$

$A_j = \sum_{i=1}^{3} \sigma_{ij} b_i$, where A_j is a vector. Finally, the force on a dislocation is;

$$\boldsymbol{f} = \boldsymbol{A} \times \boldsymbol{t} \tag{3. 29}$$

$\boldsymbol{t}$ is line vector of a dislocation. Due to this cross product, the force is always acting perpendicularly to the dislocation. This force is divided into three main subtitles. These are attractive, repulsive and negligible forces [63]. Firstly, for repulsion one, force is related to ~ b^2/x. Secondly, for attraction one, force is related to ~ $-b^2/x$. These two types of forces are depicted in Figure 25. Finally, for negligible one, no interaction between dislocations (x: distance between dislocations.). For the case of mobility of dislocations under an applied force, slip planes are important. As is known, slip occurs in FCC and zinc-blende lattice structures on the {111} plane in the <110> direction and with a Burger vector $\frac{a}{2}$[110] [41].

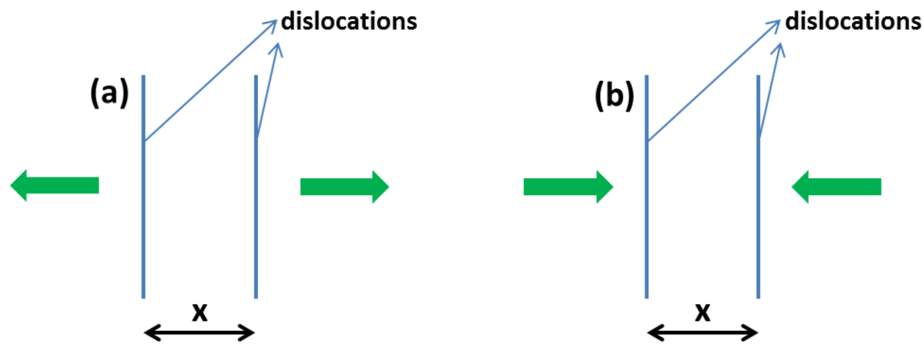

Figure 25. The schematic representation of (a) repulsive, (b) attractive forces.

The type of forces will be understood by the summing Burgers vectors of acting dislocations. According to conservation of Burgers vectors, Burgers vector can be added like a vector summation. For example, dislocation will interact with each other under an attraction force (Figure 25.b). In this case, dislocations are either neutralized with each other or combined as a single dislocation as seen in Figure 26. Burgers vector summation for neutralized situation is [41];

$$\frac{a}{2}[1-10]+\frac{a}{2}[-110]\rightarrow 0. \tag{3. 30}$$

Under the Frank's rule of dislocations [64], the condition

$$b_1{}^2 > b_2{}^2 + b_3{}^2 \tag{3. 31}$$

must be satisfied.

When two dislocations combined as a single dislocation for the zinc-blende or FCC crystal structure which is explained above,

$$\frac{a}{2}[10-1]\rightarrow\frac{a}{6}[2-11]+\frac{a}{6}[-11-2]. \tag{3. 32}$$

This relation also known as Schockley partials which are creates a stacking fault in the crystal [65].

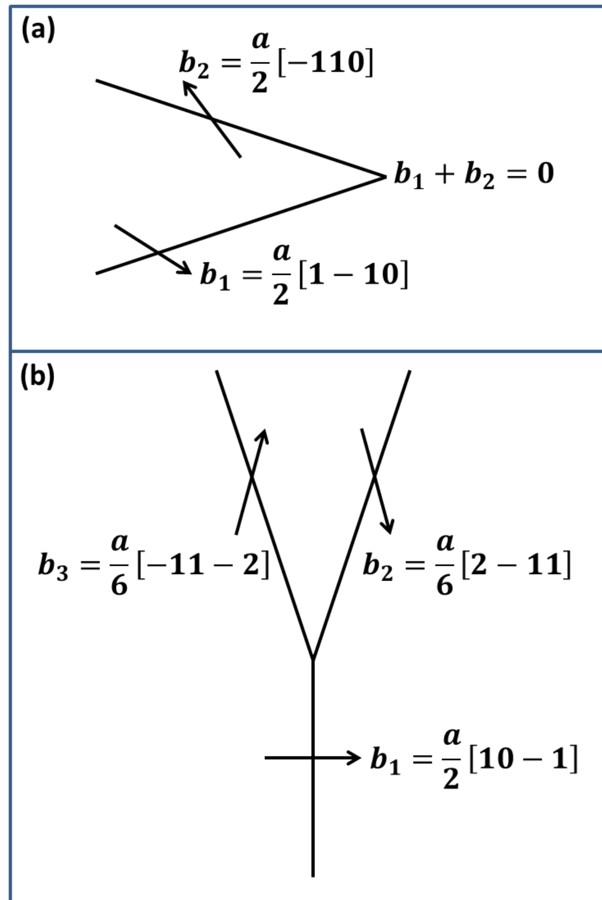

Figure 26. Graphically description of (a) neutralization and (b) combination of dislocations (adapted from [41]).

CHAPTER 4

OBSERVATION OF DISLOCATIONS

In order to minimize the damaging effects of the large lattice mismatch between the alternative substrate and the epilayer, buffer layer needs to be grown on alternative substrates. This lattice mismatch results in a large number of misfit dislocations. Most of these dislocations carried along with the growing film to the surface. Surface defects of the buffer layer reduce the material quality. Hence, the crystal quality and dislocation density of CdTe grown on alternative substrate needs to be analyzed in detail. Methods for observation of dislocations are defect decoration, transmission electron microscopy (TEM), SEM, AFM, Nomarski and electrical characterization (I-V, C-V, R_0A) techniques.

4.1. Defect Decoration Methods

Wet chemical defect decoration etching is the foremost method to reveal and observe various kinds of defects especially due to dislocation related ones over the epilayer surface. The procedure of wet chemical etching is divided into three main steps; oxidation, dissolution and dilution [66]. These steps determine the chemical reaction and hence etching rate of the etching solution. Bromic acid, bromine, chromic acid, nitric acid and hydrogen peroxide are used as an oxidizing agent [67]. Oxidizing agents take an electron from CdTe, so it is reduced. Surface of CdTe crystal can be found Te-rich or Cd-rich. Therefore, it is very important to find the chemical balance between the oxidation and dissolution steps on the polar surfaces of this compound semiconductor. For instance, tellurium has a higher reactivity as compared to cadmium, so the oxidizing agents are more reactive with tellurium atoms with respect to cadmium atoms. Oxide removal or dissolution step requires different chemicals such as hydrofluoric acid or hydrochloric acid [66]. After removing the oxide from the surface, dilution step starts. Water, lactic acid or acetic acid are used as diluting agents [66]. Different etch techniques leave different pit shapes on the surface. The defect

decoration etching creates etch pits at the end points of dislocations terminating at the surface due to the weakened bond strength. These etch pit shapes and etch rates are related with surface polarity and orientation of crystal. Therefore, crystal symmetry along the direction perpendicular to the surface can be monitored by the shape of etch pits. After the grown sample is etched with wet chemical etchants, EPD results and their effects are characterized with AFM, SEM, Nomarski microscopy and Raman Spectroscopy mapping. The density of etch pits are determined from the images obtained by these methods by manual counting or using some computer programs.

4.1.1. Everson Etch

Myers *et. al.* proposed a new chemical solution to etch CdTe samples [68]. This solution was included lactic acid ($C_2H_4OHCOOH$), nitric acid (HNO_3) and hydrofluoric acid (HF) with 1:1:1 volume ratios. Myers *et. al.* observed that Cd face of CdTe was black coating and Te face of CdTe was pitted by using $1HF:1HNO_3:1C_2H_4OHCOOH$. After Myers, The Everson etch was developed by W. J. Everson *et. al.* [69]. Everson etch is used as a standard etch technique for CdTe samples. Everson etchant solution which includes $C_2H_4OHCOOH$, HNO_3 and HF with 25:4:1 volume ratios, respectively to reveal dislocations on CdTe in both (111)B and (211)B orientations (Figure 27). The only disadvantage of this method is that the background of the sample is left very rough because of nanoridges which were formed due to (211) crystal orientation step-terrace structure [70, 71]. After the Everson etch, triangle-like shaped pits can be observed on surface of the sample by using some microscopy methods.

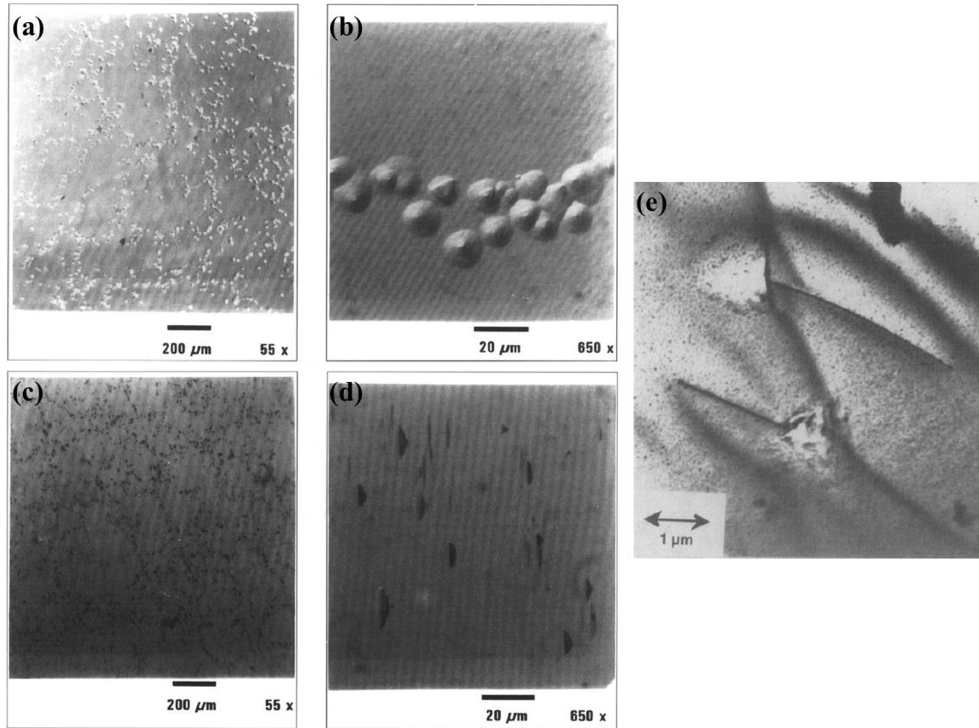

Figure 27. Nomarski microscopy images of (a) and (b) Everson etch pits on (111)B surface, (c) and (d) Everson etch pits on (211)B surface. TEM image of (e) Everson etch pits formed on dislocations [69].

4.1.2. Nakagawa Etch

This preferential etching was first developed by Warekois *et. al.* in 1962 [72]. E. P. Warekois *et. al.* claimed that B face of CdTe can be etched by using 3HF: $2H_2O_2$: $1H_2O$ and their results can be seen in Figure 28.

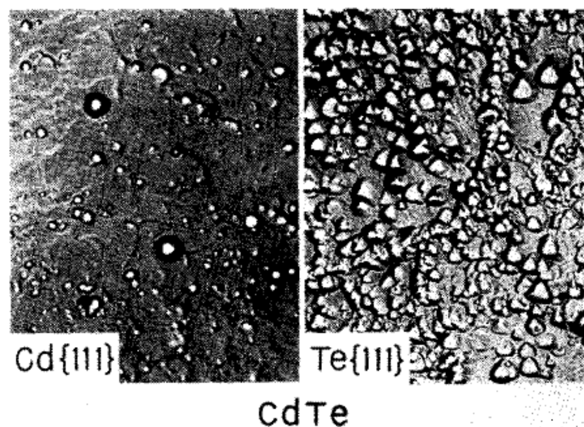

Figure 28. The CdTe (111) surfaces after 3HF: $2H_2O_2$: $1H_2O$ etch. Triangular etch pits are formed on Te-rich surface. Cadmium-rich surface is nearly polished [72].

Nakagawa etch was improved by Nakagawa *et. al.* [73]. It has been also indicated that 3HF: $2H_2O_2$: $2H_2O$ solution to reveal dislocations on CdTe (111)B but not on CdTe (111)A (Figure 29). After this paper published an etchant solution which consists of hydrofluoric acid, hydrogen peroxide and deionized water with 3:2:2 volume ratios is called as a Nakagawa solution.

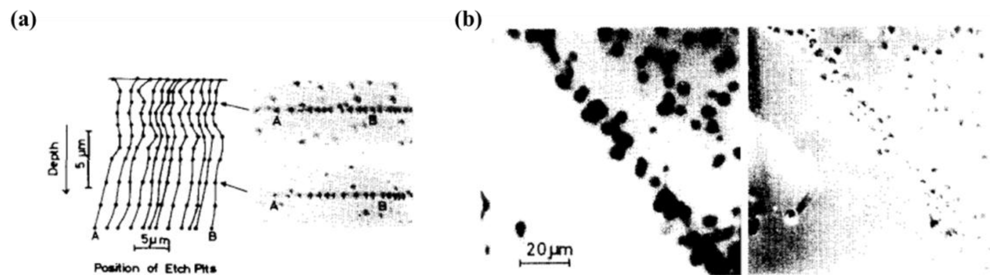

Figure 29. Optical microscopy images of (a) etch pits and how their positions into the sample and (b) surface after etching [73].

Nakagawa and Warekois etches were also studied by Fewster *et. al.* [74] and found an inconsistency Nakagawa etchant and CdTe surface polarity. Nakagawa and Warekois showed that their etchants were effective at B-face of CdTe, but Fewster claimed that these etchants actually were effective at A-face of CdTe and correlated this result with XRD studies [75]. Another study also reported the Nakagawa solution with different chemical variations (4HF: $0.5H_2O_2$: $2H_2O$) to work on B face of CdTe (Figure 30) [76]. But, the results of this study were not confirmed by other groups.

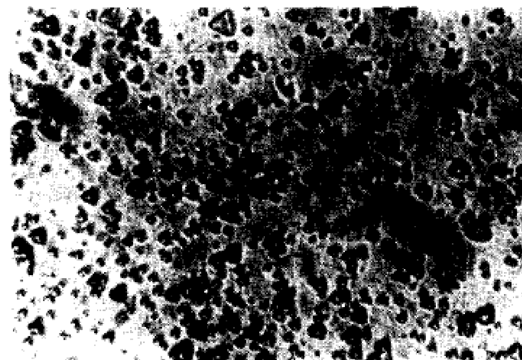

Figure 30. Optical microscopy image of etch pits on CdTe (111)B surface [76].

4.1.3. Benson Etch

Benson etch was developed by Benson *et. al*. [77] against the rough surface which is formed during the Everson etch. Benson etch was developed for both CdTe and HgCdTe for EPD studies. This etch method involves H_2O, HCl, HF, HNO_3 and CrO_3 with 300 ml, 10 ml, 10 ml, 10 ml and 8 gr volume ratios, respectively. However, the reaction in the Benson etch proceeds very fast on CdTe [9] etching. In addition, the film while creating etch pits yields less defined pits and, hence it is more appropriate for thicker (~ 10 μm) films. The Benson etch results of a study is shown in Figure 31.

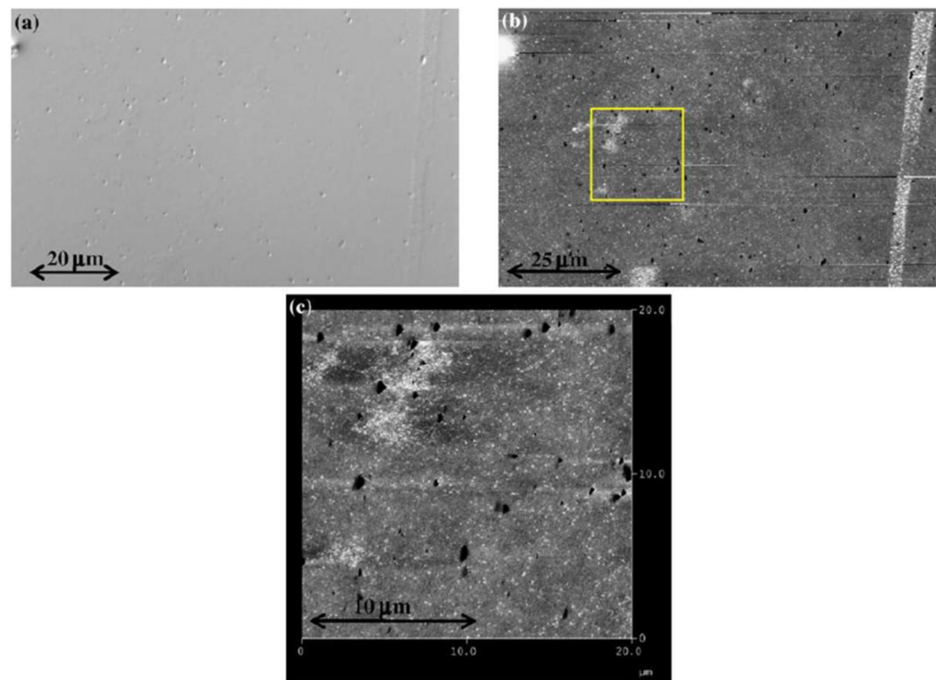

Figure 31. (a) Nomarski microscopy, (b) low-resolution AFM and (c) high-resolution AFM images of a sample surface after Benson etching [77].

4.1.4. Schaake Etch

The Schaake etch was developed by H. F. Schaake in 1970 [78], but this etch technique was not officially published. The Schaake etch which involves 150 ml H_2O, 25 ml HCl and 30 gr CrO_3 is the most prevalent method for HgCdTe materials. This solution is also effective in both A and B faces of HgCdTe. This etch creates round or elliptically shaped etch pits on the sample surface as shown in Figure 32.

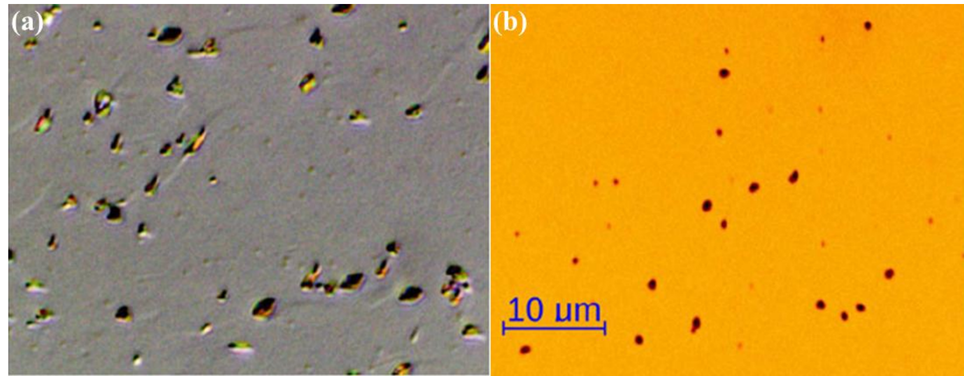

Figure 32. (a) and (b) Nomarski microscopy images of after 15 s Schaake etch HgCdTe samples [79].

4.2. Transmission Election Microscopy

Dislocations can be directly observed by using transmission electron microscopy (TEM), which was firstly built by Max Knoll and Ernst Ruska in 1931 [80]. Lattice deformity around the dislocations can display diffraction contrast as the electron beam undergoes Bragg scattering [81]. According to this diffraction contrast, unscattered electron beam appears as dark fields. Therefore, dislocations which are the cause of Bragg scattering can also appear as a dark lines in TEM images. If the orientation of the sample is known, position of the defects, types of the defects and Burger vectors can be easily examined by TEM.

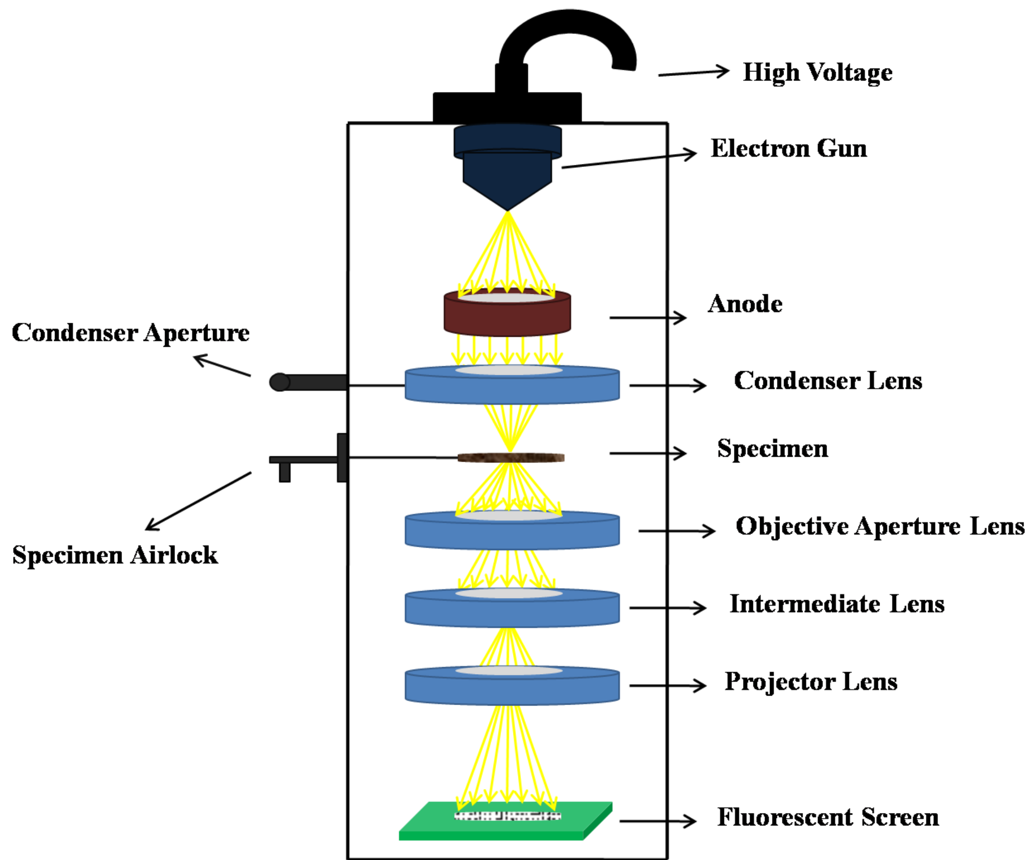

Figure 33. Schematic description of TEM components.

TEM has typically three main parts common to all electron microscopes. First one is electron gun which produces the electron beam under the high voltage and condenser system which contains condenser lens and condenser aperture. This system focuses the beam onto the sample. Second part of TEM, the image producing system, consisting of the specimen airlock, specimen stage, objective aperture lens, intermediate and projector lenses which focus the electrons getting through the sample to create an image. Final step is the image viewing process. This part consists of a fluorescent screen for gathering the unscattered electrons to form “shadow image” of the sample with the diffraction contrast. These three main parts which are described above are shown in Figure 33.

4.3. Electrical Characterization of Etch Pit Density

For the LWIR detector applications, HgCdTe is one of the most important materials. CdTe/GaAs buffer layers are suitable for large format focal plane arrays. However; lattice mismatch between CdTe and GaAs leads to a large number of misfit dislocations. As known, misfit dislocations originate at the interface and cause the threading dislocations which are carried along with the growing film to the surface. Surface defects of the buffer layer reduce the detector performance. One of the most important parameter for LWIR detector fabrications is zero-bias junction impedance (R_0A) which is a measurement method of the thermal noise of the LWIR detectors. Higher R_0A values are result in the lower thermal noise. As a consequence, to maximize detector performance and R_0A, etch pit density which are related with dislocations should be minimized. Dislocations can adversely affect the electrical properties of detectors because of their electric field [82].

Johnson *et al.* demonstrate the relations between EPD and R_0A (Figure 34) [83]. R_0A values decreases with the square of EPD values at high etch pit densities.

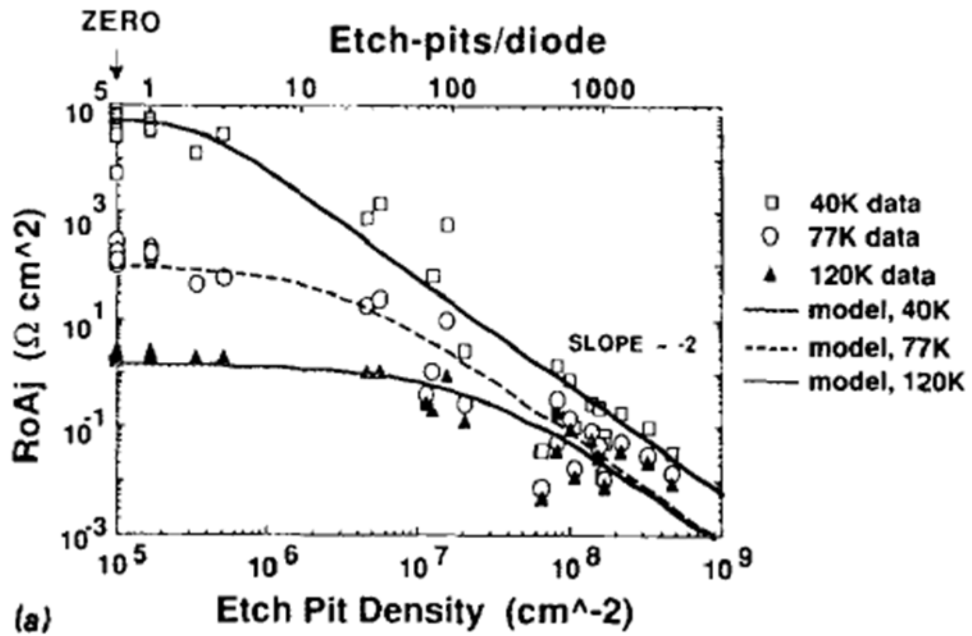

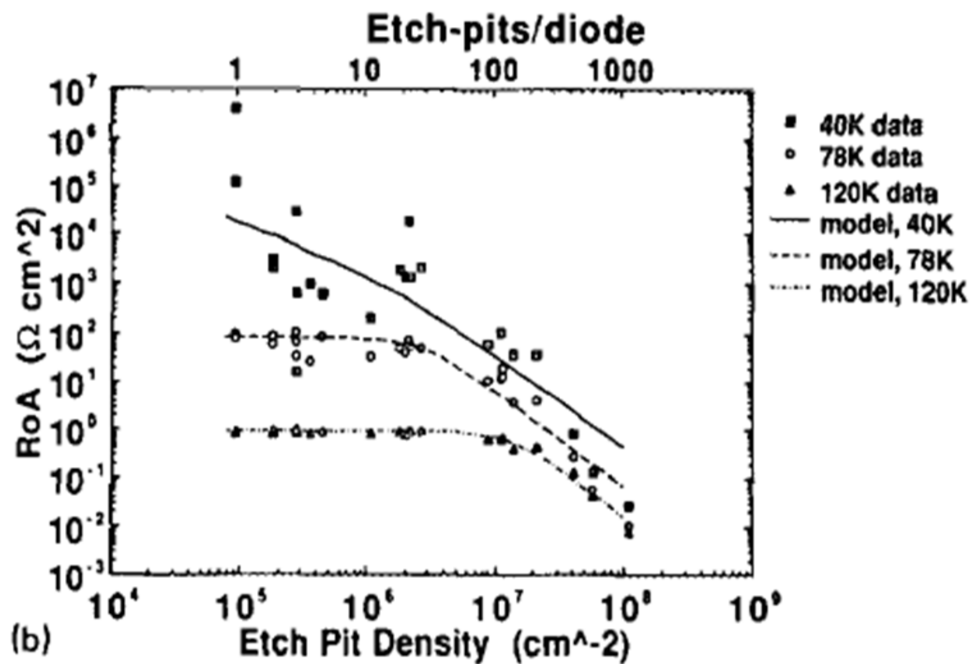

Figure 34. R_0A versus EPD values for a device built on an (a) Array 1 and (b) Array 2 (Array 1 junction area: $6.8x10^{-6}$ cm^2 and Array 2 junction area: 1.1 $x10^{-5}$ cm^2) [83].

CHAPTER 5

EXPERIMENTAL TECHNIQUES AND PROCEDURES

5.1. Atomic Force Microscopy

Atomic force microscope (AFM) was invented by Gerd Binnig, Calvin F. Quate and Christopher Herber in 1986 [84]. AFM relies on interactive force to generate an image. Interactive force occurs between a tip and sample surface using the probe which is a micro fabricated elastic cantilever with a sharp tip on the end.

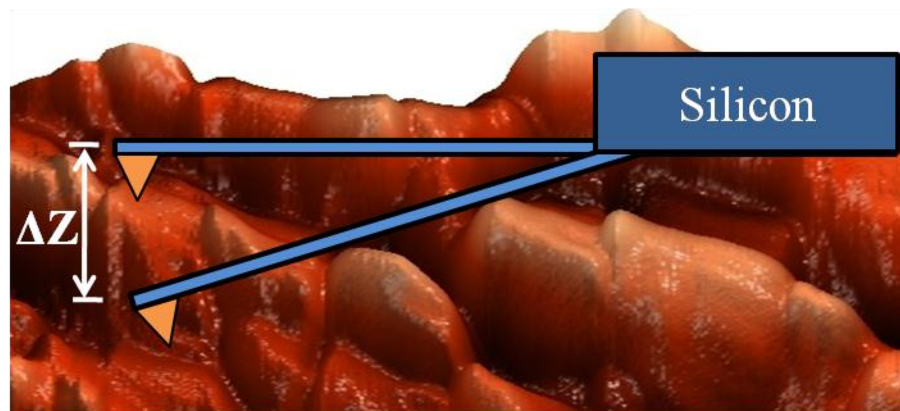

Figure 35. Schematic description of tip bending (adapted from [85]).

Cantilevers are generally made from silicon (Si) or silicon nitride (Si_3N_4) materials [86]. The deflection of the AFM cantilever can be obtained by using Hooke's Law [87];

$$\boldsymbol{F = k\Delta Z} \qquad (5.\ 1)$$

where ΔZ is the deflection of cantilever (Figure 35) which is determined by dividing the acting force F with spring constant k.

The optical detection system of the AFM detects the displacement of the cantilever. This system consists of a four-quadrant photodiode and a laser source. In simple terms, laser beam is focused on the back of the cantilever. The reflected beam is collected in a photodiode. Each section of the photodiode creates photocurrents when

laser falls on them. Through this optical detection system, the attractive or repulsive forces due to the tip bending or cantilever torsion due to the lateral component of tip-sample interaction can be examined. Whether the reference values in the photodiode sections are indicated as I_{01}, I_{02}, I_{03}, I_{04} and I_1, I_2, I_3, I_4 are the current values, the variation of currents from different sections of the photodiode $\Delta I_i = I_i - I_{0i}$ can be characterized with $\Delta I_Z = [(I_1 + I_2) - (I_3 + I_4)]$ and $\Delta I_L = [(I_1 + I_4) - (I_2 + I_3)]$ for deflection and torsion of the cantilever.

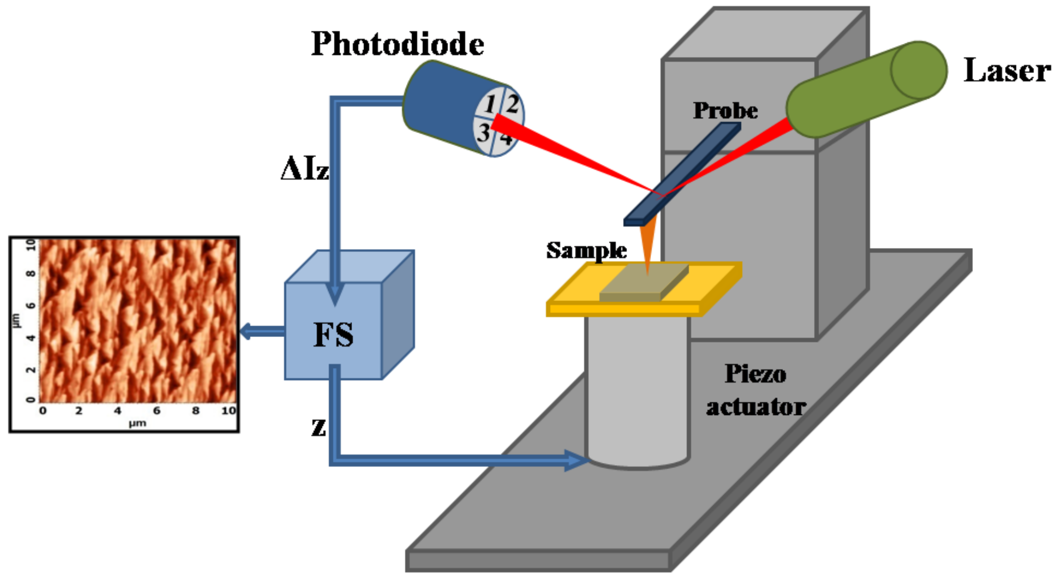

Figure 36. Schematic representation of AFM components.

In feedback mode, the ΔI_Z value is used as an input signal and output signal adjusts the Z position of the scanner. The main purpose of the feedback system is to keep the tip-sample interval (ΔZ) constant. If ΔZ = constant mode is used, tip moves along the sample surface. Accordingly, $Z = f(x,y)$ surface topography can be acquired with respect to applied voltage on the Z-electrode of the scanner (Figure 36).

The interactive forces taking part in AFM imaging which are mentioned before can be explained by considering van der Waals forces [88]. Two atoms are located at a distance r from each other, the van der Waals potential energy of these two atoms is approximated by the exponential function which is known as Lennard-Jones potential [31].

$$U(r) = U_0\left\{-2\left(\frac{r_0}{r}\right)^6 + \left(\frac{r_0}{r}\right)^{12}\right\} \qquad (5.2)$$

where the first term describes the attraction of long distances due to dipole-dipole interaction and second term describes short range repulsion which are explained by the Pauli exclusion principle. The r_0 parameter is the equilibrium distance between two atoms and it corresponds to the minimum energy value (Figure 37).

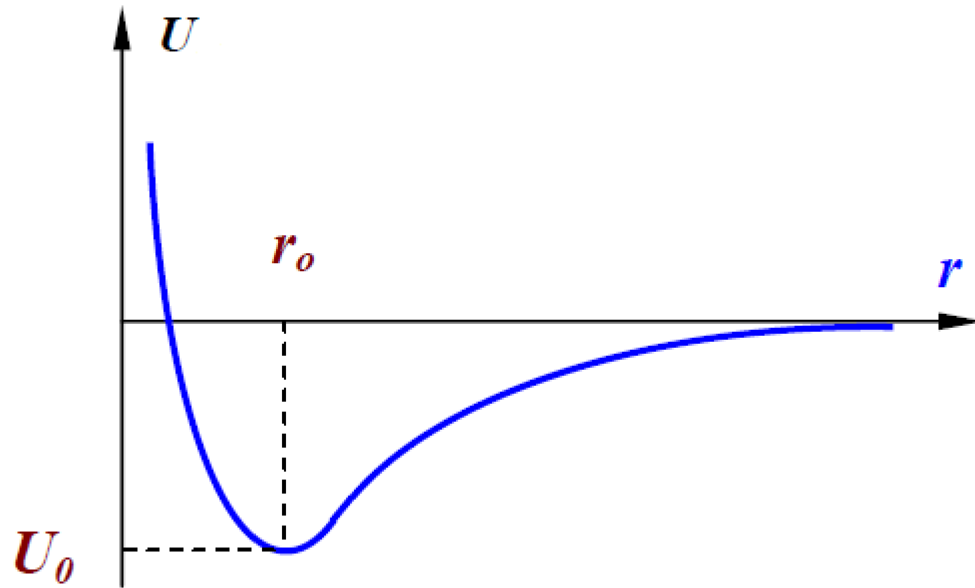

Figure 37. Lennard-Jones potential [86].

Distance between the tip and the sample is dependent van der Waals force which can be seen in Figure 38.

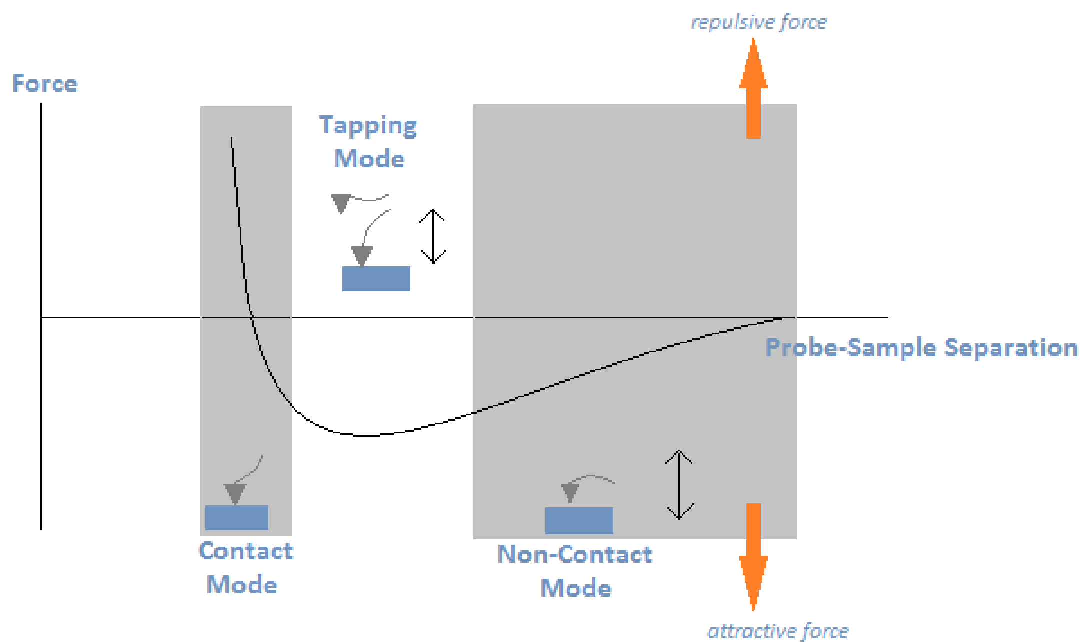

Figure 38. Force as a function of probe-sample separation [89].

The main AFM imaging modes are divided into three parts: contact mode, tapping (semi-contact) mode and non-contact mode (Figure 38). In our AFM measurements, in general tapping mode is used for surface characterization.

5.2. Scanning Electron Microscopy

Scanning electron microscopy (SEM) was invented by Max Knoll in 1935 as a tool for surface characterization [80]. SEM is a type of electron microscopy that creates images of a sample by using focused beam of electrons and gain information about surface structure and composition. The outcomes of interaction between electron beams and a sample can be seen in Figure 39.

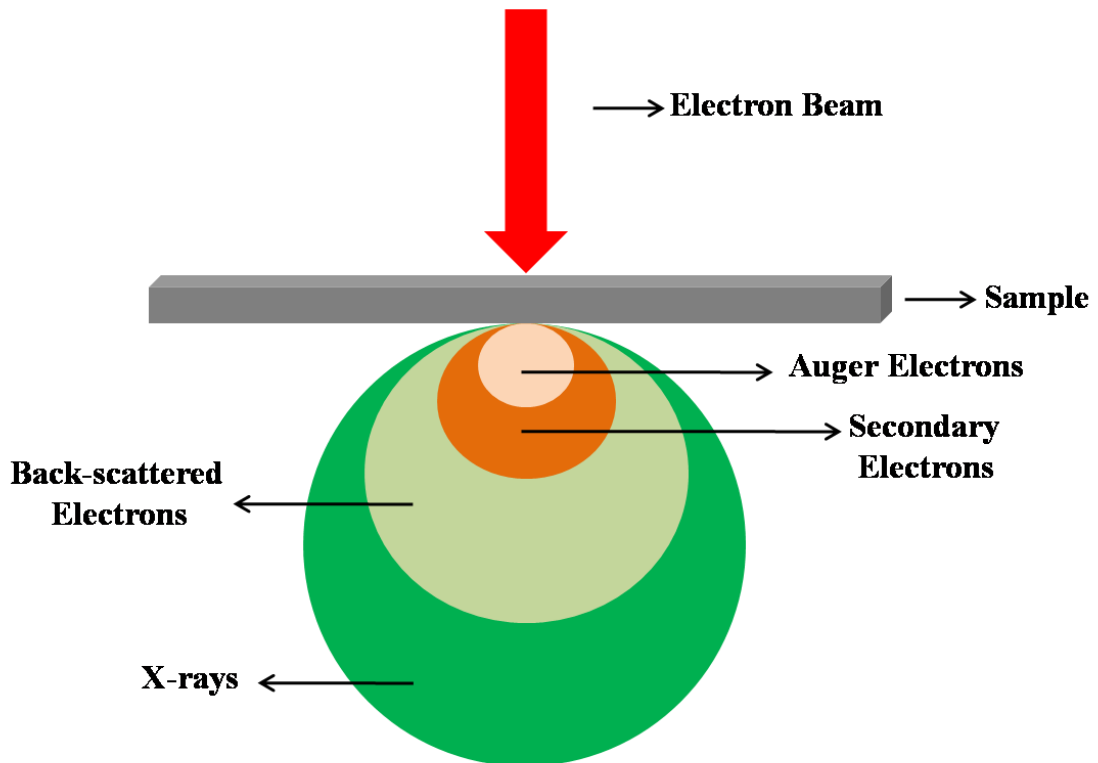

Figure 39. Demonstration of output of interaction of electrons with sample.

The types of signals at various detector produced by an interaction between sample and focused electron beam involve auger electrons, secondary electrons, back-scattered electrons and characteristic x-rays (Figure 39). Depth ranges of the interaction volumes are investigated with respect to various types of scattered electrons and x-rays.

Auger electrons have ~ 1 nm, secondary electrons have ~ 100 nm, back-scattered electrons have ~ 1-2 µm and X-rays have ~ 5 µm depth ranges [90-92].

SEM uses high vacuum conditions and also electrons to produce an image. All water must be removed from the sample since the water would vaporize and interfere with electron beam in the vacuum. Metal, semi-metal and semiconductor samples are conductive enough and, therefore, no preparation required before being used. However, all non-metals need to be made conductive by covering the sample with a thin layer of conductive material by using sputter coater.

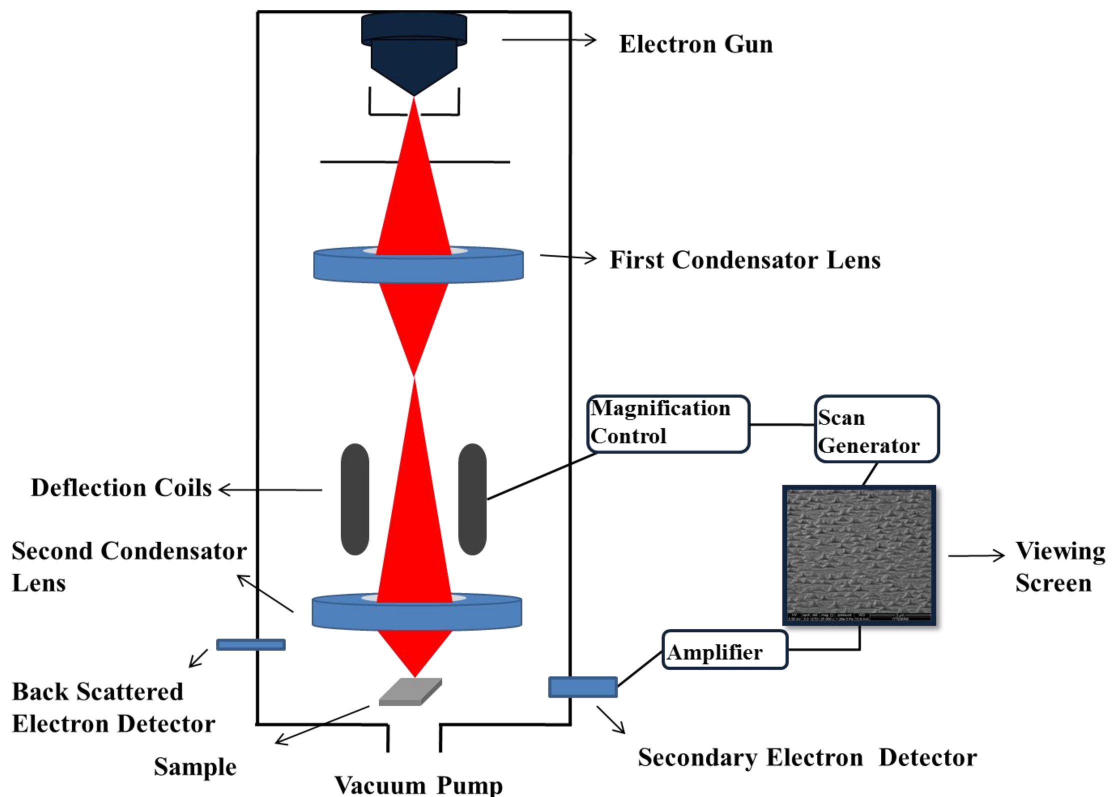

Figure 40. Schematic diagram of a scanning electron microscope.

SEM consists of an electron gun which produces a beam of electrons. The electron beam follows a vertical path from electron gun to the sample surface in a vacuum. This vertical path involves the deflection coils and lenses which focus the beam onto the sample. Electrons and x-rays are produced from the sample when the electron beam hits the sample. Backscattered and secondary electron detectors collect these ejected electrons and x-rays and convert them into a signal. This produces the final image (Figure 40).

For the topographic images, we use a secondary electron detector because; secondary electrons are closer to the sample surface. Backscattered electron detector gives information due to the atomic contrast. Elements of higher atomic number give a brighter image (dark-bright contrast). For the sample with unknown elements, x-ray detector (EDX) can be used. This detector collects the x-rays which are scattered from the sample surface. Each element has a different x-ray diffraction spectrum. The difference between XRD and EDX is that XRD for the crystal composition and uses the x-rays. However; EDX gives information for the elemental composition by using electrons.

5.3. Nomarski Microscopy

Differential Interference Contrast (DIC) is also known as Nomarski microscopy. It was invented by George Nomarski in 1960 [93]. DIC is a type of optical characterization technique which involves Wollaston (Nomarski) prisms for separating and merging a polarized light. Polarized light is formed when light from lamp source is passed through a polarizer.

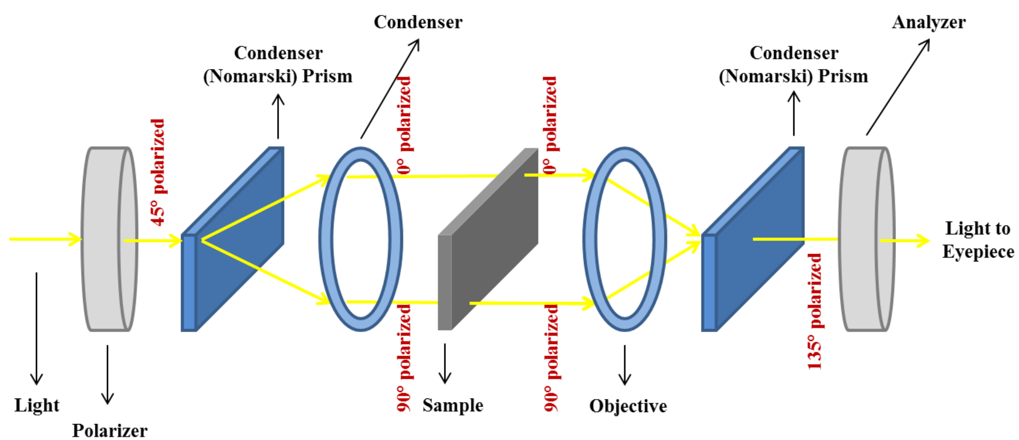

Figure 41. Schematic representative of DIC microscope working principle.

Working principle of the DIC microscope is based on the polarized light source which is firstly divided into two rays (ordinary and extra-ordinary) by first condenser (Wollaston or Nomarski) prism [94]. These two rays are vibrating perpendicular with each other. These two rays reach the condenser and aligned parallel to each other. Distance between these two parallel rays is almost equal to the optical path difference.

Perpendicular vibration between rays does not occur to cause interference. Later, two rays passed through the sample and wavelengths of these rays changes with respect to the sample properties such as thickness or refractive indices. Two parallel rays go into the objective and begin reunification. Second Wollaston or Nomarski prism merges two rays. Analyzer prevents the interference of the rays. The final image which can be seen with eyepieces has the three-dimensional appearance of the sample. This pseudo three-dimensional effect results from the shadow impact that involves the brighter and darker sides. Working principle of Nomarski microscope can be seen clearly in Figure 41.

5.4. Reflected High Energy Electron Diffraction

Reflected high energy electron diffraction (RHEED) is an *in-situ* characterization technique which gives information about surface during the growth. To understand RHEED geometry, some theoretical background of the electron diffraction and kinematic scattering will be given in this section. For high energetic electrons (E ≥ 50 keV), relativistic effect should be taken into account [95].

$$\boldsymbol{eV_0} = \sqrt{\left(\boldsymbol{m_0^2 c_0^2} + \boldsymbol{p^2 c_0^2}\right)} - \boldsymbol{m_0 c_0^2} \tag{5. 3}$$

Accelerating voltage, electron rest mass, electron momentum and speed of light are indicated with V_0, m_0, p and c_0, respectively. If we rewrite this above equation leaving the momentum alone;

$$\boldsymbol{p} = \sqrt{\boldsymbol{2m_0 eV_0}\left(\boldsymbol{1} + {\boldsymbol{eV_0}}/{\boldsymbol{2m_0 c_0^2}}\right)}. \tag{5. 4}$$

can obtained.

Due to the wave-particle duality, a beam of electrons are diffracted just like a beam of light or a matter wave. Louis de Broglie proposed moving particles can be associated with a wave [96]. Therefore, electrons wave-particle property can be explained by;

$$\boldsymbol{\lambda} = \frac{\boldsymbol{h}}{\boldsymbol{p}}. \tag{5. 5}$$

equation 5.4 can be substitute into the equation 5.5 to obtain,

$$\lambda = \frac{h}{\sqrt{2m_0eV_0\left(1+{eV_0}/{2m_0c_0^2}\right)}}. \quad (5.6)$$

c is speed of light and accepted value is 2.99×10^8 m/s. h is Planck's constant and is equal to 4.14×10^{-15} eV.s. Rest mass of electron is indicated with m_0 and it is equal to 0.51×10^6 eV/c^2. When these numeric values are substituted in the de Broglie relation, wavelength equation becomes;

$$\lambda = \frac{12.26}{\sqrt{V_0(1+0.9785x10^{-6}V_0)}}\ \text{Å}. \quad (5.7)$$

If the energy value of the incident beam is set to 30 keV, wavelength is equal to 0.07 Å according to the above equation. RHEED patterns, as seen on the phosphorescent screen, are the result of the constructive interference of the scattered wave. Constructive interference term is related to the Bragg condition which is given by [97];

$$n\lambda = 2d\sin\theta_i. \quad (5.8)$$

As can be seen in Figure 42; the incidence angle θ_i is equal to ${\theta}/{2}$ for elastic scattering process. Also in this figure, scattering or momentum transfer vector is given.

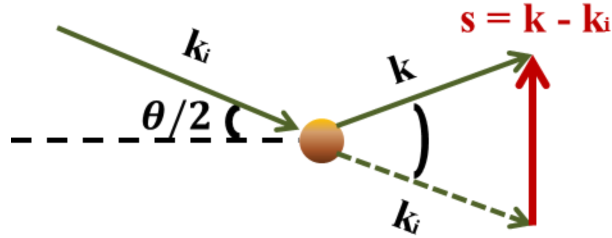

Figure 42. Representation of elastic scattering process [98].

Under the conditions of elastic scattering, incidence and scattered wave vectors are $|\mathbf{k}'| = |\mathbf{k}| = 2\pi/\lambda$ [99]. Diffraction maximum occurs when the Laue condition is satisfied and this condition is [98];

$$sd = 2n\pi. \quad (5.9)$$

Order of diffraction is demonstrate by n. RHEED patterns on the phosphorescent screen are due to diffraction of electrons from the surface atoms in reciprocal lattice

space. If the real space basis vectors are indicated as **a**, **b** and **c** where the relation between real and reciprocal space basis vectors is [31];

$$\boldsymbol{a} \cdot \boldsymbol{a}^{*} = \boldsymbol{b} \cdot \boldsymbol{b}^{*} = \boldsymbol{c} \cdot \boldsymbol{c}^{*} = \boldsymbol{2\pi} \ (\textbf{otherwise} = \boldsymbol{0}). \tag{5. 10}$$

Translation vector is also indicated for reciprocal space can be given as;

$$\boldsymbol{G_{hkl}} = \boldsymbol{h}\boldsymbol{a}^{*} + \boldsymbol{k}\boldsymbol{b}^{*} + \boldsymbol{l}\boldsymbol{c}^{*} \tag{5. 11}$$

h, k and l are Miller indices. Laue condition under the constructive interference for certain miller indices is **s** = **G** [98].

The incident electron beam hit the crystal surface which is growing epitaxially at low angle of incidence and is reflected onto the phosphorescent screen to form RHEED patterns (Figure 43). RHEED patterns include spots, streaks, rings and lines.

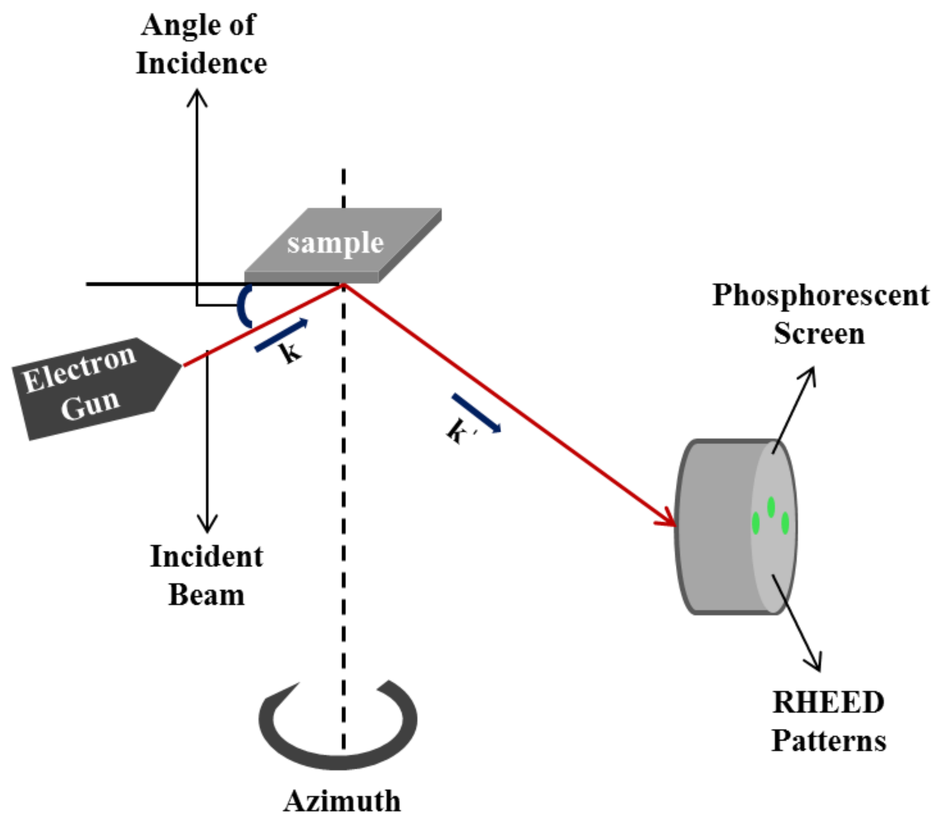

Figure 43. Schematically demonstration of experimental arrangements of RHEED.

The intensity oscillation changes of the RHEED spots on the screen give information about growth parameters such as removal of oxides from epi-ready substrates surface, surface roughness of the grown layers and crystal quality of the

layers [100]. When the incident beam of electrons reach the epi-ready surface at the start of the growth, incident electrons get through minimum diffraction because of surface smoothness. Therefore, RHEED patterns have maximum intensity. When a layer is partially covering the surface, electrons get through maximum diffraction and this condition led to minimum intensity of the RHEED patterns.

Calculation of the lattice constant for growing material from the RHEED images and the percentage of the error between the accepted and calculated value of the lattice parameters will be discussed in section 6.2.

5.5. Raman Mapping

Raman spectroscopy was discovered by C. V. Raman and K. S. Krishnan in 1928 [101]. In addition, C. V. Raman was awarded the Nobel Prize for discovery of Raman effect in 1930 [102]. Raman spectroscopy can be used for distribution of vibrational modes over an area of the lattice to generate variation in composition. The data signal collected by the detector and then sent to the processing system for analysis.

Laser beam comes from the laser source and passes through the filters. Beam splitter deflects a portion of light onto the optical microscope. Light is passed through a proper objective and laser light is focused onto the sample. Sample stands on the XYZ stage. Laser light is scattered from the sample and follows a proper optical path to reach a detector. Computer system is used to analyze signals which are collected by detector (Figure 44).

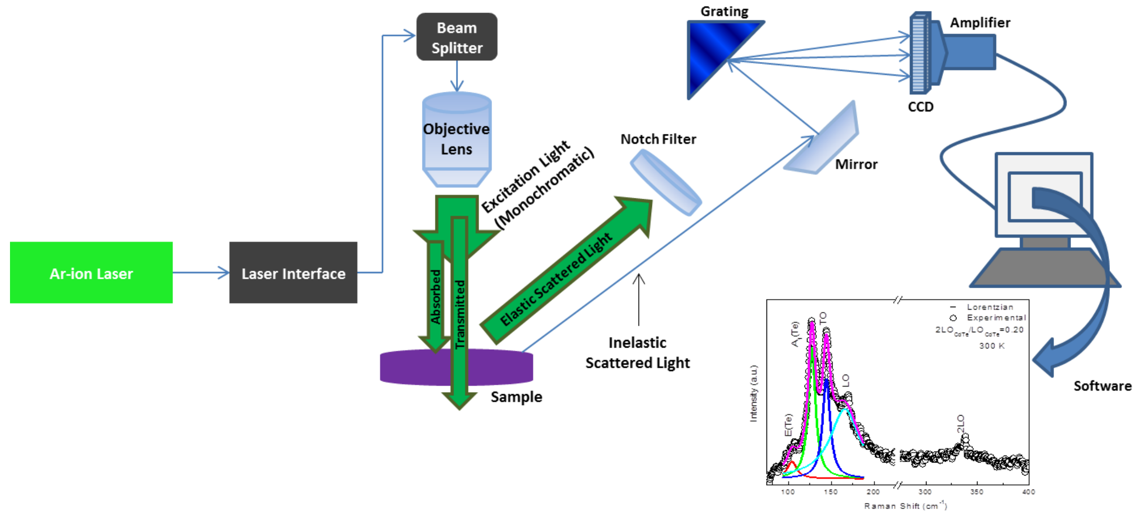

Figure 44. Schematic representation of a confocal Raman spectroscopy.

In order to investigate the effects of wet chemical etching procedures on especially Te, CdTe and GaAs vibration modes in this study, two dimensional (x, y) maps were recorded by Raman spectroscopy at room temperature. Raman measurements were performed by a confocal Raman system.

CHAPTER 6

EXPERIMENTAL RESULTS AND DISCUSSION

6.1. MBE Grown CdTe/GaAs (211)B Epilayers

CdTe buffer layers on epi-ready GaAs (211)B substrates were grown by Veeco GEN20MZ MBE system. The GaAs protective oxide was desorbed at approximately 650-580 °C under As_4 flux. After this step, substrate temperature was cooled to the range 280-218 °C to grow CdTe nucleation layer. Finally, the substrate temperature was heated to the growth temperature at range between 295-310 °C under Te_2 flux and the growth was carried at a rate of about 1μm/h. Temperature and duration of the deoxidation, nucleation layer and buffer layer growth parameters were studied.

Temperature values of the substrate and molecular beam epitaxially grown layers were measured by a non-contact thermocouple measurement system. Temperature values were also measured by a band edge thermometry (BandiT) and pyrometer systems. It is indicated that both BandiT and pyrometer measurement systems followed closely each other for temperature changes during the growth [103]. BandiT is also known as a detection system which detects emitted radiation from the substrate holder. Therefore, especially at high temperatures, BandiT measurement values were more accurate than thermocouple reading values [104].

VI/II flux ratio describes the rate between the total amount of Te which is group VI element and also the total amount of Cd which is group II element in periodic table. VI/II flux ratio is obtained by measuring beam equivalent pressures (BEP) of Te_2 and CdTe fluxes during the growth with respect to base pressure of MBE growth chamber. This ratio was also varied from sample to sample. Furthermore, *in-situ* annealing process was applied to some samples. Growth parameters are given in the Table 2.

Table 2. CdTe (211)B buffer layers growth parameters.

Sample No	VI/II	Deoxidation		Nucleation		Annealing		Growth	
		T (°C)	Time (min.)	T (°C)	Time (s.)	T (°C)	Time (min.)	T (°C)	Time (min.)
CT6	3	650	4	280	30	–	–	310	80
CT9	3	650	4	250	30	–	–	310	80
CT10	3	600	4	250	30	–	–	310	278
CT22	3	582	4	220	600	380	5	300	120
CT24	2	580	4	220	600	390	5	305	120
CT25	1,5	583	4	220	600	380	5	295	120
CT26	1	582	4	218	600	388	5	295	120
CT27	2,5	584	4	219	600	390	5	302	120

To measure the thickness of an epilayer, we performed the *ex-situ* spectroscopic ellipsometry (SE) and fourier transform infrared spectroscopy (FTIR) transmittance measurements.

A Woollam model M-2000X ellipsometer was used for epilayer thickness measurements. In order to obtain the thickness, the ellipsometric data were fitted using a three-layer model; GaAs substrate, CdTe film, and a surface-oxide layer. The Cauchy material CdTe-oxide was used as a surface layer. For the substrate, the dielectric function of the GaAs in the Woollam library was used.

The transmittance of CdTe films were measured at room temperature using a Bruker Vertex-80v spectrometer in the range of 4000 cm^{-1} to 15500 cm^{-1} which is equipped with a room temperature InGaAs detector and KBr windows. During measurements a green laser with a wavelength of 532 nm was used to obtain thickness values of CdTe epilayers. Thicknesses of CdTe layers were also obtained from intensity oscillations in the transmittance spectra.

$$t_{CdTe} = \frac{1}{2n(\Delta k)_{avg}} \quad (6.\ 1)$$

where t is the thickness of the CdTe buffer layer, n is the refraction index of CdTe and Δk is the distance wave number differences between two intensity oscillations.

Both GaAs and CdTe is transparent at lower energies than their respective bandgap, therefore transmittance of CdTe on GaAs can be obtained with reduced transmittance. On the other hand, since bandgap of GaAs at lower energy than that of CdTe, the bandgap cut-off of only GaAs can be observed.

To investigate the crystal quality of epitaxially grown CdTe (211)B samples, XRD rocking curve measurements were obtained by using Philips X'Pert PRO MRD XRD system. The X-ray radiation was emitted by copper x-ray source and characteristic wavelength of this radiation (K_α) was 1.5418 Å.

In Table 3, characterization results of XRD, SE and FTIR are given for MBE grown CdTe on GaAs (211)B buffer layers. Compared to Table 2 and Table 3, growth rate changes a lot with the growth conditions such as flux ratio or nucleation layer growth temperature.

Table 3. XRD, SE and FTIR characterization results for CdTe films.

Sample No	**XRD-FWHM (arc-sec)**	**Thickness (µm)**	
		SE	**FTIR**
CT6	–	1.92	2.06
CT9	280	1.63	1.73
CT10	116	5.05	4.91
CT22	196	2.29	2.60
CT24	327	2.15	2.27
CT25	172	2.21	2.30
CT26	206	2.02	1.99
CT27	299	2.08	–

FTIR transmittance measurements are comparable with SE measurements as given in Table 3.

6.2. RHEED Characterization Results

As an *in-situ* characterization technique, RHEED was used a 24-keV beam. RHEED is very useful method to understand epitaxial changes and the surface crystallinity during the growth. (211) zinc-blende buffer layer surface is formed two low-index crystal planes which are [-111] and [01-1]. RHEED pattern images which were viewed along [01-1] were used in this section.

CT22 buffer layer was grown on 20x20 mm^2 epi-ready GaAs (211)B substrates which were cut from 4" wafers. Base pressure of the MBE system was $6x10^{-10}$ Torr before the growth. During the growth process, the sample was rotated 2 revolutions-per-minute (rpm). The GaAs native oxide was desorbed at 582 °C for 4 minutes under 2.45 x 10^{-6} Torr As_4 flux. During the oxide removal process, the surface structure changes of GaAs wafer was monitored by RHEED. As shown in Figure 45.a, [01-1] RHEED patterns became streaky patterns after the oxide desorption. After deoxidation, nucleation layer growth and annealing steps, the substrate temperature was heated to the growth temperature of 300 °C under 5.84 x 10^{-7} Torr Te_2 and 6.7 x 10^{-7} Torr CdTe fluxes for 120 minutes. [01-1] RHEED patterns on fluorescent screen in Figure 45.b are shown CT22 sample surface at the end of the growth process. Compared to the Figure 45.a and Figure 45.b, streaky RHEED patterns in Figure 45.a became shorter, expanding and closer to each other in Figure 45.b.

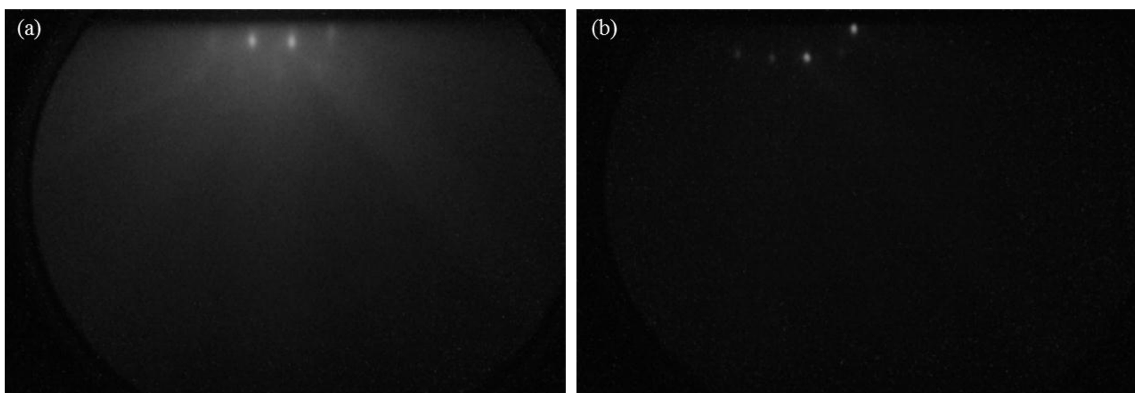

Figure 45. [01-1] RHEED patterns of CT22 (a) after oxide desorption at 582 °C and (b) after growth at 300 °C.

20x20 mm^2 epi-ready GaAs (211)B substrates were used to grow CT24 buffer layer. Before the growth, base pressure of the MBE system was 3.72 x 10^{-10} Torr. In

Figure 46.a, streaky RHEED patterns were obtained for GaAs oxide desorption at 580 °C for 4 minutes under 2.34 x 10^{-6} Torr As_4 flux. CT24 buffer layer growth was performed at 320 °C under 2.87 x 10^{-7} Torr Te_2 and 5.73 x 10^{-7} Torr CdTe fluxes for 120 minutes. RHEED patterns corresponding to the CT24 buffer layer after the growth was shown in Figure 46.b. In this figure, a single spot seems clear and shiny the others are seen a slightly faint. Furthermore, the intensity of RHEED patterns was decreased as a result of rough sample surface structure.

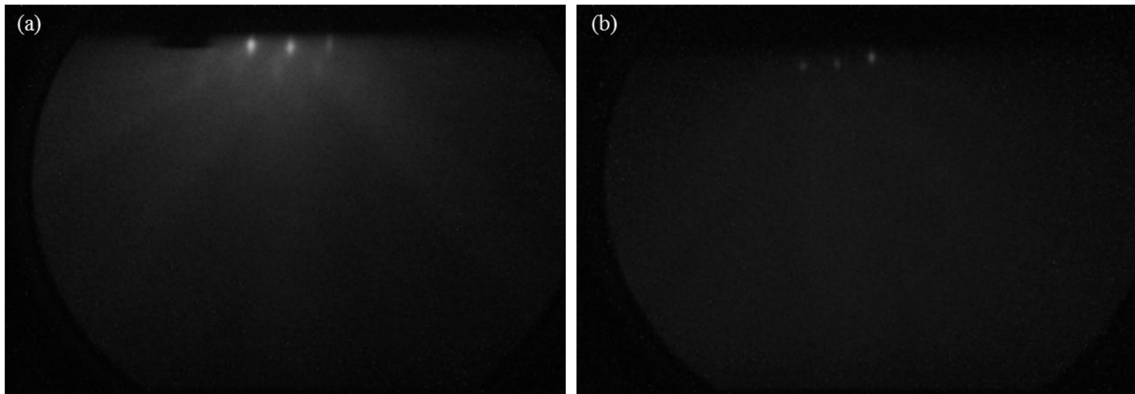

Figure 46. [01-1] RHEED patterns of CT24 (a) after oxide desorption at 580 °C and (b) after growth at 320 °C.

CT25 buffer layer was grown on 20x20 mm^2 epi-ready GaAs (211)B substrates. Base pressure of the MBE system was 3.5 x 10^{-10} Torr before the growth and during the growth process, the sample was rotated 2 rpm. The GaAs native oxide desorption was performed at 583 °C for 4 minutes under 2.2 x 10^{-6} Torr As_4 flux. During the oxide removal process, the surface structure changes of GaAs wafer was recorded by RHEED. In Figure 47.a, [01-1] RHEED patterns became streaky patterns after the oxide desorption. After deoxidation, nucleation layer growth and annealing processes, the substrate temperature was heated at 295 °C under 1.29 x 10^{-7} Torr Te_2 and 5.14 x 10^{-7} Torr CdTe fluxes for 120 minutes. [01-1] RHEED patterns on fluorescent screen in Figure 47.b are shown CT25 sample surface at the end of the growth process. In this figure, streaky RHEED patterns changed to slightly spotty patterns.

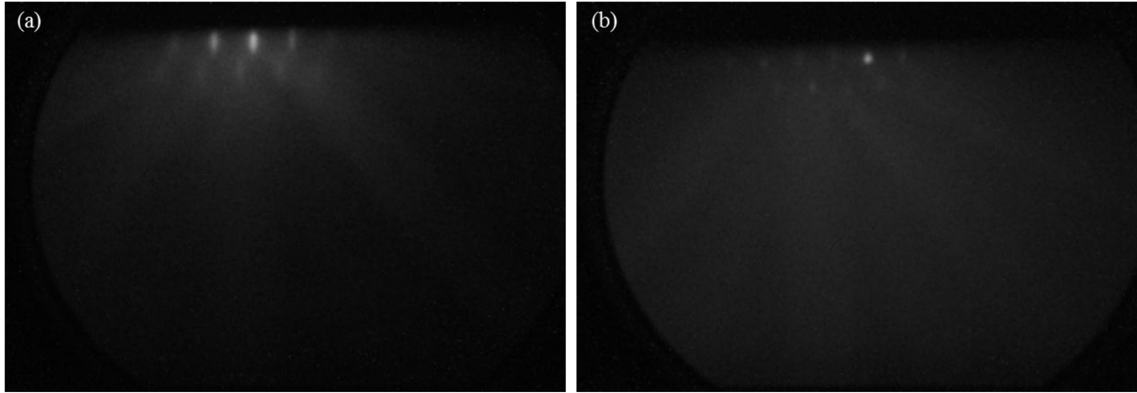

Figure 47. [01-1] RHEED patterns of CT25 (a) after oxide desorption at 583 °C and (b) after growth at 295 °C.

CT26 buffer layer was grown on 20x20 mm^2 epi-ready GaAs (211)B square substrate. Base pressure of the MBE system was 3.4 x 10^{-10} Torr before the growth and the sample was rotated 2 rpm during the growth process. The GaAs native oxide desorption was carried out at 582 °C for 4 minutes under 2.21 x 10^{-6} Torr As_4 flux. In Figure 48.a, at the end of the GaAs oxide desorption process, the RHEED pattern was streaky along [01-1] direction. After deoxidation, nucleation layer growth and annealing steps, the substrate temperature was heated to the growth temperature of 295 °C under only 5.15 x 10^{-7} Torr CdTe flux for 120 minutes. [01-1] RHEED patterns on fluorescent screen in Figure 48.b are shown for CT26 sample surface at the end of the growth process. Streaky RHEED patterns were shown in this figure and RHEED intensity did not change significantly.

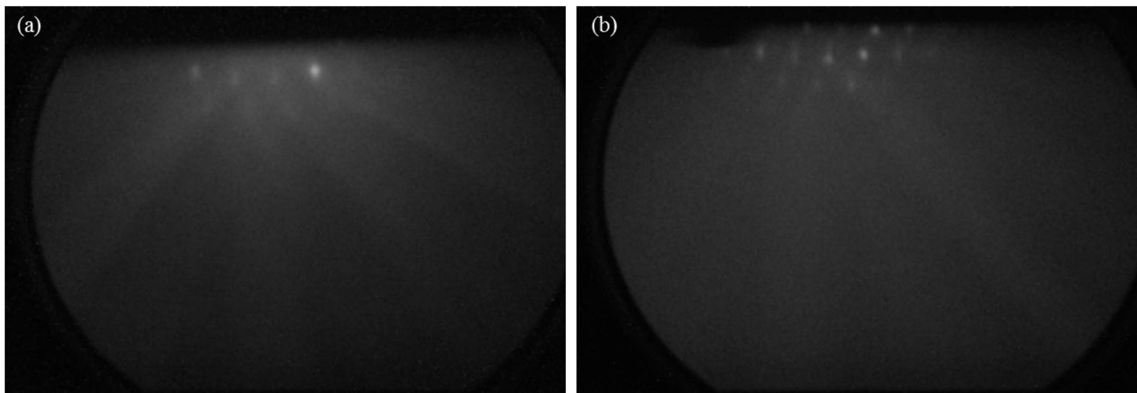

Figure 48. [01-1] RHEED patterns of CT26 (a) after oxide desorption at 582 °C and (b) after growth at 295 °C.

20x20 mm^2 epi-ready GaAs (211)B substrates were used to grow CT27 buffer layer. Before the growth, base pressure of the MBE system was 4.37 x 10^{-10} Torr. The substrate was rotated with 2 rpm during the growth. The GaAs native oxide was desorbed at 584 °C for 4 minutes under 2.23 x 10^{-6} Torr As_4 flux. The [01-1] RHEED patterns were streaky and intense at the end of the GaAs oxide desorption step as shown in Figure 49.a. After oxide desorption, nucleation layer growth and annealing steps, the substrate temperature was heated to the growth temperature of 302 °C under 4.16 x 10^{-7} Torr Te_2 and 5.55 x 10^{-7} Torr CdTe fluxes for 120 minutes. [01-1] RHEED patterns on the screen in Figure 49.b are shown CT27 sample surface at the end of the growth process. In this figure, a single spot seems clear and shiny the others are seen a slightly faint. Compared to the Figure 49.a and Figure 49.b, RHEED patterns were changed streaky to spotty patterns and intensity was decreased. Rough surface morphology causes the intensity decreasing and spotty patterns.

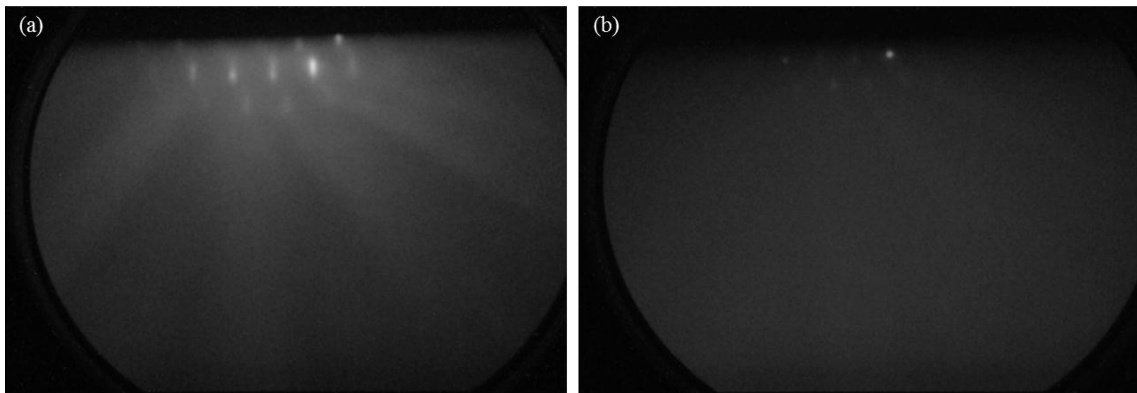

Figure 49. [01-1] RHEED patterns of CT27 (a) after oxide desorption at 584 °C and (b) after growth at 302 °C.

The central streak in the RHEED pattern gives the knowledge about interplanar distance between crystal planes [98]. To calculate the interplanar spacing (d_{hkl}), firstly, the distance between streaks was measured. RHEED fluorescent screen size which was used in these experiments was 135 mm. 2D RHEED images were monitored into interactive 3D surface images by using a software program [105] and the most intense points of the RHEED spots could be observed by using these 3D images. The spacing between the most intense points of the spots was measured by using a different software program [106]. The measured values converted into the millimeter with reference to the

size of fluorescent screen. To obtain the value of interplanar spacing, below equation was used.

$$d_{hkl} = \left(\frac{L}{D}\right) \times \lambda \tag{6. 2}$$

where L is distance between sample and the RHEED screen and D is the distance between spots. Wavelength is obtained from the energy value of the incident beam (equation 5.7). To calculate the lattice constant of reciprocal space,

$$a^* = \frac{2\pi}{\sqrt{(h^2+k^2+l^2)d^2}}. \tag{6. 3}$$

In this thesis, RHEED pattern images which were monitored along [01-1] were used. Therefore; h,k and l miller indices were taken as 0,1 and -1, respectively. The calculated reciprocal lattice constants for CT22, CT24, CT25, CT26 and CT27 buffer layers are summarized in Table 4.

Table 4. Calculated lattice constants and percentage error values of buffer layers.

Sample No	**λ (Å)**	**L (mm)**	**D (mm)**	**d (Å)**	**a* (calculated, Å)**	**a* (real, Å)**	**Error%**
CT22	0.079162	456.55	8.35	4.33	0.974	0.9696	5.6
CT24	0.079162	456.55	8.24	4.38	0.985	0.9696	4.5
CT25	0.079162	456.55	8.19	4.41	0.993	0.9696	3.7
CT26	0.079162	456.55	8.10	4.46	1.054	0.9696	2.7
CT27	0.079162	456.55	8.37	4.32	0.972	0.9696	5.8

6.3. Structural Analysis of As-Grown CdTe (211)B Buffer Layers

6.3.1. Nomarski Characterization Results

The as-grown buffer layers' surface morphologies were also observed using Nomarski microscopy (A13.1013 BF/DF DIC Metallurgical Microscope) to examine a wide area of the samples surface with 100x objective focus. Yellow filter is suitable to observe semiconductor materials and turning the adjusting lever of the Nomarski microscope, best image contrast can be chosen.

CT6, CT9 and CT10 buffer layers were grown on epi-ready GaAs substrates. The native oxide of GaAs substrates were desorbed at 650 °C for CT6 and CT9, also deoxidation process occurred at 600 °C for CT10 for 4 minutes under As_4 flux. CdTe nucleation layers were grown for 30 seconds at 280 °C, 250 °C and 250 °C for CT6, CT9 and CT10, respectively. The substrate temperature was heated to the 310 °C under Te_2 flux for these three samples and growths were carried out at a rate of about 1 μm/h.

As shown in Figure 50, the substrate and/or growth related as-grown surface defects were not fully resolved for CT6 and CT9. For CT10, these defects were better resolved than CT6 and CT9. Furthermore, the relative value of average surface roughness can be estimated from Figure 50 to make comparison.

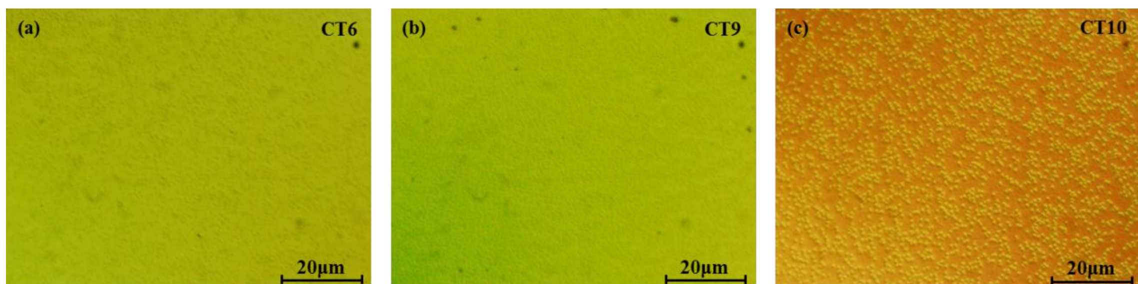

Figure 50. Nomarski microscopy as-grown images of (a) CT6, (b) CT9 and (c) CT10 at 100x magnification.

CT22, CT24, CT25, CT26 and CT27 buffer layers were grown on epi-ready GaAs (211)B substrates. Oxide desorption steps for these buffer layers were performed at 580 °C for 4 minutes under As_4 flux. After deoxidation, nucleation layers were grown for 10 minutes at 220 °C. Nucleation layers were also annealed at 385 °C for 5 minutes. Finally, buffer layers growth were carried out in 120 minutes at 300 °C and growths

were also performed at a rate of about 1 μm/h. Slight change in growth temperatures from run to run does not significantly affect for CdTe buffer layer growth. The only differences between CT22, CT24, CT25, CT26 and CT27 samples is the flux ratios which are 3, 2, 1.5, 1 and 2.5, respectively.

In Figure 51, the first notable samples were CT24 and CT27. The substrate and/or growth related as-grown surface defects were not seen for CT24 and CT27 surface was rougher than other buffer layers. CT25 as-grown surface related defects could be distinguished more clearly than CT22, CT26 and CT27 at this magnification.

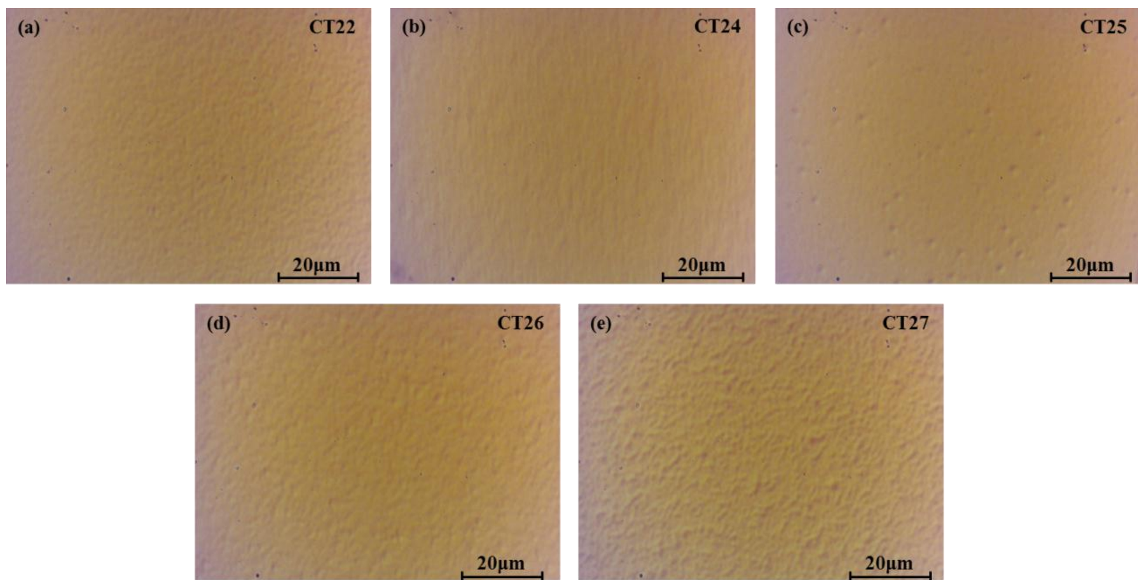

Figure 51. Nomarski microscopy as-grown images of (a) CT22, (b) CT24, (c) CT25, (d) CT26 and (e) CT27 at 100x magnification.

6.3.2. AFM Characterization Results

To investigate the surface root mean squared (RMS) roughness, substrate and/or growth-related surface defects and smooth step-terrace structures which were occurred due to growth on (211) crystal orientation, AFM topographical images of CdTe/GaAs (211)B buffer layers were used. These images were obtained in the semi-contact mode with using Solver-Pro 7 system. During the AFM measurements, silicon tips and golden tips with cantilever thicknesses of 1.75 μm and 1.5 μm, force constants of 3.5-12 N/m and 0.35-6.1 N/m were used, respectively.

Topographic images of as-grown CdTe buffer layers were obtained from a 10x10 μm^2 scanned area. To obtain the average RMS roughness value for each sample, roughness values of five different scanned regions were averaged. In order to investigate the widths and depths of substrate and/or growth-related surface defects were specified in this thesis by using AFM length and cross-section analyze tools. In Figure 52, AFM 2D and 3D topographical images, length and cross-section analyze tools for as-grown CT9 sample are shown. The average RMS roughness value from the five different scanned areas for CT9 was found as 13.6 nm. Average size of as-grown surface defects was about 0.6 μm and average depth was about 90 nm. Also the average substrate and/or growth related surface defect density was calculated as 8.3×10^7 cm^{-2} for CT9.

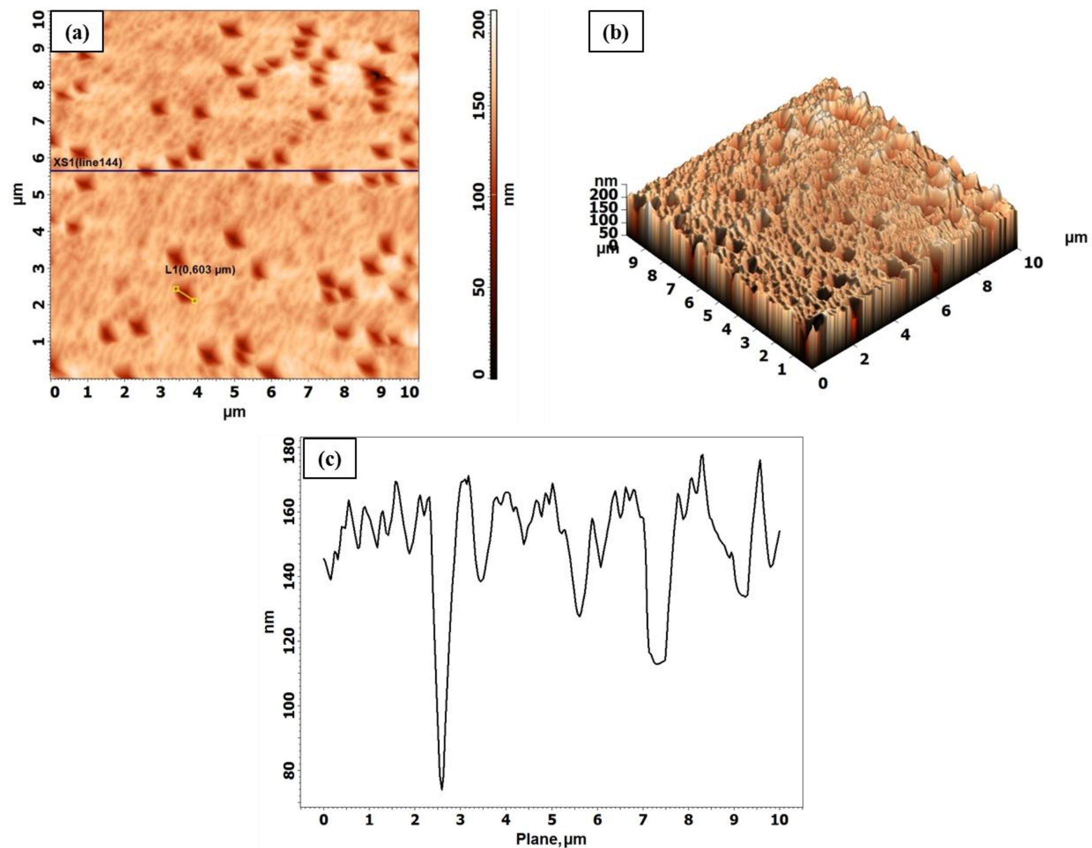

Figure 52. (a) AFM 2D and (b) 3D topographical images of CT9 as-grown sample and (c) cross-section line analysis of XS1(line 144).

AFM 2D and 3D topographical images, length and cross-section analyze tools for as-grown CT22 sample are shown in Figure 53. Five different scanned regions were used to obtain average RMS value for this sample and found to be about 4.2 nm.

Average size of as-grown surface defects was nearly 1.3 μm and average depth was nearly 80 nm. Also the average substrate and/or growth related surface defect density was counted as $0.1x10^7$ cm^{-2} for CT22.

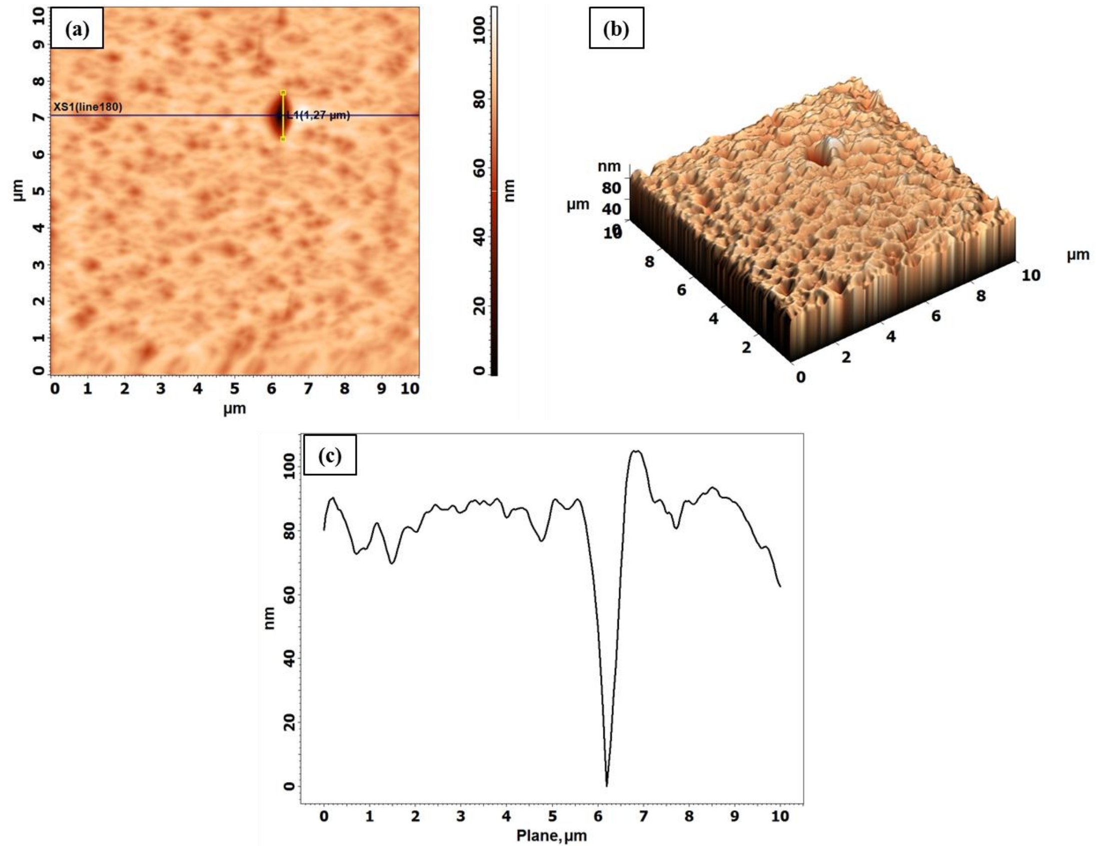

Figure 53. (a) AFM 2D and (b) 3D topographical images of CT22 as-grown sample and cross-section line analysis of XS1(line 180).

In Figure 54, AFM 2D and 3D topographical images, length and cross-section analysis tools for as-grown CT26 sample are shown. The average RMS roughness value from the five different scanned areas for CT26 was found approximately 8.7 nm. Average size of as-grown surface defects was about 1 μm and average depth was about 90 nm. Also the average substrate and/or growth related surface defect density was calculated as $6.3x10^7$ cm^{-2} for CT26.

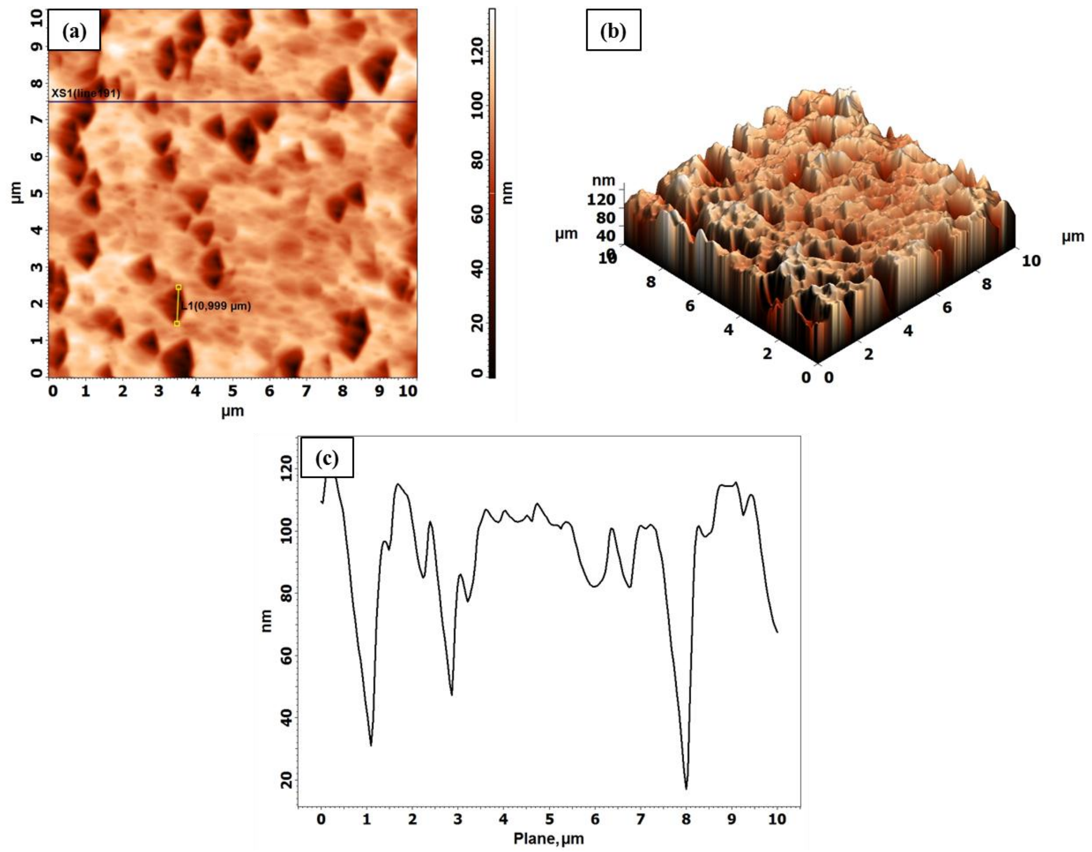

Figure 54. (a) AFM 2D and (b) 3D topographical images of CT26 as-grown sample and cross-section line analysis of XS1(line 191).

AFM images for the rest of the samples were given under the section 6.5.2. Average RMS roughness values, average size and average depth values of as-grown surface defects for all buffer layers are given in the Table 5.

Table 5. AFM characterization results for as-grown CdTe buffer layers.

Sample No.	RMS (nm)	Avg. Size (µm)	Avg. Depth (nm)	As-grown Defect Density ($x10^7 cm^{-2}$)
CT6	10.6	0.5	70	3.6
CT9	13.6	0.6	90	8.3
CT10	16	1.1	90	4.4
CT22	4.2	1.3	80	0.1
CT24	14.4	–	–	–
CT25	5.9	0.8	50	0.9
CT26	8.7	1	90	6.3
CT27	21.5	–	–	–

We thinned down the CT10 sample in steps to investigate the source of as-grown surface defects; whether they were substrate or growth-related by using Br_2-MeOH solution. CT10 sample was used for this experiment because of its higher thickness than others (~5 µm). AFM 2D topographical image, length and cross-section analyze tools for as-grown CT10 sample are shown in Figure 55. As-grown CT10 buffer layer average RMS roughness value was found as 16 nm. Average size of as-grown surface defects was about 1.1 µm and average depth was about 90 nm. The average substrate and/or growth related surface defect density was calculated as $4.4x10^7$ cm^{-2} for CT10.

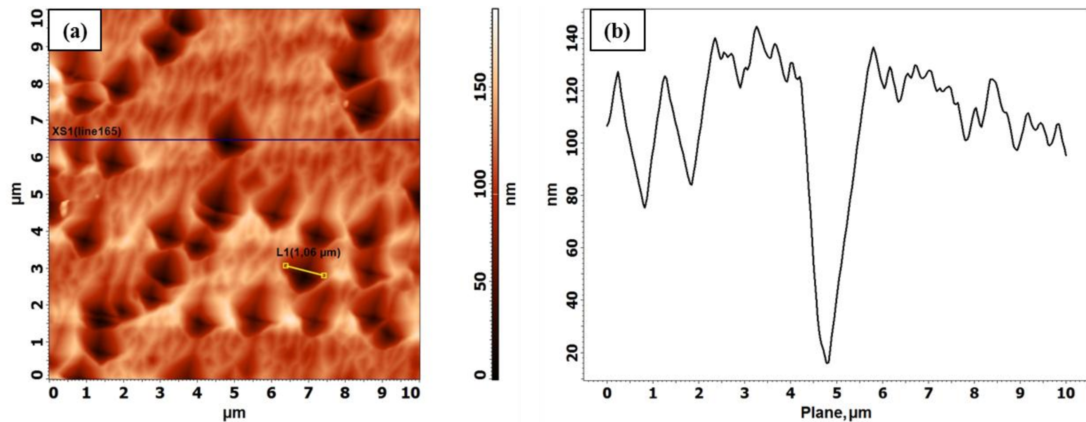

Figure 55. (a) AFM 2D topographical image and (b) and cross-section line analysis of XS1(line 165) of CT10 as-grown sample.

CT10 as-grown buffer layer was started to polish with prepared 0.5% Br_2-MeOH mixture for about 2 second and then rinsed in methanol and also finally dried with N_2. The surface morphology of the sample after this step is shown in Figure 56. The average RMS roughness value of polished sample was found to be approximately 5 nm. Average size of as-grown surface defects was about 0.4 µm and average depth was about 25 nm.

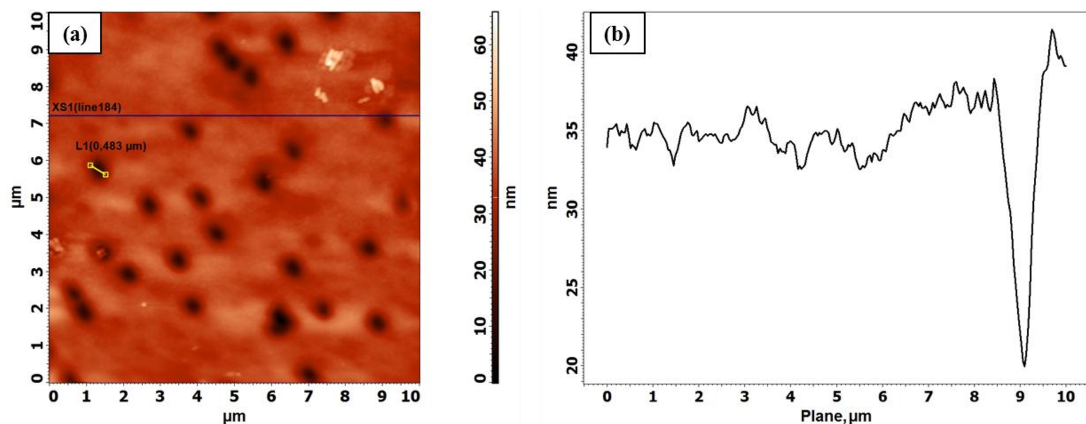

Figure 56. (a) AFM 2D topographical image and (b) and cross-section line analysis of XS1(line 184) after CT10 polished with 0.5% Br_2-MeOH for 2 seconds.

After first polishing step, CT10 sample was polished again with same mixture for about 10 second. In Figure 57, AFM 2D topographical image showed the changes of surface morphology. The average RMS roughness value of 10 second polished sample was found approximately 1.9 nm. Average size of as-grown surface defects was about 0.6 µm and average depth was about 4 nm.

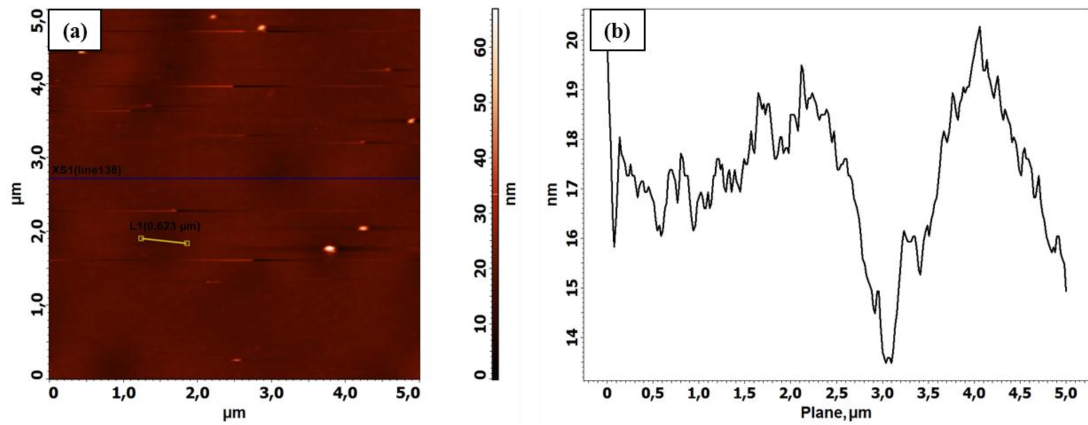

Figure 57. (a) AFM 2D topographical image and (b) and cross-section line analysis of XS1(line 138) after CT10 polished with 0.5% Br_2-MeOH for 10 seconds.

For the final step of this experiment, CT10 sample was polished with the same mixture for about 15 second. The change in the surface morphology and the average RMS roughness can be seen in Figure 58. The average RMS roughness value of 15 second polished sample was found approximately 1.2 nm. Average size of as-grown surface defects was about 1.1 µm and average depth was about 2.5 nm.

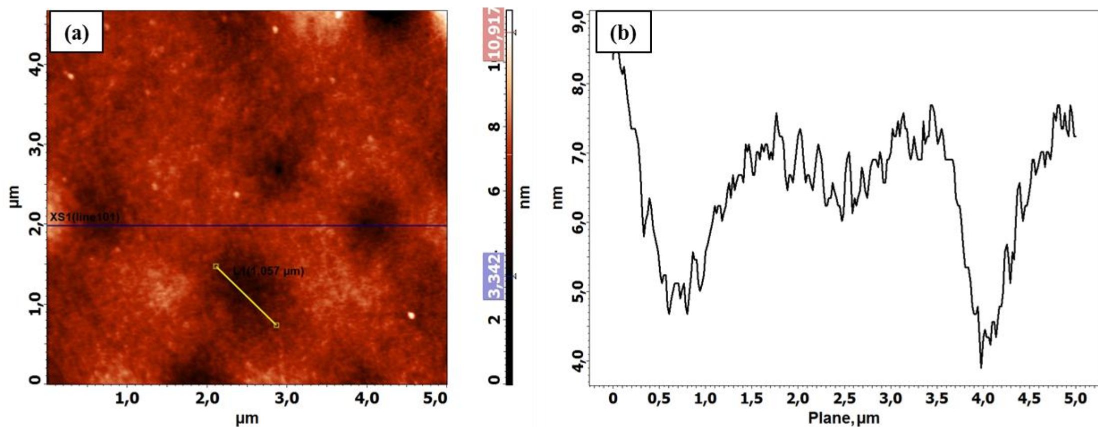

Figure 58. (a) AFM 2D topographical image and (b) and cross-section line analysis of XS1(line 101) after CT10 polished with 0.5% Br_2-MeOH for 15 seconds.

When the polishing experiment was tried for more than 15seconds, the sample surface began to damage. Polishing process was continued until the depth of surface defects approximately unchanged with respect to Figure 59. After these polishing steps, the number of as-grown surface defects was almost constant and depth of these defects decreased to about approximately 88nm. This means the as-grown surface defects were

not due to substrate oxide removal before the growth or substrate related, but growth conditions related [1].

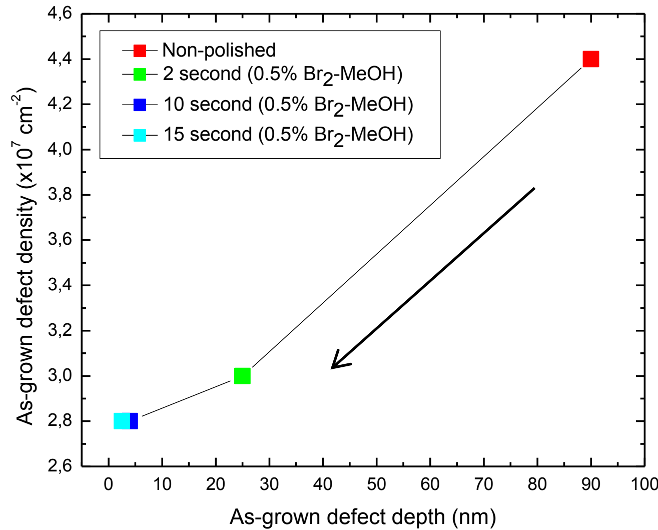

Figure 59. Comparison between as-grown defect density and as-grown defect depth.

6.3.3. SEM Characterization Results

The surface morphology and the areal density of growth-related as-grown surface defects were obtained by manual counting and by a computer program from the SEM images. Samples without applying any conducting coatings were analyzed with accelerated electrons under 5 kV and 3 spot size (except CT9). Working distance was nearly 10 mm and images were obtained by Everhart- Thornley Detector (ETD) at 25000x magnification.

As-grown surface defects which are related to growth conditions can be seen clearly in Figure 60. As-grown surface defect densities were counted by manual and using a software program [105] and calculated areal defect density values were found as $3.6x10^7$ cm^{-2}, $8.1x10^7$ cm^{-2} and $5.1x10^7$ cm^{-2} for CT6, CT9 and CT10, respectively. As-grown surface defect density values obtained by AFM images are in good agreements with those obtained from SEM images for these three samples.

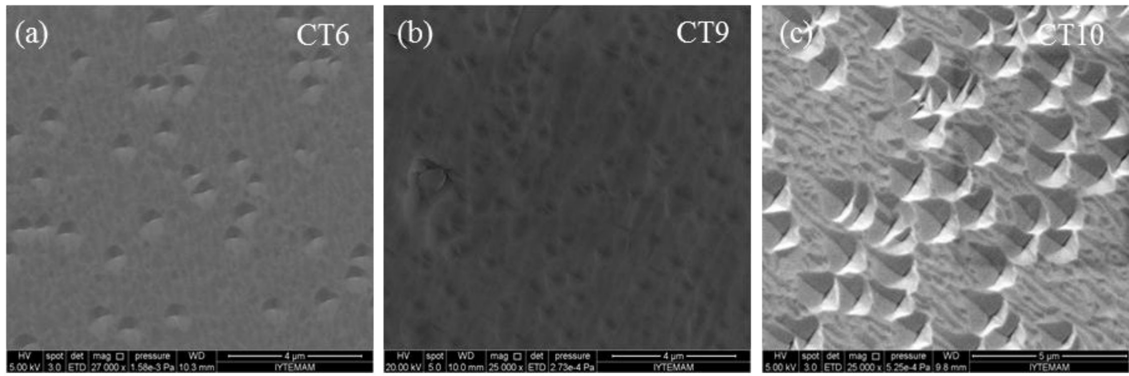

Figure 60. SEM images of as-grown (a) CT6, (b) CT9 and (c) CT10 samples at 25000 magnification.

In Figure 61, as-grown surface related defects can be clearly seen except CT24 and CT27 buffer layers. For these two samples, there are no improper growth condition related surface defects. Therefore, areal density of as-grown surface defects cannot be calculated for CT24 and CT27. As-grown surface defect densities were counted by manual and using a software program [105] and areal defect density values were calculated as approximately 0.2×10^{7} cm^{-2}, 1.4×10^{7} cm^{-2} and 6.7×10^{7} cm^{-2} for CT22, CT25 and CT26, respectively. As-grown surface defect density values obtained by SEM images are in good agreements with those obtained from AFM images for these three samples.

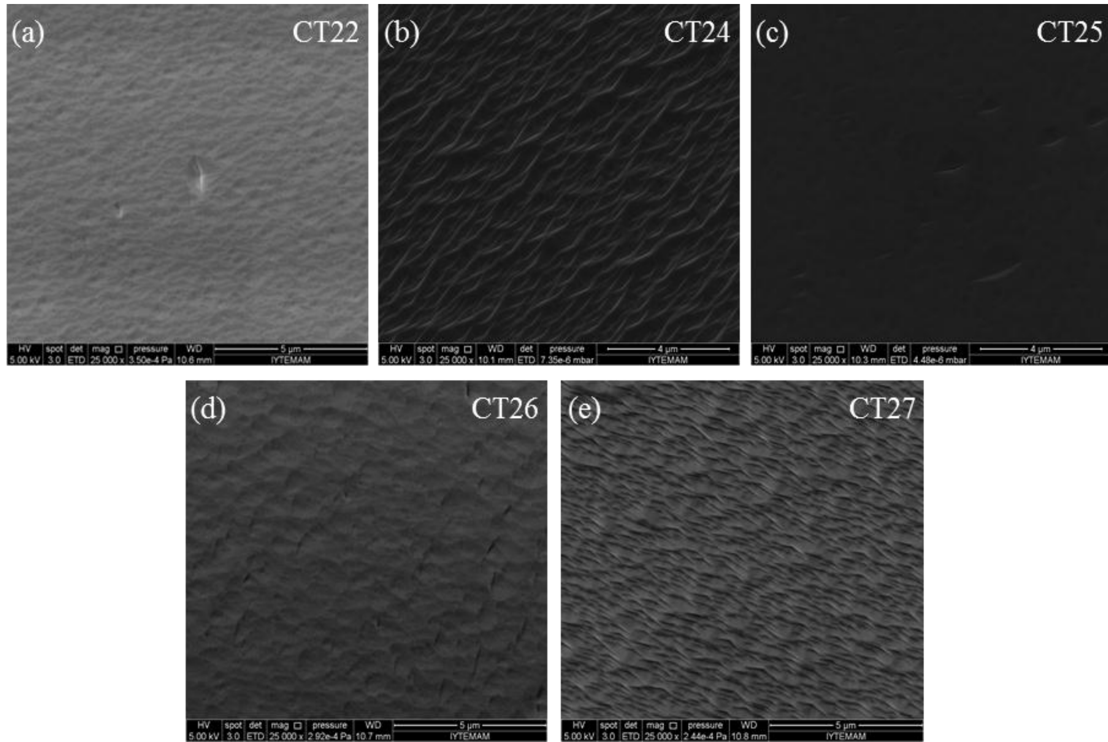

Figure 61. SEM images of as-grown (a) CT22, (b) CT24, (c) CT25, (d) CT26 and (c) CT27 samples at 25000 magnification.

6.4. Defect Decoration Etching Processes of CdTe (211)B Epilayers

As grown CdTe samples were diced into several pieces and standard EPD method were applied. Etching times were kept shorter than the usual etching times to prevent overlapping of the pits for accurate EPD measurements. We focused our investigation on two different etch methods: Everson and Nakagawa. It was reported that Nakagawa etching is effective only for the (111)A crystal orientation [75].

In order to apply the etching procedures, the Everson ($C_2H_4OHCOOH$: HNO_3: HF) and the Nakagawa (H_2O: H_2O_2: HF) etch solutions were prepared with various volume ratios in polypropylene beakers at room temperatures under the fume hood. The chemical reaction taking place during etch pit formation consists of oxidation and dissolution of the oxide steps and the volume ratios of the constituents of the etching solution decide the rate of each processes. Therefore, we tried different volume ratios of these etchants to adjust etch rate on CdTe (211)B samples. For etching, a diced piece of the sample was dipped into these mixtures with gentle stirring at room temperature. The samples were rinsed in DI water and dried with high purity N_2.

In a large number of different volume ratios and implementation times were tried for CT6 and CT9 samples. This was done to find an appropriate volume ratio and implementation time for both the Everson and the Nakagawa etch methods which were used for approximately ~ 2 μm thick samples. For the Everson etching, two different volume ratios and etch times, can be specified as E4 ($25C_2H_4OHCOOH$: $4HNO_3$: 0.5HF, 20s) and E1 ($25C_2H_4OHCOOH$: $4HNO_3$: 1HF, 15s) in Table 6, have been found. E1 and E4 methods were compared separately by using Nomarski, AFM, SEM and Raman spectroscopy mapping characterization techniques. Even though there were no large differences between E1 and E4, E1 was chosen to compare our results with those given in the literature [69]. A single appropriate volume ratio ($20H_2O$: $20H_2O_2$: 30HF) with 7 s. implementation time was determined for the Nakagawa etching.

Table 6 shows the etching methods, volume ratios of etching solutions, etch time and the EPD values for two epilayers studied. The results obtained from the Everson and the Nakagawa etchings were examined for both samples by using different surface characterization methods. EPD results are indicated that decreasing the application time of etchants in both of techniques led to a slight increase in EPD values. This might be due to overlapping of enlarged pits to a larger pit for a longer etching. It was shown that the etch pit size depended on the etching implementation time and solution volume ratios. It was also seen in this table, EPD results of CT9 higher than the CT6. This might be the result of differences in growth conditions.

Table 6. Defect decoration methods, volume ratios, etching times and EPD values for CT6 and CT9

Sample #	Etch Methods		Volume Ratios	Etch times (s)	EPD (cm^{-2})
CT6	Everson ($C_2H_4OHCOOH:HNO_3:HF$)	E1	25:4:1	15	$7.9x10^7$
		E2	25:4:2	15	$9.3x10^7$
		E3	25:8:1	20	NA
		E4*	25:4:0.5	20	$8.6x10^7$
	Nakagawa ($H_2O:H_2O_2:HF$)	N1	20:20:30	20	NA
		N2*		7	$1.4x10^7$
CT9	Everson ($C_2H_4OHCOOH:HNO_3:HF$)	E1*	25:4:1	15	$1.4x10^8$
		E2	25:4:2	15	NA
		E4	25:4:0.5	15	$8.3x10^7$
		E6	25:4:1	10	$1.8x10^8$
	Nakagawa ($H_2O:H_2O_2:HF$)	N2*	20:20:30	7	$4.8x10^7$
		N3		5	$6.5x10^7$

(Etching methods which had been marked with asterisks* were examined in this thesis.)

To examine other samples, E1 and N2 were decided as optimum volume ratios and etch times for the Everson and Nakagawa etching methods, respectively.

Table 7. EPD results for different samples by applying E1 and N2 methods.

Etch Method	Sample #	EPD (x10^8 cm^{-2})
E1	CT10	0.7
	CT22	1.1
	CT24	2.3
	CT25	0.3
	CT26	0.4
	CT27	3.8
N2	CT10	0.4
	CT22	0.03
	CT24	–
	CT25	0.04
	CT26	0.6
	CT27	–

The EPD results which were given in the Table 6 and Table 7 were calculated from SEM images with using imageJ [105] computer program.

6.5. Structural Analysis Results of Wet Chemically Etched CdTe

6.5.1. Nomarski Characterization Results

Nomarski microscopy was also used to determine buffer layers surface topography and a surface morphology changes after the Everson etch and the Nakagawa etch solutions. The pits were not fully resolved for all etched samples at a magnification of 100x. Therefore, we did not attempt to count defects to establish their areal density from these images. On the other hand, the relative concentration of the defects from these images good enough to make comparison.

CT6 as-grown surface seemed to have relatively defect free surface. In Figure 62, Everson etch produced larger pits compared to Nakagawa etch on CT6 sample. The

same was also true for the CT9 buffer layer. CT9 sample had more defects on the as-grown surface compared to first sample. Etch pits produced by Nakagawa method was better resolved in Nomarski images than those produced by Everson method (Figure 63).

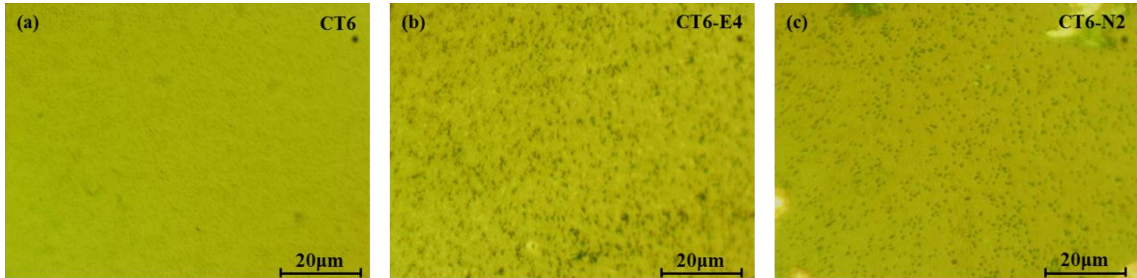

Figure 62. Nomarski microscopy images of (a) as-grown surface, (b) E1 etched surface and (c) N2 etched surface for CT6 at 100x magnification.

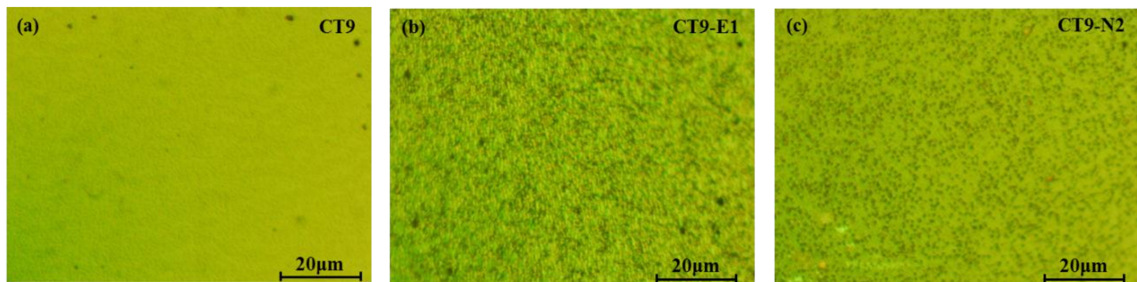

Figure 63. Nomarski microscopy images of (a) as-grown surface, (b) E1 etched surface and (c) N2 etched surface for CT9 at 100x magnification.

As-grown surface defects, Everson etch pits and Nakagawa etch pits were better resolved at 100x magnification for CT10 sample. Nakagawa etch produced smaller etch pits compared to Everson etch on CT10 buffer layer which could be seen from Figure 64.

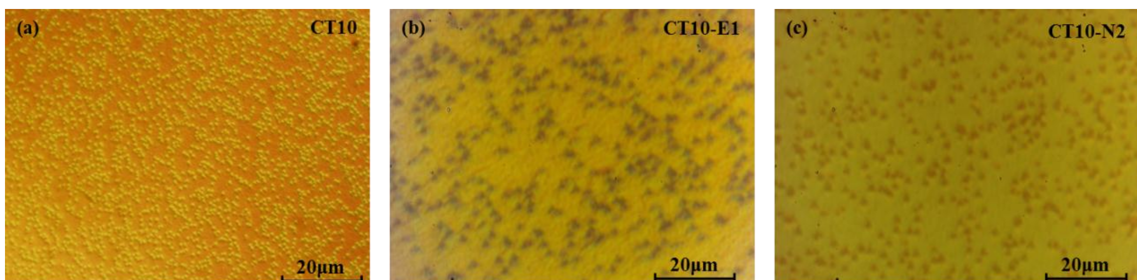

Figure 64. Nomarski microscopy images of (a) as-grown surface, (b) E1 etched surface and (c) N2 etched surface for CT10 at 100x magnification.

As-grown surface of CT22 seemed to have relatively growth-related defect free surface. In Figure 65, Everson etch produced some larger pits on the surface and these larger ones could be seen clearly, others were indistinguishable. Furthermore, Nakagawa etch produced larger pits than CT6, CT9 and CT10 samples. Etch pit density value from the Nakagawa etch lower than all other buffer layers.

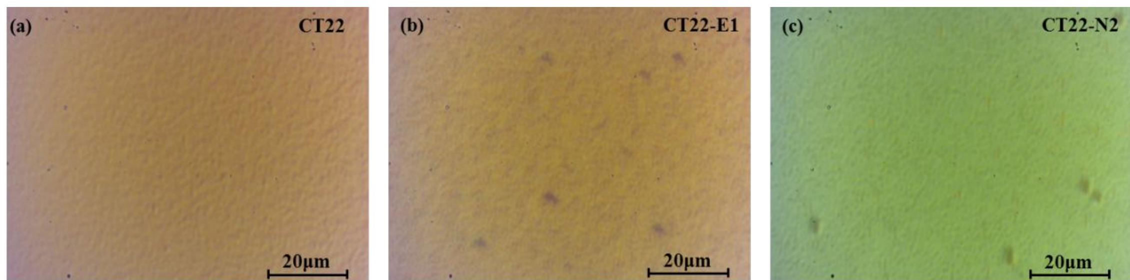

Figure 65. Nomarski microscopy images of (a) as-grown surface, (b) E1 etched surface and (c) N2 etched surface for CT22 at 100x magnification.

In Figure 66, there are no improper growth condition related surface defects for CT24 buffer layer surface. In Figure 66.d, Nakagawa solution could not etch the sample surface. From this image, no more comment could be made for both etch technique.

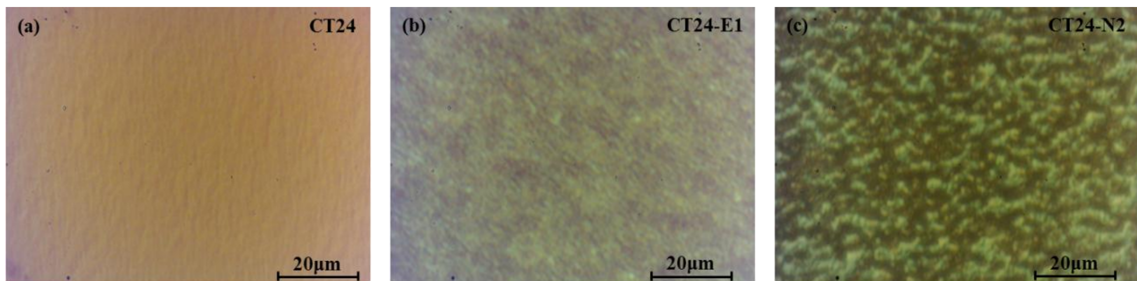

Figure 66. Nomarski microscopy images of (a) as-grown surface, (b) E1 etched surface and (c) N2 etched surface for CT24 at 100x magnification.

CT25 as-grown surface related defects could be distinguished more clearly than CT26 at this magnification. Nakagawa etch produced larger pits compared to Everson etch on CT25 sample (Figure 67). The same was also true for the CT26 buffer layer (Figure 68). CT26 sample had more defects on the as-grown surface compared to CT25 etched sample. CT25-E1 etched sample had smaller pits with respect to CT26-E1 etched sample. Contrary to this, CT25-N2 etched sample had larger pits compared to CT26-N2 etched sample. Etch pit density value from the Nakagawa etch for CT25-N2 lower than

CT26-N2. Etch pits produced by Nakagawa method was better resolved in Nomarski images than those produced by Everson method like as other images.

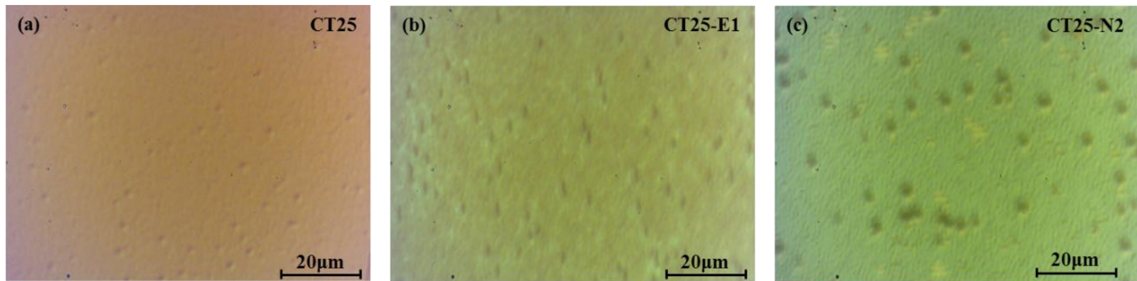

Figure 67. Nomarski microscopy images of (a) as-grown surface, (b) E1 etched surface and (c) N2 etched surface for CT25 at 100x magnification.

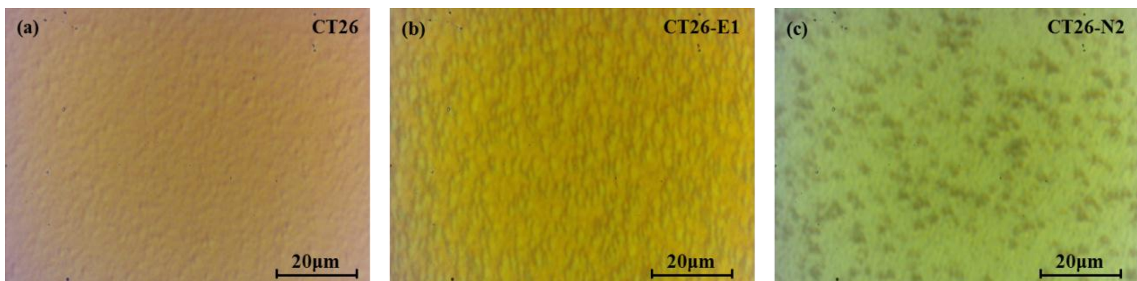

Figure 68. Nomarski microscopy images of (a) as-grown surface, (b) E1 etched surface and (c) N2 etched surface for CT26 at 100x magnification.

As-grown surface of CT27 seemed to have some relatively growth-related defects (Figure 69). However; in Figure 69.d, Nakagawa solution could not etch the sample surface. In a similar manner for CT24, actually there are no improper growth condition related surface defects for CT27. Because of rough surface, as- grown surface of CT27 seemed have some surface defects. No comment could be made for CT27-E1 etched sample surface like a CT24-E1 etched sample surface.

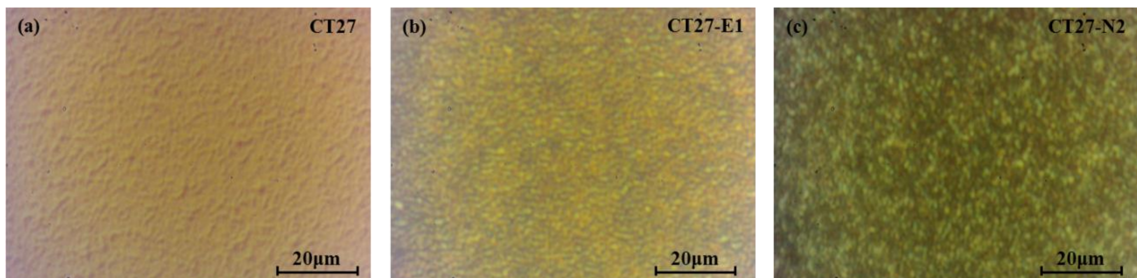

Figure 69. Nomarski microscopy images of (a) as-grown surface, (b) E1 etched surface and (c) N2 etched surface for CT27 at 100x magnification.

6.5.2. AFM Characterization Results

The etch pits were then observed using AFM in a semi-contact mode. The widths and depths of the etch pits were measured by using AFM length and cross-section analysis tools. AFM 10µmx10µm topographic images, pit width and cross section line analysis on these images for CT6 are shown in Figure 70. In this figure it can be seen that E4 etched CT6 has well-defined "triangular" etch pits on the surface (Figure 70.a). Average size of these pits was about 0.9 µm and average depth was about 260 nm. Figure 70.c shows the N2 etch pits formed on CT6. These etch pits had about 1.3 µm average size and about 360 nm average depth (Figure 70.d). From Figure 70.a and Figure 70.c, EPD values were counted as ~$7.3x10^7cm^{-2}$ for CT6-E4 and ~$1.5x10^7cm^{-2}$ for CT6-N2.

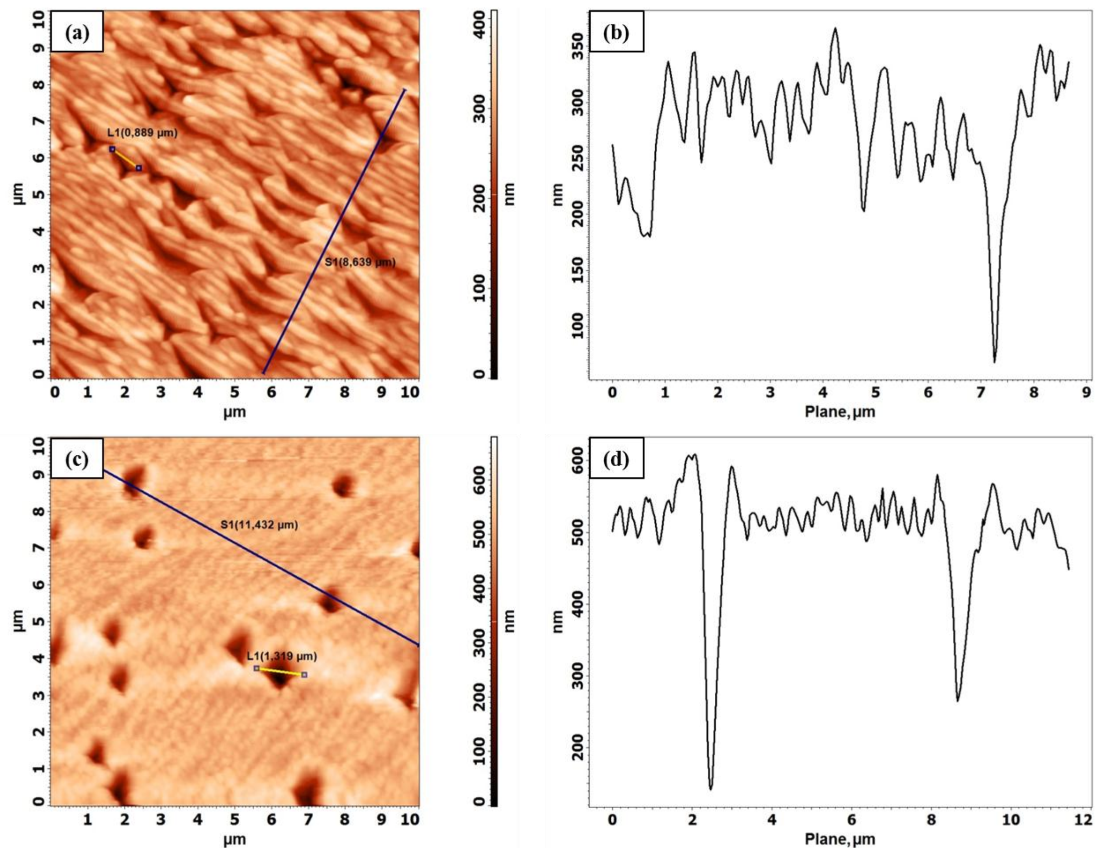

Figure 70. CT6 AFM 2D topographical images of (a) and (b) length analysis and cross-section line analysis of pits after CT6-E4 etch; (c) and (d) length analysis and cross-section line analysis of pits after CT6-N2 etch.

In Figure 71, AFM topographical images of E1 and N2 etch pits for CT9 sample indicates that the CT9-E1 method creates the "triangular" pits which have an average

size ~ 1.5 μm and average depth ~ 245 nm on the sample. Similar to the other sample CT9-N2 etch reveals etch pits (Figure 71.c). These etch pits have ~ 0.8 μm average size and ~ 420 nm average depth. From Figure 71.a and Figure 71.c, EPD values were found as ~$8.4x10^7 cm^{-2}$ for CT9-E1 and ~$4.1x10^7 cm^{-2}$ for CT9-N2.

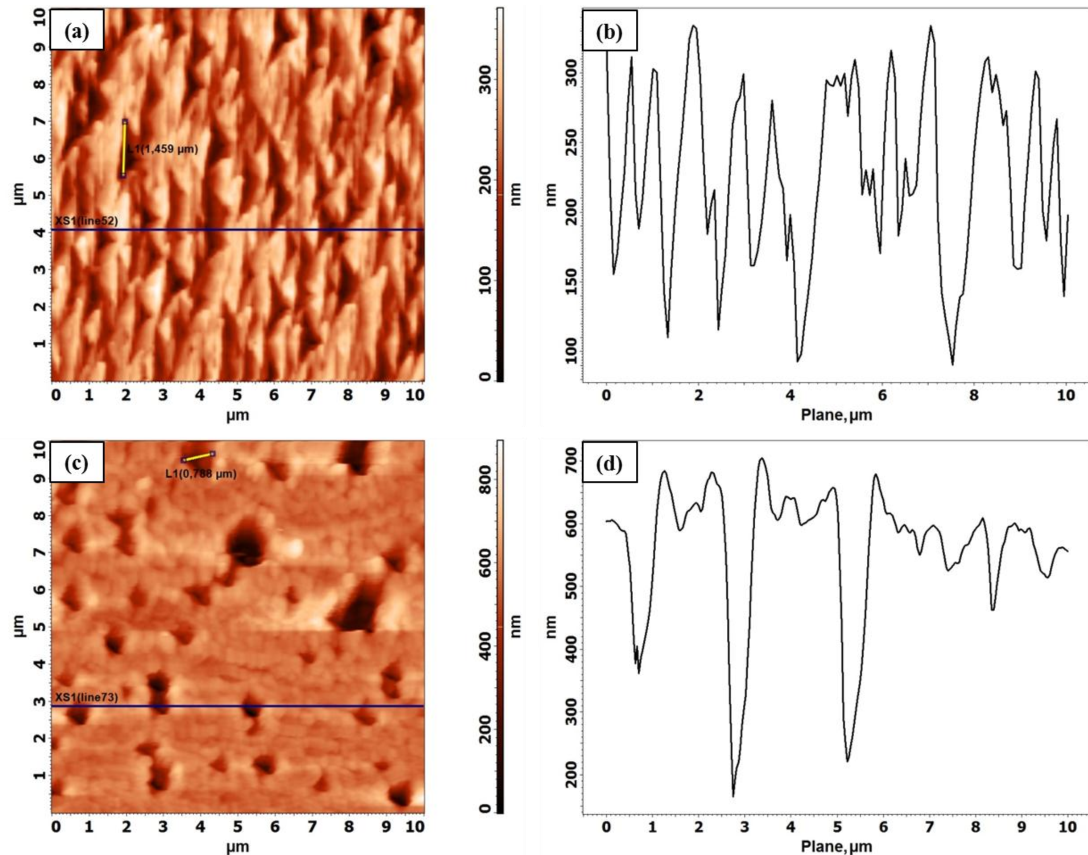

Figure 71. CT9 AFM 2D topographical images (a) and (b) length analysis and cross-section line analysis of pits after CT9-E1; (c) and (d) length analysis and cross-section line analysis of pits after CT9-N2 etch.

In Figure 72, AFM 10x10 $μm^2$ scanned regions of E1 and N2 etch pits for CT10 sample has well-defined “triangular” etch pits and Nakagawa etch pits on the surface. Average size of these “triangular” pits was about 1 μm and average depth was about 190 nm. Figure 72.c shows the CT10-N2 etch pits formed on sample surface. These etch pits had about 0.6 μm average size and about 410 nm average depth. EPD values were calculated as ~$5x10^7 cm^{-2}$ for CT10-E1 and ~$4x10^7 cm^{-2}$ for CT10-N2 from Figure 72.a and Figure 72.c.

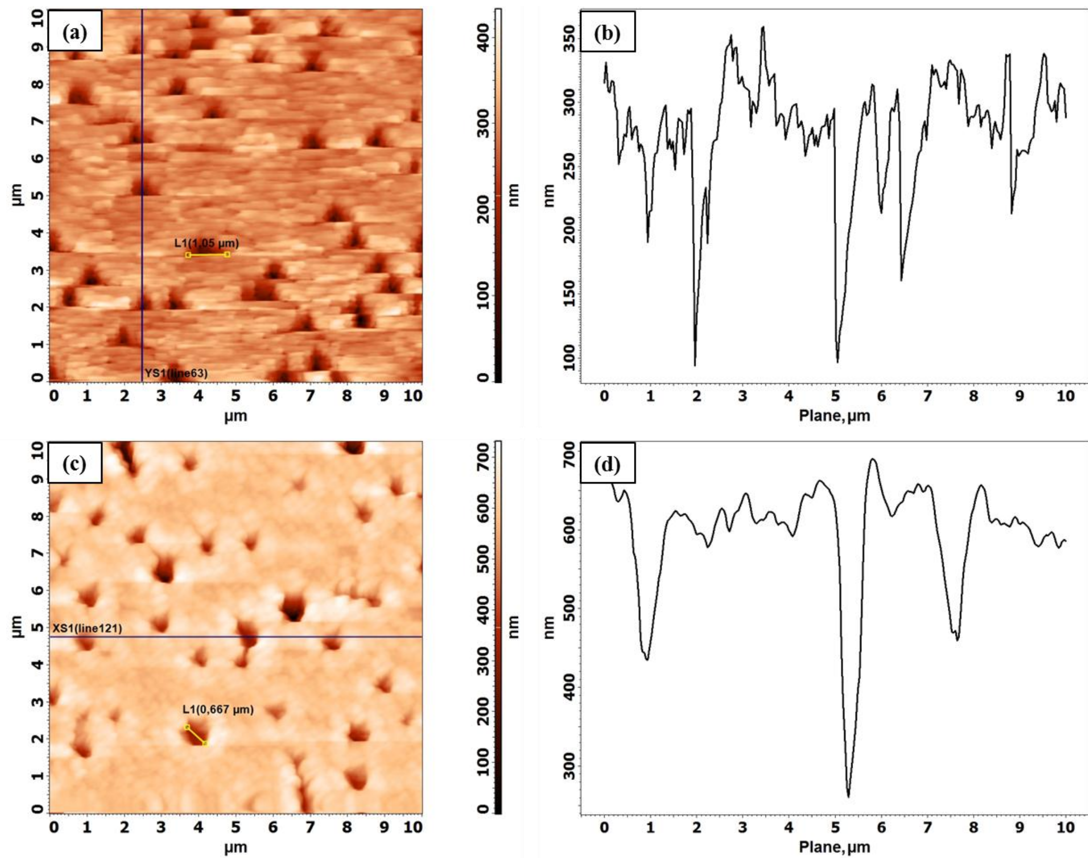

Figure 72. CT10 AFM 2D topographical images of (a) and (b) length analysis and cross-section line analysis of pits after CT10-E1 etch; (c) and (d) length analysis and cross-section line analysis of pits after CT10-N2 etch.

AFM 10µmx10µm topography images, pit width and cross section line analysis on these images for CT26 are demonstrated in Figure 73. In this figure it can be seen that E1 etched CT26 has some well-defined "triangular" etch pits on the surface (Figure 73.a). Average size of these pits was about 0.9 µm and average depth was about 130 nm. Figure 73.c shows the N2 etch pits formed on CT26. These etch pits had about 0.7 µm average size and about 330 nm average depth (Figure 73.d). From Figure 73.a and Figure 73.c, EPD values were counted as ~$3x10^7cm^{-2}$ for CT26-E1 and ~$4x10^7cm^{-2}$ for CT26-N2.

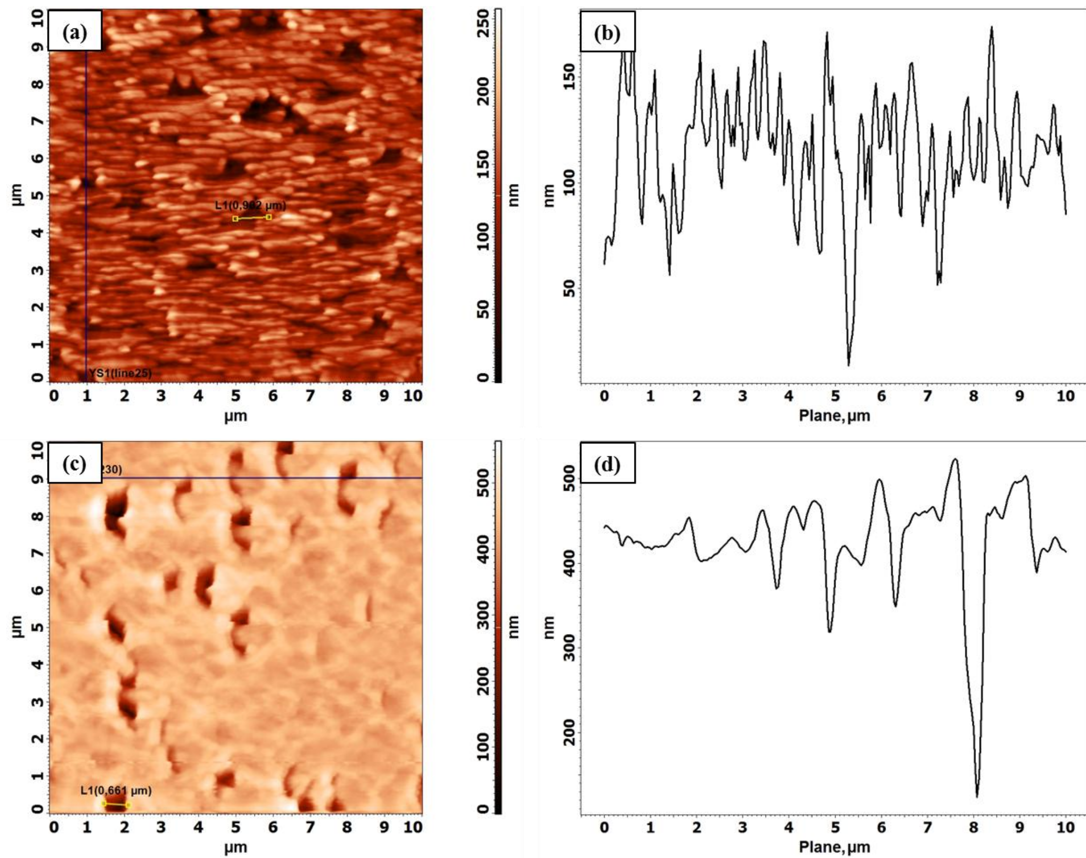

Figure 73. CT26 AFM 2D topographical images of (a) and (b) length analysis and cross-section line analysis of pits after CT26-E1 etch; (c) and (d) length analysis and cross-section line analysis of pits after CT26-N2 etch.

As mentioned before, the Everson and the Nakagawa etch solutions are the most commonly used as defect decoration techniques to reveal lattice mismatch induced dislocations. However; these etchants are effective for different crystal orientations for CdTe sample. Everson etch have an impact on only (111)B and (211)B of CdTe, not A-face. In contrast with this explanation, Nakagawa etch only effect on CdTe (111)A. Therefore, we need to explain how the Nakagawa etch worked for (211)B crystal orientation when other publications presumably were not able to get it to work. As described in section 6.3.3, as-grown surface defects were actually due to improper growth conditions related. When the Nakagawa etch ($20H_2O$:$20H_2O_2$:30HF) applied on CdTe (211)B surface for about 2-3 seconds, this solution began to etch as-grown surface.

In Figure 74.a, AFM topographical image of as-grown CT6 demonstrated that the surface defect density was approximately $3.6x10^7$ cm^{-2} and also average depth of surface defect was about 70 nm (Figure 74.b). After the Nakagawa etch applied about 2-

3 seconds, from Figure 74.c EPD value was counted as 2.8 x10^7 cm^{-2} and Figure 74.d average depth of etch pits was about 137 nm.

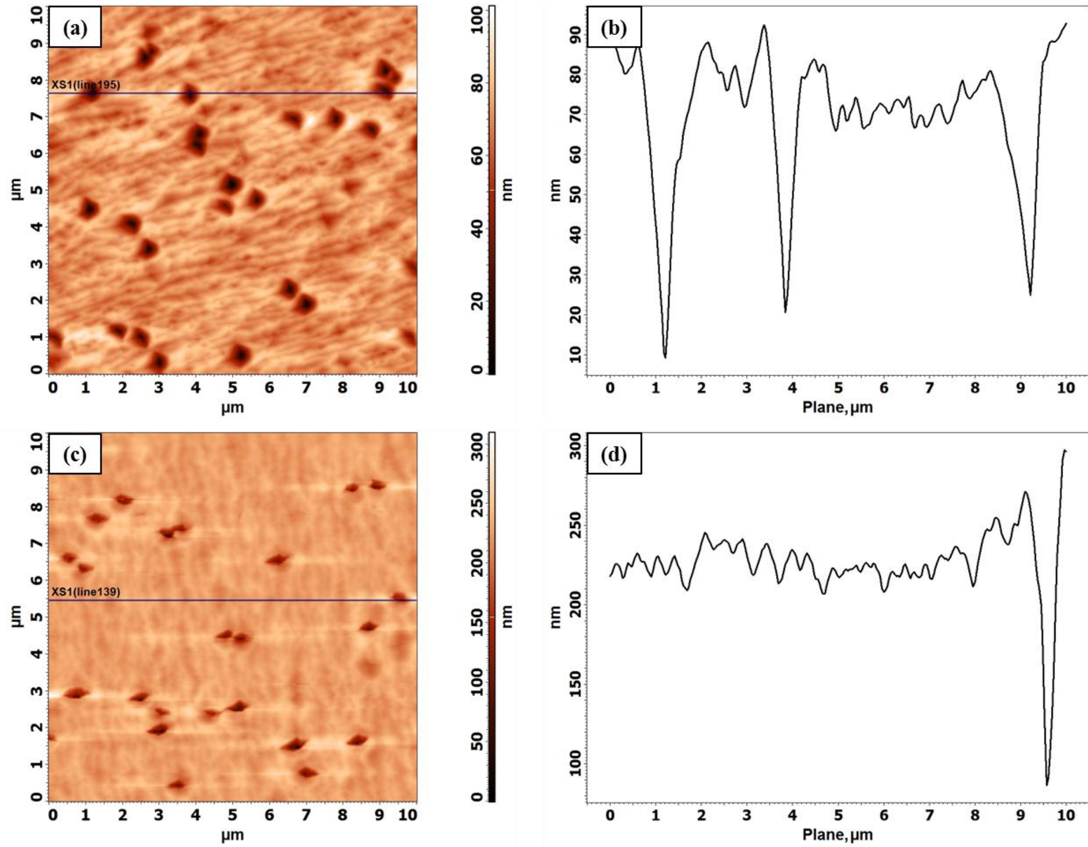

Figure 74. (a) AFM 2D topographical images and (b) cross-sectional line analysis of XS1(line 195) of as-grown CT6; (c) AFM 2D topographical image and (d) cross-sectional line analysis of XS1(line 139) after 3 seconds Nakagawa ($20H_2O$:$20H_2O_2$:30HF) etched CT6.

In Figure 75, AFM 10x10 μm^2 scanned areas of as-grown and 3 seconds Nakagawa etch pits for CT10 sample can be seen clearly. Average size of these as-grown surface defects was about 1.1 µm and average depth was about 90 nm. Figure 75.c shows the after 3 seconds Nakagawa etch pits formed on sample surface. These etch pits had about 0.6 µm average size and about 400 nm average depth. Surface defect density was calculated approximately as ~3.9x$10^7$$cm^{-2}$ and ~4x$10^7$$cm^{-2}$ for Nakagawa etched CT10 from Figure 75.a and Figure 75.c.

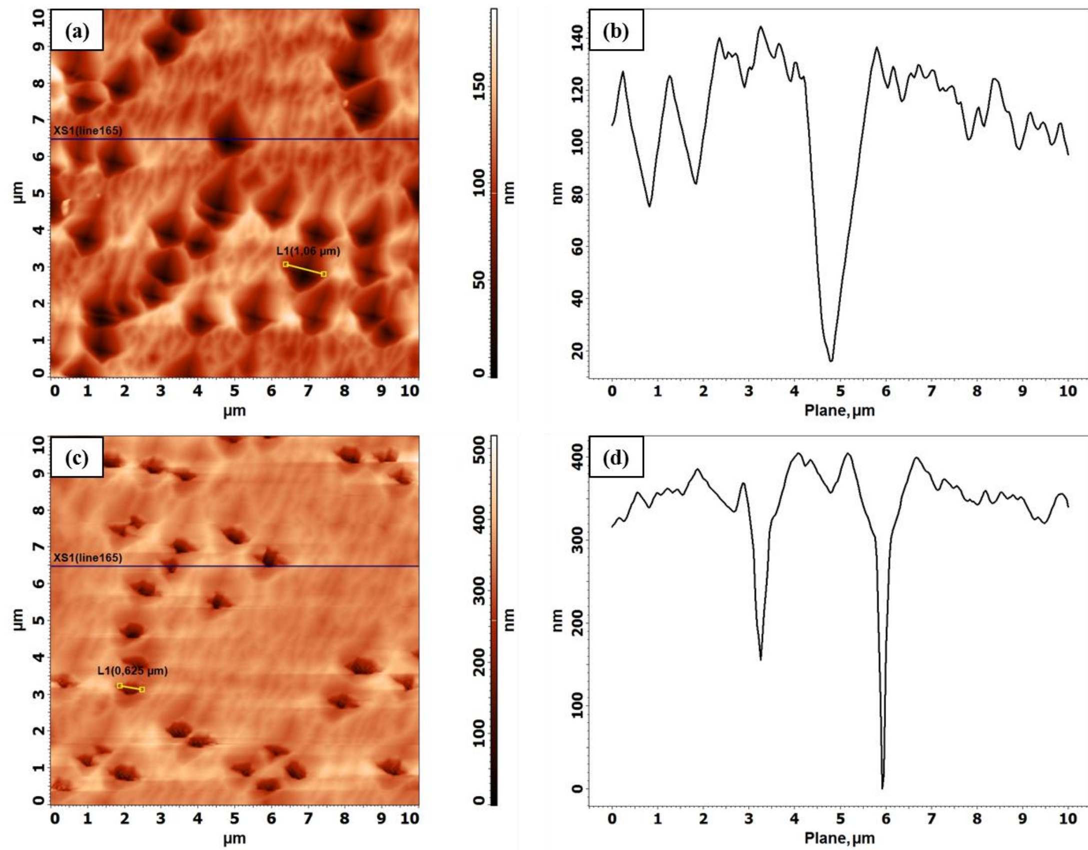

Figure 75. (a) AFM 2D topographical images and (b) cross-sectional line analysis of XS1(line 165) of as-grown CT10; (c) AFM 2D topographical image and (d) cross-sectional line analysis of XS1(line 165) after 3 seconds Nakagawa ($20H_2O$:$20H_2O_2$:30HF) etched CT10.

As shown in Figure 76.a, there are no growth-related surface defects on the as-grown CT24 buffer layer surface. When the Nakagawa etch applied on this sample surface for 2-3 seconds, no etch pits formed on surface as seen from Figure 76.c. On the other hand, when Figure 76.b and Figure 76.d were compared, it was observed that the as-grown surface structure changed due to the Nakagawa solution.

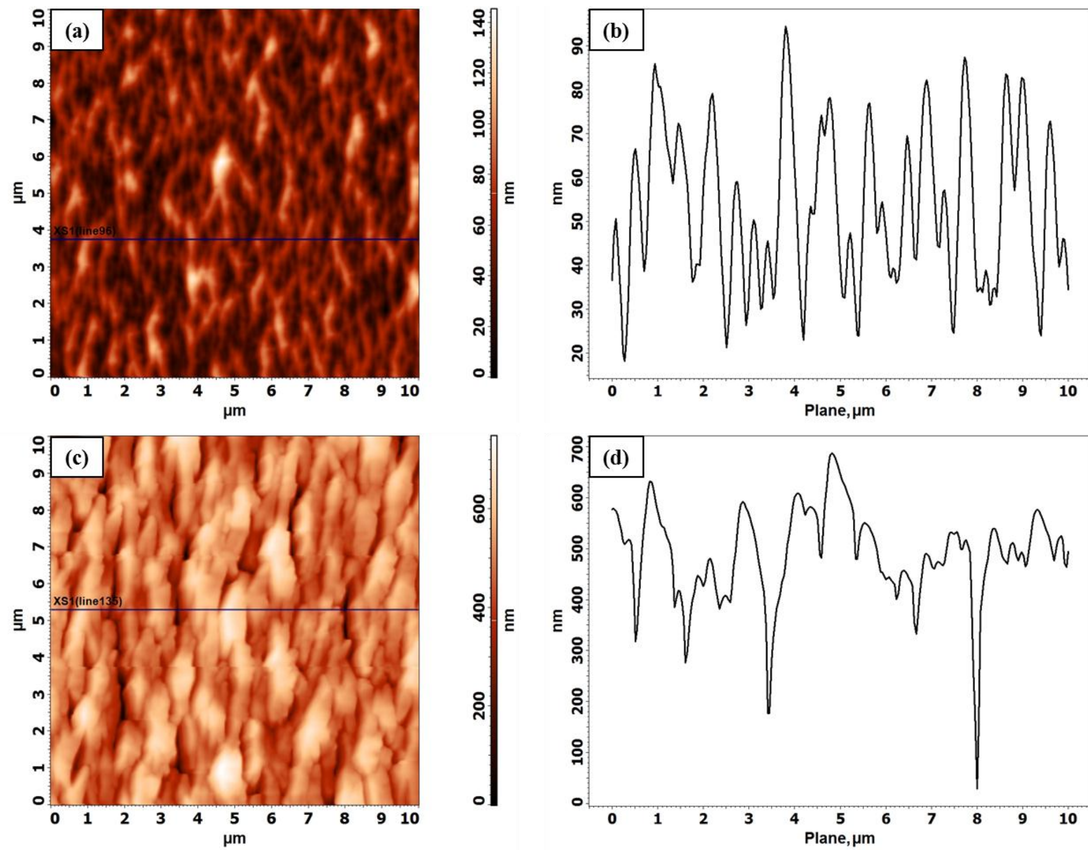

Figure 76. (a) AFM 2D topographical images and (b) cross-sectional line analysis of XS1(line 96) of as-grown CT24; (c) AFM 2D topographical image and (d) cross-sectional line analysis of XS1(line 135) after 3 seconds Nakagawa ($20H_2O:20H_2O_2:30HF$) etched CT24.

AFM 10 µm x 10 µm scanned areas of as-grown and 3 seconds Nakagawa etch pits for CT25 sample as can be observed in Figure 77. Size of these as-grown surface defects was approximately 0.8 µm and average depth was about 50 nm. After 3 seconds Nakagawa etch pits formed on sample surface as can be seen in Figure 77.c. These etch pits had about 0.6 µm average size and about 350 nm average depth. From Figure 77.a surface defect density was calculated approximately as ~$0.9x10^7cm^{-2}$ and from Figure 77.c EPD was calculated about ~$4x10^7cm^{-2}$ for Nakagawa etched CT25.

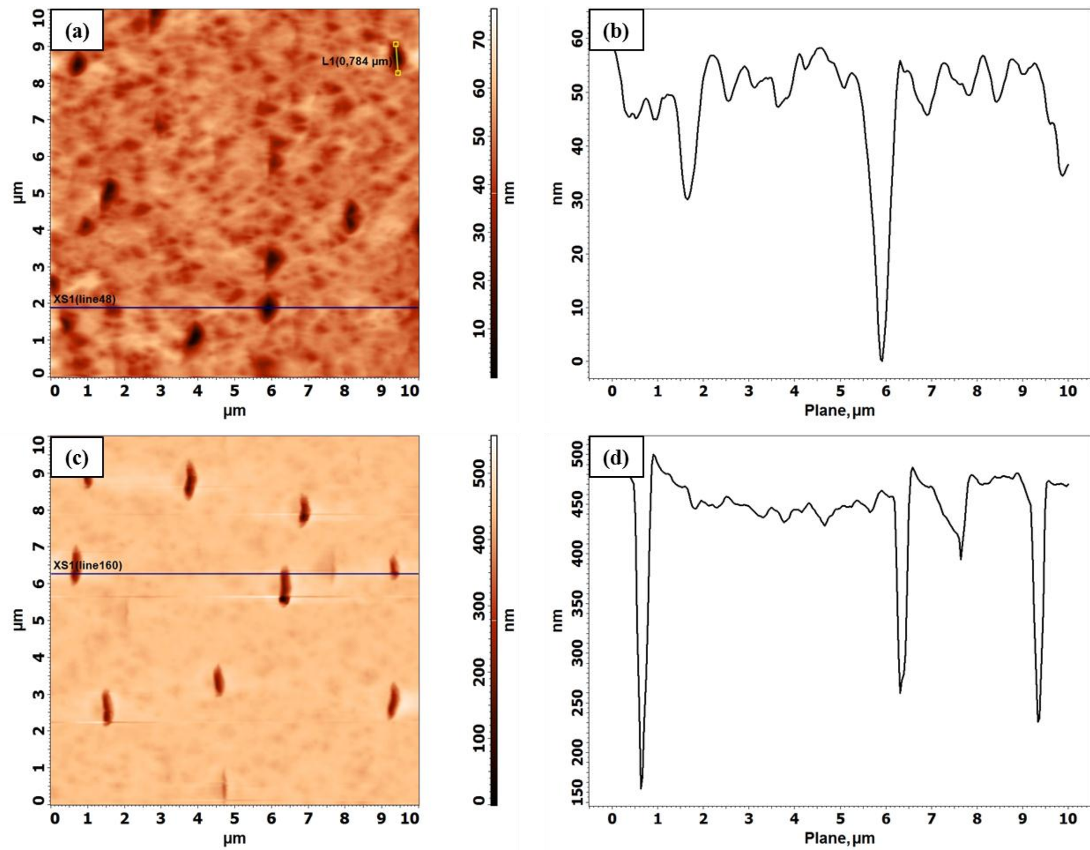

Figure 77. (a) AFM 2D topographical images and (b) cross-sectional line analysis of XS1(line 48) of as-grown CT25; (c) AFM 2D topographical image and (d) cross-sectional line analysis of XS1(line 160) after 3 seconds Nakagawa ($20H_2O$:$20H_2O_2$:30HF) etched CT25.

Origin software program was used to obtain and understand the relation between 3 seconds Nakagawa EPD and as-grown surface defect density.

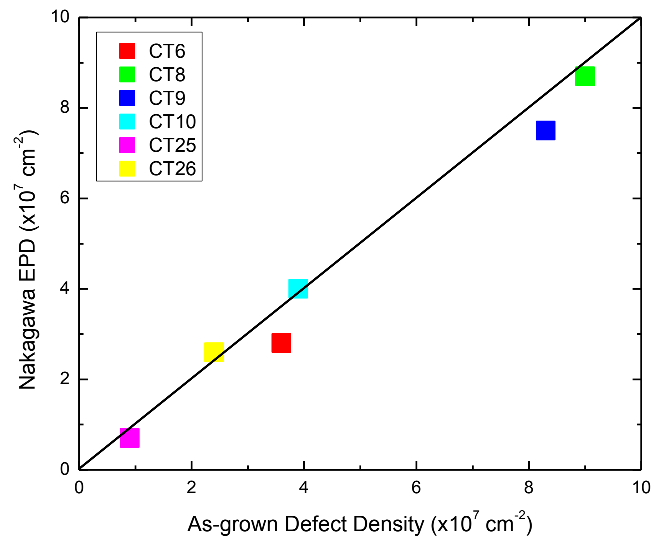

Figure 78. Comparison of 3 second Nakagawa EPD and as-grown defect density.

Everson etch yields good estimation of dislocation density. However; Nakagawa etch correlates well with as-grown improper growth condition related surface defect density as can be seen from AFM images and Figure 78.

6.5.3. SEM Characterization Results

The areal density of etch pits was obtained by both manual counting and a software program [105] from the AFM and SEM images. From AFM images, after the Nakagawa etch, etch pits on the sample surface appear to have like a sphere shaped, however, due to the high vacuum SEM images the etch pits have a smooth and specific line of shapes. These are actually “trapezoid-liked” pits which have the same orientation on the sample surfaces. The EPD values in the Table 6 and Table 7 were calculated from SEM images. Etched samples without any coating were analyzed with 20 keV energy accelerated electrons and 5 spot size. Working distance was get nearly 10 mm and images were getting ETD at 25000x magnification.

SEM images of the as-grown, Everson etched and Nakagawa etched CT6 sample surface can be seen in Figure 79. Growth-related as-grown surface defects, “triangle” and “trapezoid” shape etch pits were compared and counted easily from this

image. The only reason for giving the as-grown SEM images here was to make a better comparison between as-grown and etched surface morphologies. As-grown SEM images of the examined samples in this thesis were described in section 6.3.3. In Figure 79.b, Everson EPD value obtained by both manual and software counting which were in agreement with each other. EPD value was calculated as 8.6x10^7 cm^{-2}. “Trapezoid” shape pit density on the surface after the Nakagawa etch was obtained about 1.4x10^7 cm^{-2} from Figure 79.c.

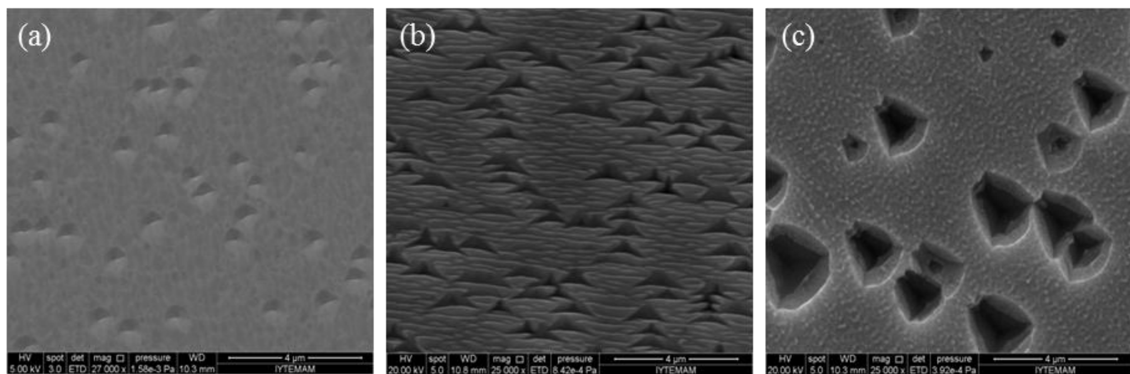

Figure 79. SEM images of (a) as-grown surface of CT6, (b) after CT6-E4 etched sample, (c) after the CT6-N2.

SEM micrograph results of as-grown surface defects which are related to growth conditions, “triangular” shape pits on the surface after the Everson etch and “trapezoid-like” pits after the Nakagawa etch can be seen in Figure 80 for CT9. Everson EPD value of the CT9-E1 etched sample was found as 1.4x10^8 cm^{-2} from Figure 80.b. After the Nakagawa etched, EPD values of CT9-N2 sample was calculated about 4.8x10^7 cm^{-2} from Figure 80.c.

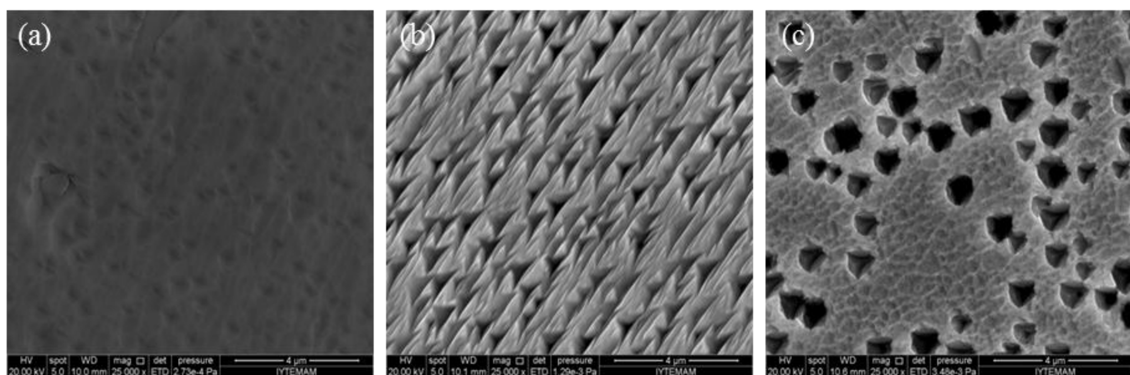

Figure 80. SEM images of (a) as-grown surface of CT9, (b) after CT9-E1 etched sample and (c) after CT9-N2.

The results for as-grown surface of CT10, CT10-E1 and CT10-N2 etched sample surfaces are given in Figure 81. From Figure 81.b "triangle" shape pit density of the CT10-E1 etched sample was found approximately $0.7x10^{8}$ cm^{-2}. After the Nakagawa etch procedure, EPD value of CT10-N2 etched sample was obtained about $0.4\ x10^{8}$ cm^{-2} (Figure 81.c).

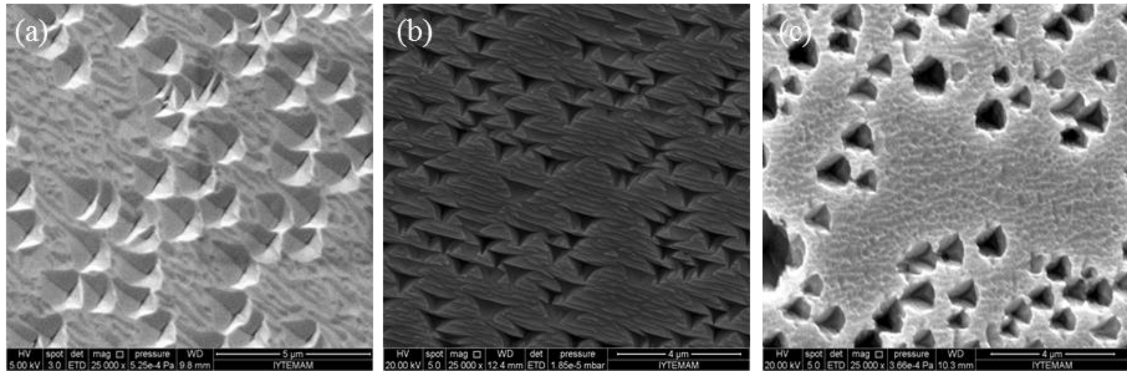

Figure 81. SEM images of (a) as-grown surface of CT10, (b) after CT10-E1 etched sample and (c) after CT10-N2.

Thus far, EPD results which were obtained from the Everson and Nakagawa were very close to each other. If it were not explained in the previous section of this chapter, it was still considered that the Nakagawa etch pits were dislocation related. However; in Figure 82, the differences between the numbers of as-grown surface defects, Everson etch pits and Nakagawa etch pits can be seen clearly for CT22. Everson EPD was calculated approximately as $\sim 1.1x10^{8}$ cm^{-2} for CT22-E1 etched sample and Nakagawa EPD was calculated about $\sim 0.03x10^{8}$ cm^{-2} for CT22-N2 etched sample from Figure 82.b and Figure 82.c, respectively. Even after the Nakagawa etch applied for 7 seconds, the numbers of as-grown surface defects (Figure 82.a) and Nakagawa etch pits (Figure 82.c) were very close to each other, because of the small number of as-grown surface defects.

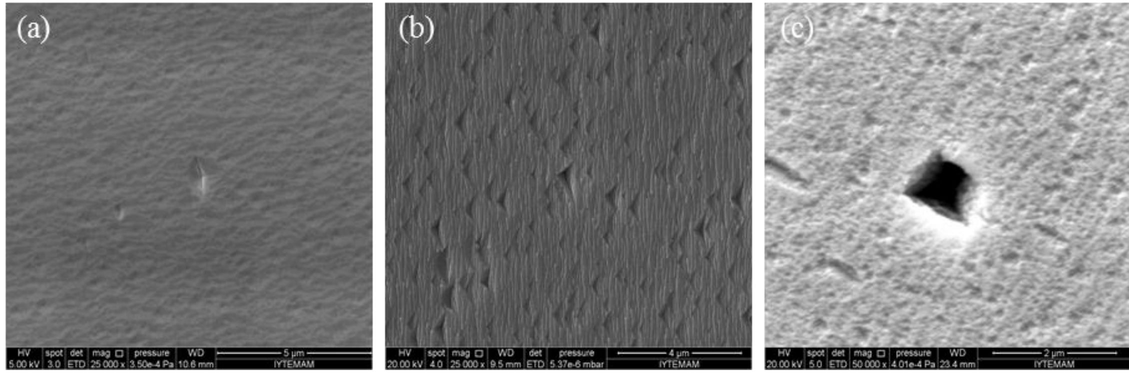

Figure 82. SEM images of (a) as-grown surface of CT22, (b) after CT22-E1 etched sample and (c) after CT22-N2.

In Figure 83.a, rough step-terrace structures which are occurred from (211) crystal orientation can be observed. Furthermore, there are no growth-related as-grown surface defects of the CT24 sample surface. After the Everson etching, it is very difficult to see and count the “triangle” shape etch pits because of rough nanoridge background structure of CT24-E1 etched sample surface (Figure 83.b). The areal density of these small etch pits was found approximately $2.3x10^8$ cm^{-2} from Figure 83.b. As shown in Figure 83.c the Nakagawa EPD value could not be calculated for CT24-N2 etched sample because there are no growth related surface defects on the as-grown sample surface.

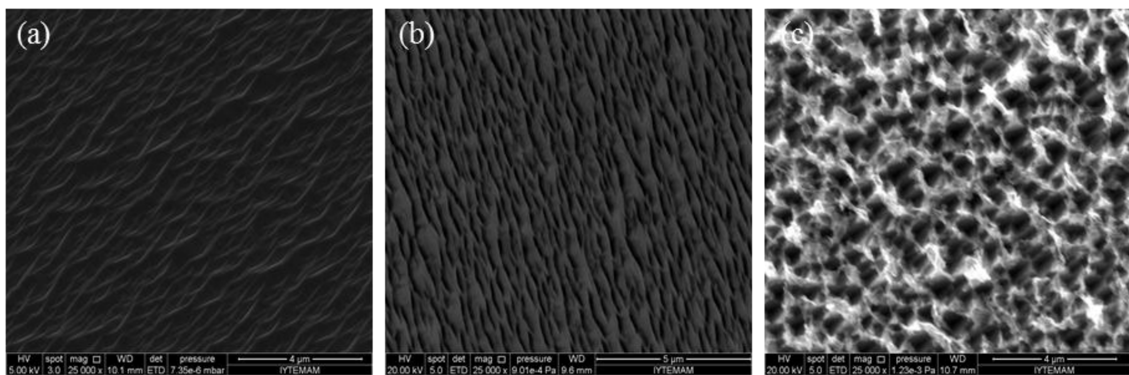

Figure 83. SEM images of (a) as-grown surface of CT24, (b) after CT24-E1 etched sample and (c) after CT24-N2.

In Figure 84, SEM micrograph surface images of CT25 sample showed that the as-grown surface defects and etch pits which are formed with “triangle” and “trapezoid” shaped due to the Everson and Nakagawa etching. Everson EPD was found approximately as $\sim 0.3x10^8$ cm^{-2} for CT25-E1 etched sample from Figure 84.b. In

addition to this, Nakagawa EPD was calculated about ~$0.04x10^8$ cm^{-2} for CT25-N2 etched sample from Figure 84.c.

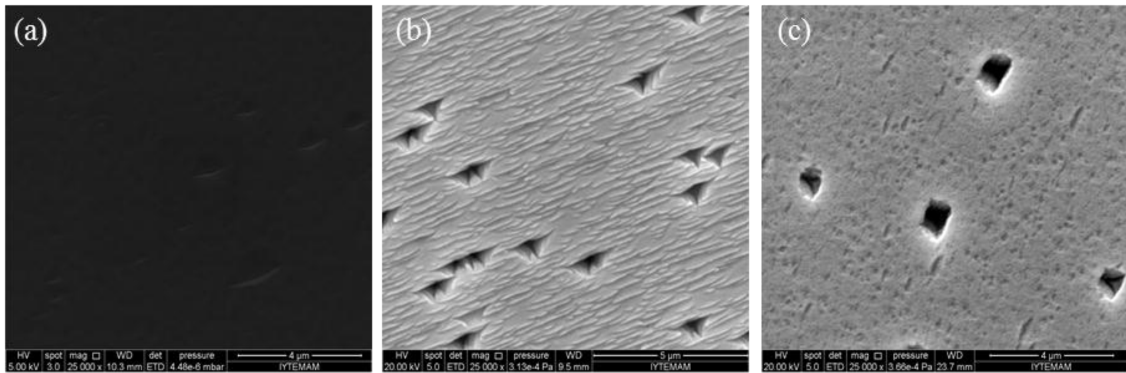

Figure 84. SEM images of (a) as-grown surface of CT25, (b) after CT25-E1 etched sample and (c) after CT25-N2.

Figure 85 showed that SEM images of CT26 as-grown, the Everson and Nakagawa etched surfaces. From Figure 85.b, calculated EPD values of CT26-E1 etched sample was found as $0.4x10^8$ cm^{-2}. “trapezoid” shape etch pit density value after the Nakagawa etching was obtained as $0.6x10^8$ cm^{-2} for CT26-N2 etched sample from Figure 85.c.

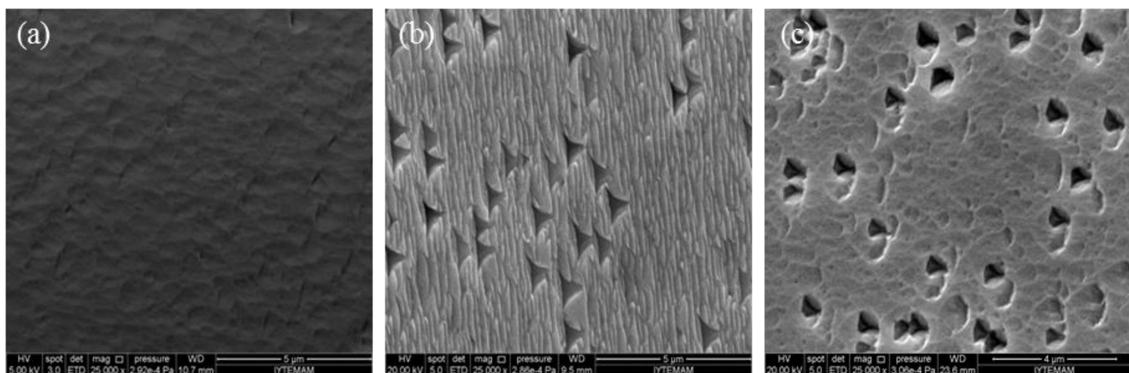

Figure 85. SEM images of (a) as-grown surface of CT26, (b) after CT26-E1 etched sample and (c) after CT26-N2.

As is similar to the CT24 sample, CT27 sample has very rough step-terrace structure and no as-grown surface defects on the as-grown surface which can see in Figure 86.a. It is very hard to see the “triangle” etch pits because these are so small and background of the CT27-E1 etched sample is very rough because of distinct nanoridge structure. Calculated EPD value of CT27-E1 etched sample was found about $3.8x10^8$ cm^{-2} from Figure 86.b. As shown in Figure 86.a, there are no growth related surface

defects on the as-grown sample surface. Therefore, Nakagawa EPD value could not be calculated for CT27-N2 etched sample (Figure 86.c)

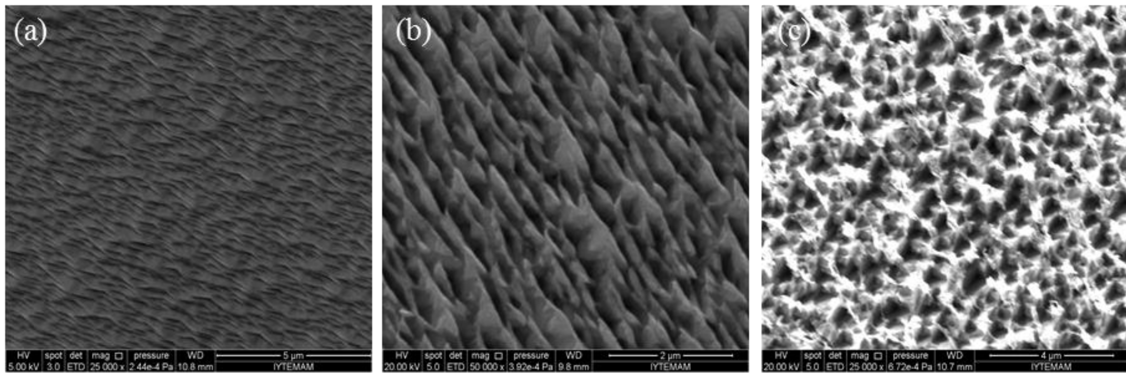

Figure 86. SEM images of (a) as-grown surface of CT27, (b) after CT27-E1 etched sample and (c) after CT27-N2.

After Everson etching, background nanoridge structure was formed all samples. This structure did not usually prevent counting etch pits except CT24 and CT27 samples. For CT24 and CT27 samples, it was very difficult to count "triangle" etch pits because of rough nanoridge structure. It can be thought that step-terrace structure of the (211) oriented sample surface have become prominent as nanoridge structure after the Everson etching. Furthermore, the Nakagawa etched samples had "trapezoid-like" pits and they were aligned in the same orientation except CT24 and CT27 samples. Additionally, EPD values obtained by AFM images are in good agreements with those obtained from SEM images. In Figure 87, it is clearly seen the distinct shapes of the etch pits and their directions are observed in both the Everson and Nakagawa etches. Etch pits should have regularly shaped and same orientation. After the Everson etch method, "triangle" shaped etch pits were converged to a single point. However; after the Nakagawa, etch pits on the surfaces had usually flat bottoms as opposed to the Everson etch pits. Briefly, Nakagawa etch pits oriented in the same direction, but had flat bottoms. Therefore, they are not also related to the crystallography.

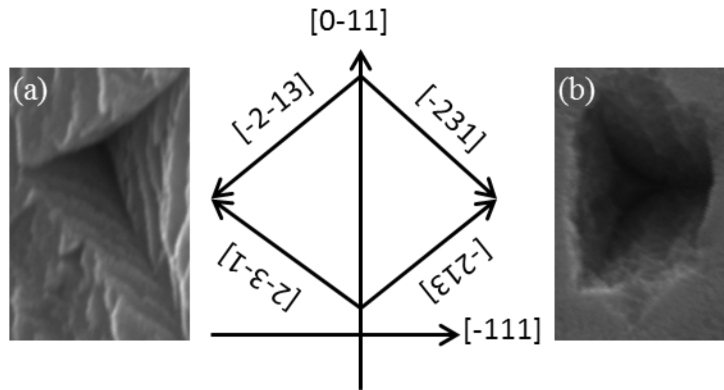

Figure 87. A comparison of (a) Everson and (b) Nakagawa etch pit shapes and their directions.

Crystal quality of the buffer layers were examined from XRD-FWHM and also Everson EPD results. The flux ratios and XRD-FWHM values of CT22, CT24, CT25, CT26 and CT27 samples were compared and plotted in Figure 88. This figure shows that CT25 was found to be higher crystal quality than other samples. Everson EPD values which were obtained from SEM images for last five samples were given in Table 7. Everson EPD versus flux ratios for CT22, CT24, CT25, CT26 and CT27 samples were compared and Figure 89 was plotted. It can be concluded that CT25 was found in better crystal quality than others.

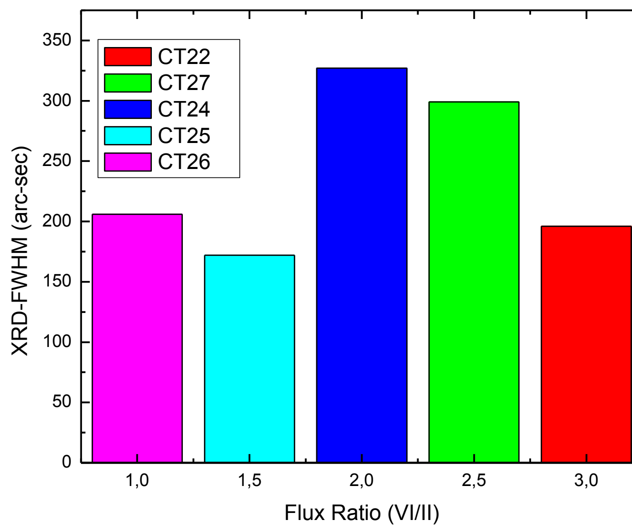

Figure 88. XRD-FWHM values versus flux ratio.

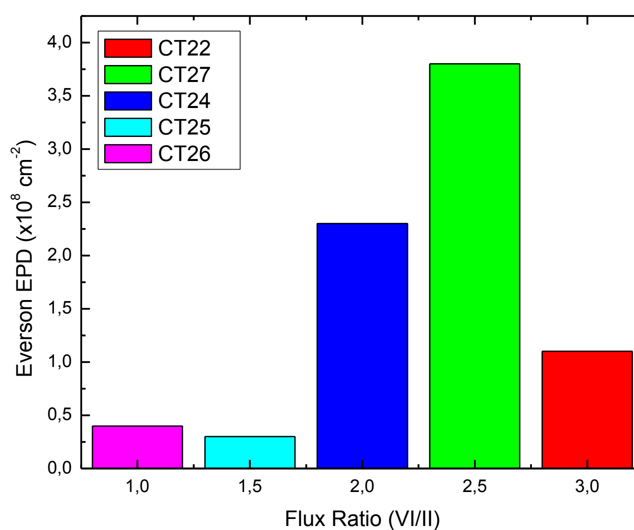

Figure 89. Everson EPD versus flux ratio.

RHEED was used as an *in-situ* characterization technique to understand the surface crystallinity during the growth. The calculated reciprocal lattice constants and the percentage error values in the Table 4 were obtained from RHEED images. Comparison between these percentage error values and Everson EPD results can be seen in Figure 90. It is understood that CT25 was better than others.

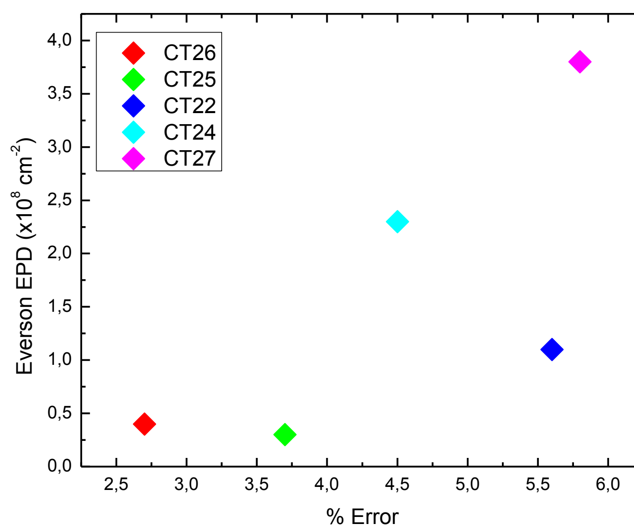

Figure 90. Everson EPD versus calculated percentage error value from RHEED.

It is known that dislocation density on the crystal quality is measured by the XRD-FWHM [107]. To find a relationship between XRD-FWHM and Everson EPD results for our buffer layers, Figure 91 was plotted. As the XRD-FWHM value is decreasing, Everson EPD value is expected to decrease. In Figure 91 this tendency can be observed even though all buffer layers were grown under different growth conditions. It is necessary to optimize the growth conditions to find an exact relationship between characterization techniques.

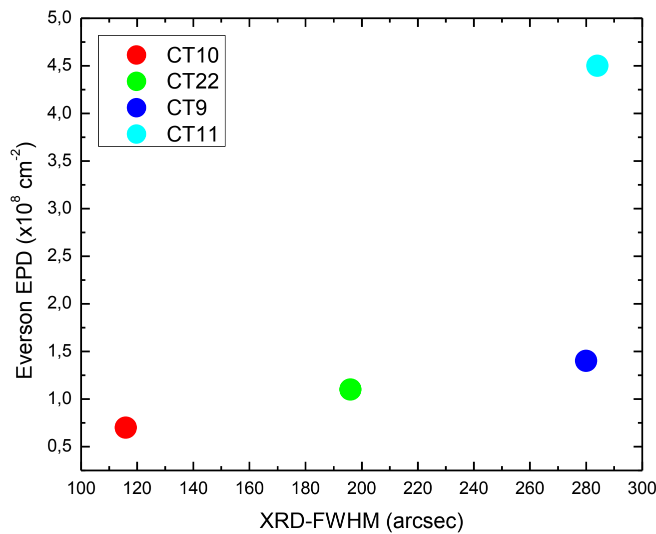

Figure 91. Everson EPD versus XRD-FWHM.

6.5.5. Raman Mapping Characterization Results

In order to investigate the effects of wet chemical etching procedures on Te, CdTe and GaAs vibrational modes, two dimensional (x, y) maps were recorded by Raman spectroscopy at room temperature. Raman measurements were performed by a confocal Raman system using Ar^+-ion 488 nm excitation laser of maximum radiation power of 120 mW with a 700 mm focal length grating spectrometer at 1800 gr/mm grating. The light was directed on sample by 100x objective and Raman scattered light was detected by InGaAs detector with a resolution of 0.3 cm^{-1}.

The two main Raman active modes in zincblende CdTe are transverse optical (TO) and longitudinal optical (LO) phonon modes at the Brillouin zone center (Γ). The

TO and LO phonon modes of CdTe occur approximately at 141 and 168 cm^{-1}, respectively [108]. Additional peaks reported at 92, 103, 120 and 147 cm^{-1} with A_1 and E symmetry modes of Te due to the presence of Te precipitates in CdTe [109]. For the samples studied here, TO, LO and 2LO phonon modes of CdTe were observed at 145.5, 169.4 and 337.8 cm^{-1} for as-grown CT6. In addition to these CdTe phonon modes, Te-specific A_1 phonon mode was acquired at126.8 cm^{-1}. For as-grown CT9, CdTe TO, LO and 2LO phonon modes were obtained at 144.4, 165.8 and 336.0 cm^{-1}. Te-specific A_1 and E phonon modes were also obtained at 104.3 and 127.5 cm^{-1}. Raman spectroscopy phonon modes for as-grown samples can be seen in Table 8. Raman intensity variation over a 20x20 μm^2 area for CT6-E4 is shown in Figure 92. Raman mapping technique was performed on an Everson etched sample (E4) with a 0.3 μm step size and 67x67 spectra were collected to form the maps. The following Raman peaks were obtained: TO and LO phonon modes of CdTe at 142.4 and 170.8 cm^{-1}, respectively. There was also 123.8 cm^{-1} peak which was indicated the presence of Te precipitates. Furthermore, a weak TO phonon mode of GaAs was observed at 275.4 cm^{-1} at some location which is the indication of deepness of the pits. As can be seen from Raman intensity maps, distribution of A_1-symmetry mode of Te and CdTe TO phonon mode resembles each other in which etched darker areas had lower intensities of A_1-symmetry mode and CdTe-like TO phonon mode. In addition, in some regions (e.g. upper and lower sides of the map area), Raman intensities of A_1-symmetry mode of Te and TO phonon mode of CdTe are higher which might be result of thickness variation due to artifact of etching process. Additionally, CdTe-like LO phonon mode intensity was lower compared to TO phonon mode intensity. Moreover, higher GaAs TO phonon mode intensities were observed at locations where weaker CdTe phonon mode intensities were observed. This was an indication that these area where the location of pits.

Table 8. A representative peak positions of phonon modes of as-grown CT6 and CT9.

As-grown sample #	Te-specific E (cm^{-1})	Te-specific A_1 (cm^{-1})	TO of CdTe (cm^{-1})	LO of CdTe (cm^{-1})	2LO of CdTe (cm^{-1})
CT6	-	126.8	145.5	169.4	337.8
CT9	104.3	127.5	144.4	169.4	338.4

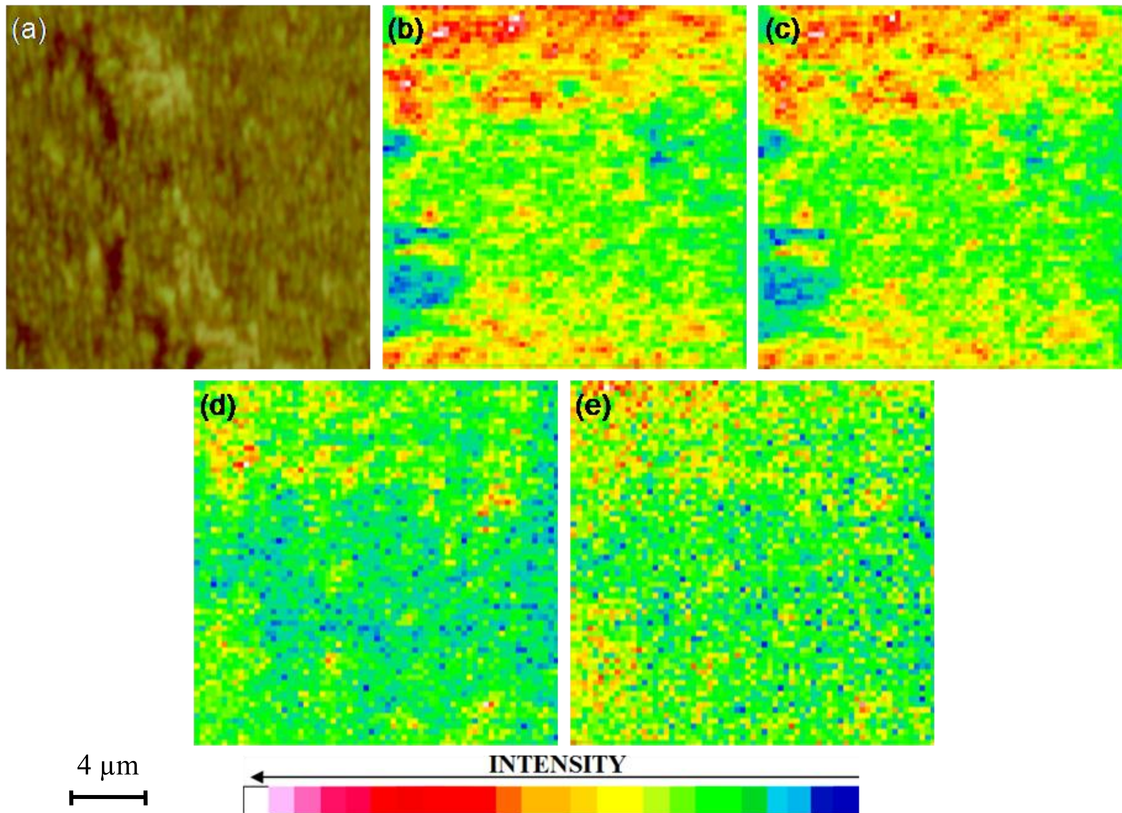

Figure 92. (a) Optical microscope image of 20x20 μm^2 scanned area on CT6-E4 etched sample, Raman intensity change of (b) A_1-symmetry mode of Te, (c) CdTe-like TO phonon mode, (d) CdTe-like LO phonon mode and (e) GaAs-like TO phonon mode.

Raman intensity distributions of CdTe-like, Te-like and GaAs-like phonon modes for CT6-N2 etched sample are shown in Figure 93. The Raman mapping was obtained from a 20x20 μm^2 area with 0.2 μm steps and Raman spectra was collected from 101x101 points. CdTe-like TO and LO phonon modes were obtained at 140.9 and 169.4 cm^{-1}. Unlike the other measurements, both Raman active TO and LO phonon mode of GaAs observed from the measurement and both were at 269.8 and 293.6 cm^{-1}, respectively. Etch pits were clearly observed in both optical image and Raman intensity variation of Te, CdTe and GaAs related phonon modes. Moreover, higher GaAs TO phonon mode intensities were observed at locations where weaker CdTe phonon mode intensities were observed. This was an indication that these area where the location of pits. The intensity of TO phonon mode of GaAs is higher for deeply etched areas (Figure 93.e). However, LO phonon mode of GaAs distributed more homogeneously which has mostly higher intensities on scanned area compared to GaAs-like TO phonon mode intensity distribution (Figure 93.f). In some point GaAs phonon mode intensities

were very high compare to the rest of the surface. These points might correspond to etch pits extending all the way to the substrate.

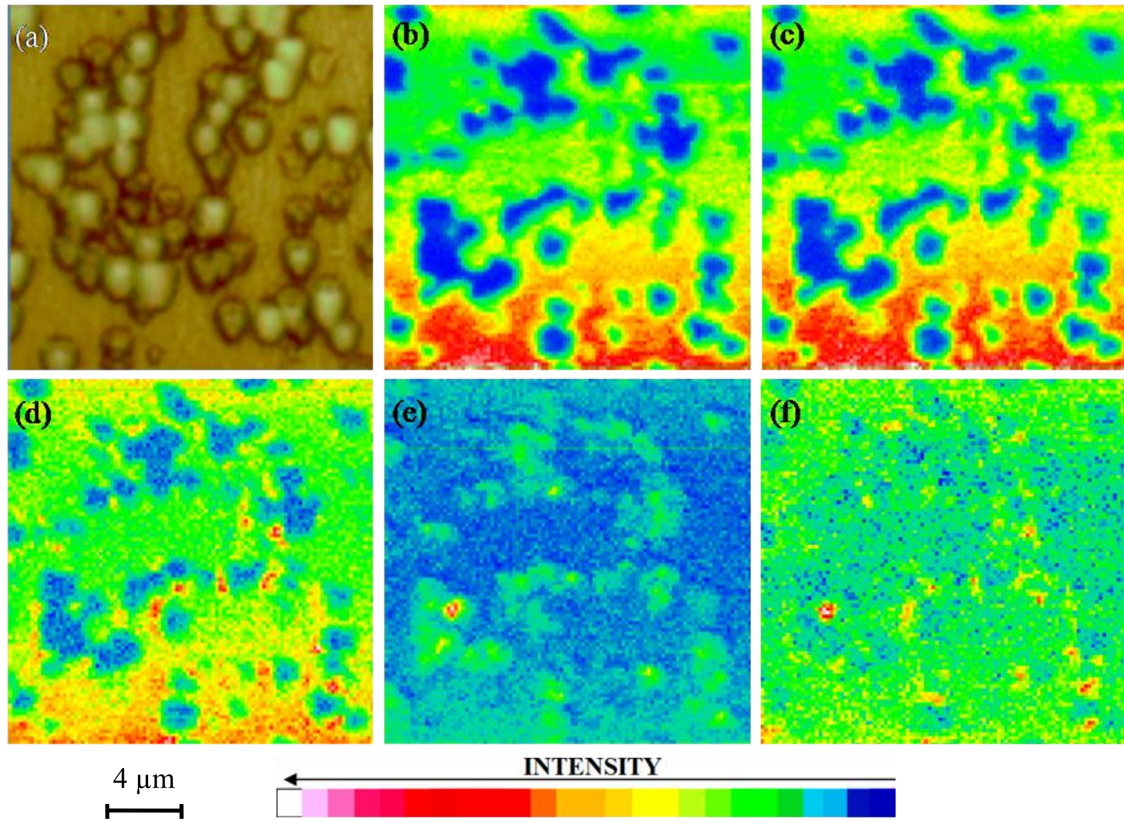

Figure 93. (a) Optical microscope image of 20x20 μm^2 scanned area on CT6-N2 etched sample, Raman intensity change of (b) A_1-symmetry mode of Te, (c) CdTe-like TO phonon mode, (d) CdTe-like LO phonon mode, (e) GaAs-like TO phonon mode and (f) GaAs-like LO phonon mode.

Te-specific A_1-symmetry mode, CdTe-like and GaAs-like phonon modes Raman intensity distributions with a step size of 0.3 μm and 135x135 scanned points in both x and y directions are shown in Figure 94 for CT9-E1 etched sample. A_1-symmetry mode of Te was observed at 125.3 cm^{-1}. TO and LO phonon mode of CdTe observed at 131.5 and 170.8 cm^{-1}, respectively. In addition, TO phonon mode of GaAs gave rise at 268.4 cm^{-1} in Raman spectrum. However, LO phonon mode of GaAs could not be observed. Unlikely to other CdTe samples, the intensities of Te-specific and CdTe-like TO phonon modes shows differences that Raman intensity of Te-specific phonon mode is lower than Raman intensity of CdTe-like TO phonon mode. Low intensity A_1-symmetry mode shows that the densities of Te-precipitates are lower. In addition, as can be seen in optical image of sample (Figure 94.a), three triangular shapes are clearly observable due to their wide etched areas which gives accurate Raman intensity distribution for all

obtained phonon modes in Raman spectra. Three triangular shapes give consistent results for all Raman maps; light blue area in Figure 94.b shows that the Raman intensity of A_1-symmetry mode of Te is higher and gives similar results for CdTe-like and GaAs-like phonon modes in which these obtained phonon modes have higher intensities. Lower intensity A_1-symmetry mode of Te (dark blue in Figure 94.b) gives also lower intensity CdTe-like TO phonon mode (green in Figure 94.c).

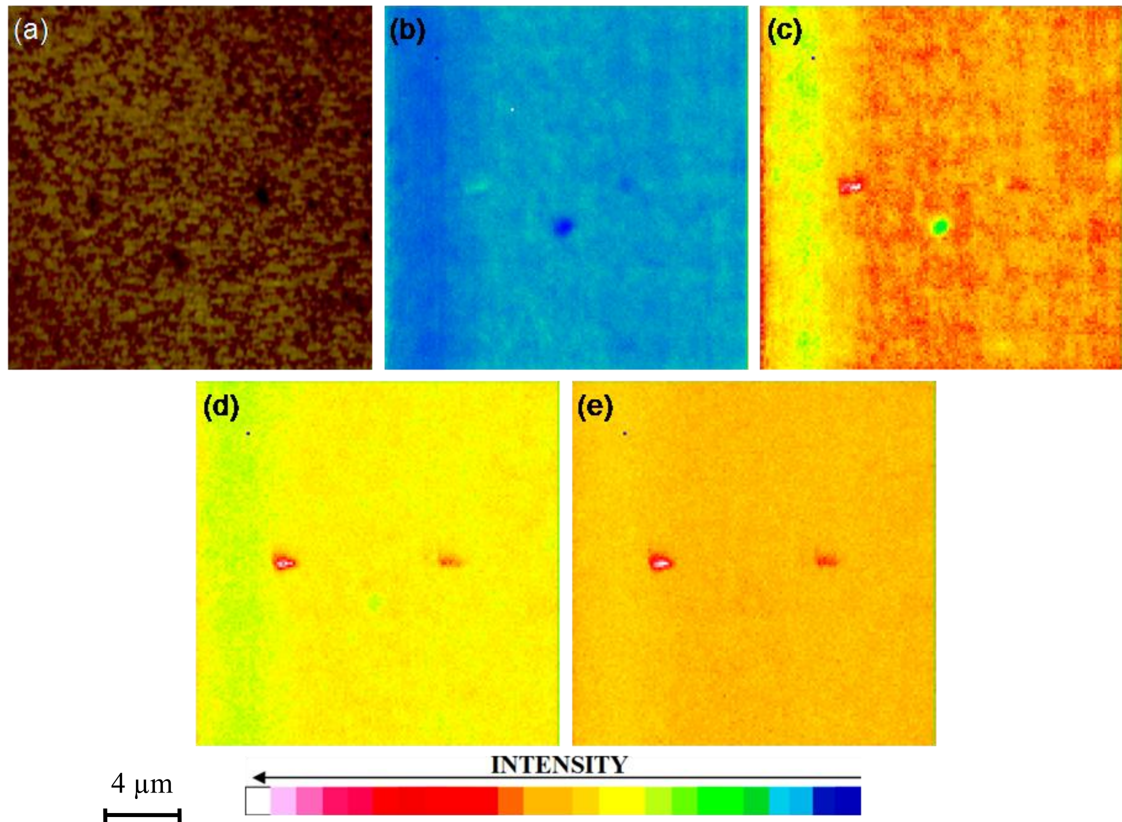

Figure 94. (a) Optical microscope image of 40x40 μm^2 scanned area on CT9-E1 etching performed sample, Raman intensity change of (b) A_1-symmetry mode of Te, (c) CdTe-like TO phonon mode, (d) CdTe-like LO phonon mode and (e) GaAs-like phonon mode.

Raman intensity distributions and optical image of 20x20 μm^2 scanned area for CT9-N2 etched sample are given in Figure 95. Raman mapping performed with 0.3 µm stepsize and 68x68 points totally scanned in both x and y directions. A_1-symmetry mode of Te gave rise a peak at 122.4 cm^{-1}, TO and LO phonon mode of CdTe observed at 142.4 and 170.9 cm^{-1}, respectively. Only TO phonon mode of GaAs obtained at 265.5 cm^{-1}, GaAs-like LO phonon mode could not be observed in Raman spectra. As seen in Raman intensity distributions in Figure 95.b and c. Raman intensities of Te-specific A_1-

symmetry mode and CdTe-like TO phonon mode gives similar results in which the Raman intensities are lower for some deeply etched areas. However, in a large area of images these modes give higher intensities (colored as yellow) which can be a result of thickness change on scanned area or higher Te-precipitates. Besides, CdTe-like LO phonon mode and GaAs-like TO phonon mode intensities are lower compared to A_1-symmetry and CdTe-like TO phonon mode Raman intensities. As seen in Figure 95.d and e, areas with higher intensities (yellow) have lower intensities of A_1-symmetry and CdTe-lie TO phonon mode which shows not deeply etched areas on the sample surface.

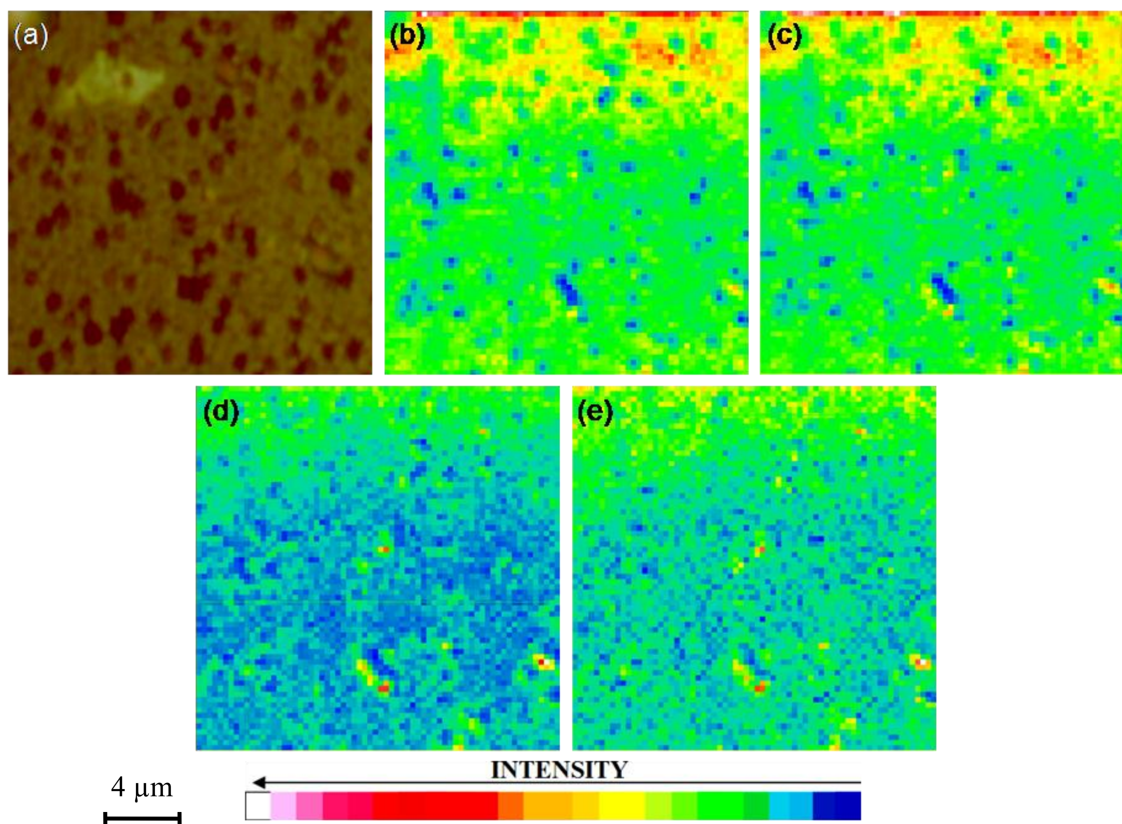

Figure 95. (a) Optical microscope image of 20x20μm^2 scanned area on CT9-N2 EPD etching performed sample, Raman intensity change of (b) A_1-symmetry mode of Te, (c) CdTe-like TO phonon mode, (d) CdTe-like LO phonon mode and (e) GaAs-like phonon mode.

Raman intensity distributions of CdTe-like, Te-like and GaAs-like phonon modes for etched CT6 and CT9 are summarized in Table 9.

Table 9. Raman intensity distribution of phonon modes of etched CT6 and CT9.

Etched sample #	**Te-specific A_1(cm^{-1})**	**TO of CdTe (cm^{-1})**	**LO of CdTe (cm^{-1})**	**TO of GaAs (cm^{-1})**	**LO of GaAs (cm^{-1})**
CT6-E4	123.8	142.4	170.8	275.5	-
CT6-N2	123.8	140.9	169.4	269.8	293.6
CT9-E1	125.3	131.5	170.8	268.4	-
CT9-N2	122.4	142.4	170.9	265.5	-

CHAPTER 7

CONCLUSION

The main interest of this thesis is to characterize the lattice mismatch induced dislocations on CdTe/GaAs (211)B buffer layers by using two different etch treatments. The thicknesses of the CdTe buffer layers which were grown on (211)B GaAs by MBE were obtained by ex-situ SE and FTIR measurements. FTIR transmittance measurements are comparable with SE measurements. The surface morphologies of the CdTe layers were analyzed by AFM, SEM and Nomarski microscopy before and after chemical etching.

To estimate the average surface roughnesses of the as-grown buffer layers, Nomarski microscopy was used. Topographic AFM images of as-grown CdTe buffer layers were used to obtain the average RMS roughness values of five different scanned regions. The width and depth values of substrate and/or growth-related surface defects were also investigated by using AFM length and cross-section analyze tools. CT10 sample was polished to investigate the source of as-grown surface defects; whether they were substrate or growth related. After the applied polishing steps, the number of as-grown surface defects was almost constant and depth of these defects decreased to approximately 88nm. This means the as-grown surface defects were not due to substrate related, but growth condition related. Growth condition related as-grown surface defect density values obtained by AFM images are in good agreements with those obtained from SEM images. Improper growth condition related surface defects were not observed for CT24 and CT27 samples.

Etch pits cannot be distinguished as one pit to calculate the areal density values by using Nomarski microscopy, but it is very easy to distinguish etch pits when using SEM. Optimized growth conditions were applied for CT22, CT24, CT25, CT26 and CT27 samples. Only flux ratios were changed. Calculated Everson EPD values for these buffer layers were compared with flux ratios and also percentage error values which were calculated from RHEED images. Furthermore, the flux ratios and XRD-FWHM values were compared. After all these comparisons, CT25 sample which were grown under 1.5 flux ratio was found in better quality than others.

It was indicated that the etch pit size depended on the etching implementation time and solution volume ratios. Decreasing the etching implementation time in both E1 and N2 etching techniques led to a slight increase in EPD values. This might be due to overlapping of enlarged etch pits with increasing etching time to a larger pit, hence, leading to undercount.

Everson etch produced “triangular” and the Nakagawa etch produced “trapezoid” shaped pits on the CdTe (211)B surfaces and pits were all aligned in the same direction. Everson etch gives good estimation of dislocation density and changing volume ratios did not affect EPD values. Comparing as grown and after-etch defect densities, it was inferred that Nakagawa etch enlarged and etched as-grown surface defects in certain crystal orientations. Therefore, Nakagawa etch can be used to relieve some specific growth related defects.

The Raman intensity distributions show that after decoration methods were performed, intensities of A_1 symmetry mode of Te, CdTe-like TO and LO phonon modes were decreased, however; GaAs-like TO phonon mode intensities were increased on triangular and trapezoid shapes. Moreover, CdTe-like LO phonon mode and GaAs-like TO phonon mode intensities were lower compared to A_1-symmetry and CdTe-like TO phonon mode Raman intensities. Te specific E_1 symmetry mode was clearly observable before both etching methods, but it was not observed after the etching.

REFERENCES

1. He, L., et al., *MBE HgCdTe on alternative substrates for FPA applications.* Journal of Electronic Materials, 2008. 37(9): p. 1189-1199.

2. Benson, J., et al., *Growth and Analysis of HgCdTe on Alternate Substrates.* Journal of electronic materials, 2012. 41(10): p. 2971-2974.

3. He, L., et al., *MBE HgCdTe on Si and GaAs substrates.* Journal of Crystal Growth, 2007. 301: p. 268-272.

4. Jacobs, R., et al., *Development of MBE II–VI Epilayers on GaAs (211) B.* Journal of Electronic Materials, 2012. 41(10): p. 2707-2713.

5. Jacobs, R., et al., *Relevance of thermal mismatch in large-area composite substrates for HgCdTe heteroepitaxy.* Journal of Electronic Materials, 2008. 37(9): p. 1480-1487.

6. Johnson, S., et al., *MOCVD grown CdZn Te/GaAs/Si substrates for large-area HgCdTe IRFPAs.* Journal of electronic materials, 1993. 22(8): p. 835-842.

7. Johnson, S., et al., *Direct growth of CdZnTe/Si substrates for large-area HgCdTe infrared focal plane arrays.* Journal of electronic materials, 1995. 24(5): p. 467-473.

8. Johnson, S.M., et al., *Effect of dislocations on the electrical and optical properties of long-wavelength infrared HgCdTe photovoltaic detectors.* Journal of Vacuum Science and Technology B, 1992. 10(4): p. 1499-1506.

9. Farrell, S., et al., *Effect of Cycle Annealing Parameters on Dislocation Density Reduction for HgCdTe on Si.* Journal of electronic materials, 2011. 40(8): p. 1727-1732.

10. Beamer, W.H. and C.R. Maxwell, *Physical Properties of Polonium. II. X-Ray Studies and Crystal Structure.* The Journal of Chemical Physics, 1949. 17(12): p. 1293-1298.

11. Mao, H.K., W.A. Bassett, and T. Takahashi, *Effect of pressure on crystal structure and lattice parameters of iron up to 300 kbar.* Journal of Applied Physics, 1967. 38(1): p. 272-276.

12. Brillouin, L., *Wave propagation in periodic structures: electric filters and crystal lattices*. 2003: Courier Corporation.

13. Rice, A., et al., *Terahertz optical rectification from< 110> zinc-blende crystals.* Applied physics letters, 1994. 64(11): p. 1324-1326.

14. Wenisch, J., et al., *MBE growth of MCT on GaAs substrates at AIM.* Journal of electronic materials, 2012. 41(10): p. 2828-2832.

15. Triboulet, R., et al., *Substrate issues for the growth of mercury cadmium telluride.* Journal of electronic materials, 1993. 22(8): p. 827-834.

16. Dhanaraj, G., et al., *Crystal Growth Techniques and Characterization: An Overview*, in *Springer Handbook of Crystal Growth*. 2010, Springer. p. 3-16.

17. Almeida, L., et al., *Growth of high quality CdTe on Si substrates by molecular beam epitaxy.* Journal of Electronic Materials, 1996. 25(8): p. 1402-1405.

18. Farrell, S.B., *Dislocation Density Reduction in Cadmium Telluride and Mercury Cadmium Telluride Grown on Silicon Using Thermal Cycle Annealing*, 2011, George Mason University.

19. Chen, Y., *Molecular Beam Epitaxial Growth of High-Quality Cadmium Telluride on Silicon.* 1995.

20. Wald, F., *Applications of CdTe. A review.* Revue de Physique Appliquée, 1977. 12(2): p. 277-290.

21. Dereniak, E.L. and G.D. Boreman, *Infrared detectors and systems*. 1996: Wiley.

22. Keyes, R.J., *Optical and infrared detectors.* Optical and Infrared Detectors, 1977. 1.

23. Rogalski, A., *Infrared detectors: an overview.* Infrared Physics & Technology, 2002. 43(3): p. 187-210.

24. Norton, P., *HgCdTe infrared detectors.* Optoelectronics review, 2002(3): p. 159-174.

25. Dhar, N.K., A.K. Sood, and R. Dat, *Advances in infrared detector array technology*. 2013: INTECH Open Access Publisher.

26. Planck, M., *On the law of distribution of energy in the normal spectrum.* Annalen der Physik, 1901. 4(553): p. 1.

27. Triboulet, R. and P. Siffert, *CdTe and Related Compounds; Physics, Defects, Hetero-and Nano-structures, Crystal Growth, Surfaces and Applications: Physics, CdTe-based Nanostructures, CdTe-based Semimagnetic Semiconductors, Defects*. 2009: Elsevier.

28. Holt, D., *Surface polarity and symmetry in semiconducting compounds.* Journal of materials science, 1988. 23(3): p. 1131-1136.

29. Selamet, Y., *Mercury cadmium telluride heterojunctions grown by MBE for infrared detection applications: An in situ doping approach.* 2004.

30. Zwanziger, D., *Fundamental modular region, Boltzmann factor and area law in lattice theory.* Nuclear Physics B, 1994. 412(3): p. 657-730.

31. Kittel, C., P. McEuen, and P. McEuen, *Introduction to solid state physics*. Vol. 8. 1976: Wiley New York.

32. Franc, J., et al., *The influence of growth conditions on the quality of CdZnTe single crystals.* Semiconductor science and technology, 2001. 16(6): p. 514.

33. Biswas, K. and M.-H. Du, *What causes high resistivity in CdTe.* New Journal of Physics, 2012. 14(6): p. 063020.

34. http://phelafel.technion.ac.il/~korens/defects.pdf, Accessed April 24, 2015.

35. Volterra, V., *Theory of functionals and of integral and integro-differential equations*. 2005: Courier Corporation.

36. Taylor, G.I., *The mechanism of plastic deformation of crystals. Part I. Theoretical.* Proceedings of the Royal Society of London. Series A, Containing Papers of a Mathematical and Physical Character, 1934: p. 362-387.

37. Orowan, E., *Mechanical strength properties and real structure of crystals.* Z. Kristallogr, 1934. 89(3/4): p. 327-343.

38. Polanyi, M. and A. Szabo, *On the mechanism of hydrolysis. The alkaline saponifications of amyl acetate.* Transactions of the Faraday Society, 1934. 30: p. 508-512.

39. http://web.mit.edu/3.091s/www/Lecture_Notes/PDF_solutions/Notes_6.pdf, Accessed April 21, 2015.

40. Frank, F., *The influence of dislocations on crystal growth.* Discuss. Faraday Soc., 1949. 5: p. 48-54.

41. http://eng.sut.ac.th/metal/images/stories/pdf/05_Dislocation_theory.pdf, Accessed April 21, 2015.

42. Callister, W.D. and D.G. Rethwisch, *Materials science and engineering: an introduction*. Vol. 7. 2007: Wiley New York.

43. Read, W. and W. Shockley, *Dislocation models of crystal grain boundaries.* Physical Review, 1950. 78(3): p. 275.

44. Gao, H., et al., *Mechanism-based strain gradient plasticity—I. Theory.* Journal of the Mechanics and Physics of Solids, 1999. 47(6): p. 1239-1263.

45. Elder, K. and M. Grant, *Modeling elastic and plastic deformations in nonequilibrium processing using phase field crystals.* Physical Review E, 2004. 70(5): p. 051605.

46. Delphenich, D., *On the topological nature of Volterra's theorem.* arXiv preprint arXiv:1109.2012, 2011.

47. Hull, D. and D.J. Bacon, *Introduction to dislocations*. Vol. 257. 1984: Pergamon Press Oxford.

48. Hirth, J.P. and J. Lothe, *Theory of dislocations.* 1982.

49. Weertman, J. and J.R. Weertman, *Elementary dislocation theory.* 1966.

50. Kittel, C. and P. McEuen, *Introduction to solid state physics*. Vol. 7. 1996: Wiley New York.

51. http://www.crystran.co.uk/userfiles/files/cadmium-telluride-cdte-data-sheet.pdf, Accessed April 21, 2015.

52. http://academic.uprm.edu/pcaceres/Courses/MechMet/MET-3A.pdf, Accessed April 21, 2015.

53. Roehl, J. and S. Khare, *Diffusion of Cd vacancy and interstitials of Cd, Cu, Ag, Au and Mo in CdTe: A first principles investigation.* Solar Energy, 2014. 101: p. 245-253.

54. Rai, R., et al., *Deformation behavior of CdTe and (Cd, Zn) Te single crystals between 200 and 600° C.* Materials Science and Engineering: B, 1991. 10(3): p. 219-225.

55. http://www.mse.berkeley.edu/groups/morris/MSE205/Extras/defects.pdf, Accessed April 24, 2015.

56. Capper, P., *Properties of narrow gap cadmium-based compounds*. 1994: Iet.

57. Yadava, R., R. Bagai, and W. Borle, *Theory of Te precipitation and related effects in CdTe crystals.* Journal of electronic materials, 1992. 21(10): p. 1001-1016.

58. Sidorov, Y.G., M. Yakushev, and A. Kolesnikov, *Dislocations in CdTe heteroepitaxial structures on GaAs (301) and Si (301) substrates.* Optoelectronics, Instrumentation and Data Processing, 2014. 50(3): p. 234-240.

59. Chou, H., et al., *Approach toward high efficiency CdTe/CdS heterojunction solar cells.* Materials chemistry and physics, 1996. 43(2): p. 178-182.

60. Ohno, H., et al., *(Ga, Mn) As: a new diluted magnetic semiconductor based on GaAs.* Applied Physics Letters, 1996. 69(3): p. 363-365.

61. Carmody, M., et al., *Threading and misfit-dislocation motion in molecular-beam epitaxy-grown HgCdTe epilayers.* Journal of electronic materials, 2003. 32(7): p. 710-716.

62. Chang, M., *Threading dislocation density reduction in heteroepitaxial layers*, 1998, University of California, Santa Barbara.

63. http://ocw.mit.edu/courses/materials-science-and-engineering/3-40j-physical-metallurgy-fall-2009/lecture-notes/MIT3_40JF09_lec05.pdf, Accessed April 21, 2015.

64. Burton, W., N. Cabrera, and F. Frank, *Role of dislocations in crystal growth.* Nature, 1949. 163(4141): p. 398-399.

65. de la Fuente, O.R., et al., *Dislocation emission around nanoindentations on a (001) fcc metal surface studied by scanning tunneling microscopy and atomistic simulations.* Physical review letters, 2002. 88(3): p. 036101.

66. Frühauf, J., *Shape and functional elements of the bulk silicon microtechnique*. 2005: Springer.

67. http://www.organic-chemistry.org/chemicals/oxidations/, Accessed April 28, 2015.

68. Myers, T., et al., *Growth of low dislocation density CdTe films on hydroplaned CdTe substrates by molecular beam epitaxy.* Journal of Vacuum Science & Technology A, 1983. 1(3): p. 1598-1603.

69. Everson, W., et al., *Etch pit characterization of CdTe and CdZnTe substrates for use in mercury cadmium telluride epitaxy.* Journal of electronic materials, 1995. 24(5): p. 505-510.

70. Benson, J., et al., *Structural analysis of cdte hetero-epitaxy on (211) si.* Journal of Electronic Materials, 2008. 37(9): p. 1231-1236.

71. Benson, J., et al., *Characterization of Dislocations in (112) B HgCdTe/CdTe/Si.* Journal of Electronic Materials, 2010. 39(7): p. 1080-1086.

72. Warekois, E.P., et al., *Crystallographic Polarity in the II-VI Compounds.* Journal of Applied Physics, 1962. 33(2): p. 690-696.

73. Nakagawa, K., K. Maeda, and S. Takeuchi, *Observation of dislocations in cadmium telluride by cathodoluminescence microscopy.* Applied Physics Letters, 1979. 34(9): p. 574-575.

74. Fewster, P., et al., *Crystallographic polarity and chemical etching of CdxHg1−xTe.* Journal of Applied Physics, 1981. 52(7): p. 4568-4571.

75. Fewster, P. and P. Whiffin, *Crystallographic polarity and etching of cadmium telluride.* Journal of applied physics, 1983. 54(8): p. 4668-4670.

76. Bagai, R., et al., *Preferential etchant for revealing crystallographic defects on (111) Te surface of CdTe crystals.* Journal of crystal growth, 1987. 85(3): p. 386-388.

77. Benson, J., et al., *Topography and Dislocations in (112) B HgCdTe/CdTe/Si.* Journal of electronic materials, 2009. 38(8): p. 1771-1775.

78. Schaake, H. and A. Lewis. *Defects in Semiconductors II*. in *Mater. Res. Soc. Symp. Proc.* 1983. North Holland New York.

79. Farrell, S., et al., *Comparison of the Schaake and Benson Etches to Delineate Dislocations in HgCdTe Layers.* Journal of electronic materials, 2013. 42(11): p. 3097-3102.

80. Knoll, M. and E. Ruska, *Das elektronenmikroskop.* Zeitschrift für Physik, 1932. 78(5-6): p. 318-339.

81. Martin, P.J., et al., *Bragg scattering of atoms from a standing light wave.* Physical review letters, 1988. 60(6): p. 515.

82. Paxton, A., et al., *How dislocations affect transport.* Journal of electronic materials, 1995. 24(5): p. 525-532.

83. Johnson, S.M., et al., *Effect of dislocations on the electrical and optical properties of long-wavelength infrared HgCdTe photovoltaic detectors.* Journal of Vacuum Science & Technology B, 1992. 10(4): p. 1499-1506.

84. Binnig, G., C.F. Quate, and C. Gerber, *Atomic force microscope.* Physical review letters, 1986. 56(9): p. 930.

85. Leite, F.L., et al., *Theoretical models for surface forces and adhesion and their measurement using atomic force microscopy.* International journal of molecular sciences, 2012. 13(10): p. 12773-12856.

86. Mironov, V.L., *Fundamentals of scanning probe microscopy.* Moscow: Technosfera, 2004: p. 144.

87. Ugural, A.C. and S.K. Fenster, *Advanced strength and applied elasticity*. 2003: Pearson education.

88. Batsanov, S., *Van der Waals radii of elements.* Inorganic materials, 2001. 37(9): p. 871-885.

89. Cappella, B. and G. Dietler, *Force-distance curves by atomic force microscopy.* Surface science reports, 1999. 34(1): p. 1-104.

90. Goldstein, J.I., et al., *Scanning electron microscopy and X-ray microanalysis. A text for biologists, materials scientists, and geologists*. 1981: Plenum Publishing Corporation.

91. Potts, P.J., *A handbook of silicate rock analysis*. Vol. 622. 1987: Blackie Glasgow; London.

92. http://www4.nau.edu/microanalysis/microprobe-sem/signals.html, Accessed April 24, 2015.

93. Georges, N., *Interferential polarizing device for study of phase objects*, 1960, Google Patents.

94. Murphy, D.B. and M.W. Davidson, *Differential interference contrast microscopy and modulation contrast microscopy.* Fundamentals of Light Microscopy and Electronic Imaging, Second Edition, 2001: p. 173-197.

95. Vainshtein, B.K., *Structure analysis by electron diffraction*. 2013: Elsevier.

96. De Broglie, L., *Recherches sur la théorie des quanta*, 1924, Migration-université en cours d'affectation.

97. Bragg, W.L. *The diffraction of short electromagnetic waves by a crystal*. in *Proceedings of the Cambridge Philosophical Society*. 1913.

98. Yang, D.-S., N. Gedik, and A.H. Zewail, *Ultrafast electron crystallography. 1. Nonequilibrium dynamics of nanometer-scale structures.* The Journal of Physical Chemistry C, 2007. 111(13): p. 4889-4919.

99. Mahan, J.E., et al., *A review of the geometrical fundamentals of reflection high-energy electron diffraction with application to silicon surfaces.* Journal of Vacuum Science & Technology A, 1990. 8(5): p. 3692-3700.

100. Resh, J., et al., *Multiple reflection high-energy electron diffraction beam intensity measurement system.* Review of Scientific Instruments, 1990. 61(2): p. 771-774.

101. Raman, C.V. and K.S. Krishnan, *A new type of secondary radiation.* Nature, 1928. 121(3048): p. 501-502.

102. Singh, R. and F. Riess, *Sir CV Raman and the story of the Nobel Prize.* 1995.

103. Sacks, R., et al., *Growth related interference effects in band edge thermometry of semiconductors.* Journal of Vacuum Science & Technology B, 2005. 23(3): p. 1247-1251.

104. Farrer, I., et al., *Substrate temperature measurement using a commercial band-edge detection system.* Journal of Crystal Growth, 2007. 301: p. 88-92.

105. http://imagej.nih.gov/ij/. Accessed April 13: p. 2015.

106. http://www.autodesk.com/education/free-software/autocad, Accessed May 26, 2015.

107. Carmody, M., et al., *Recent progress in MBE growth of CdTe and HgCdTe on (211) B GaAs substrates.* Journal of electronic materials, 2012. 41(10): p. 2719-2724.

108. Amirtharaj, P. and F.H. Pollak, *Raman scattering study of the properties and removal of excess Te on CdTe surfaces.* Applied Physics Letters, 1984. 45(7): p. 789-791.

109. Zitter, R., *Raman detection of tellurium layers on surfaces of CdTe.* Surface Science, 1971. 28(1): p. 335-338.